AN EXAMINATION OF THE APPLICABILITY OF HYDROTALCITE FOR REMOVING OXALATE ANIONS FROM BAYER PROCESS SOLUTIONS

James Peter Brady
BEd (Sec), BAppSc (Chem)

Supervisors: Dr Wayde N. Martens, Prof. Ray L. Frost

Submitted in partial fulfilment of the requirements for the degree of
Master of Applied Science (Research)

Discipline of Chemistry
Faculty of Science and Technology
Queensland University of Technology

February 2011

Keywords

Adsorption, Bayer liquor, Freundlich isotherm, hydrotalcite, kinetics, Langmuir isotherm, oxalate intercalated hydrotalcite, oxalate, thermally activated hydrotalcite

Abstract

Hydrotalcite and thermally activated hydrotalcites were examined for their potential as methods for the removal of oxalate anions from Bayer Process liquors.

Hydrotalcite was prepared and characterised by a number of methods, including X-ray diffraction, thermogravimetric analysis, nitrogen adsorption analysis and vibrational spectroscopy. Thermally activated hydrotalcites were prepared by a low temperature method and characterised using X-ray diffraction, nitrogen adsorption analysis and vibrational spectroscopy.

Oxalate intercalated hydrotalcite was prepared by two methods and analysed with X-ray diffraction and for the first time thermogravimetric analysis, Raman spectroscopy and infrared emission spectroscopy.

The adsorption of oxalate anions by hydrotalcite and thermally activated hydrotalcite was tested in a range of solutions using both batch and kinetic adsorption models.

Table of Contents

List of Figures

List of Tables

List of Equations

List of Abbreviations

BET: Brunauer, Emmett, Teller adsorption theory
BJH: Barret, Joyner, Halender method for calculating pore volumes
COD: Chemical Oxygen Demand
HT: Hydrotalcite
IC: Inorganic Carbon
IES: Infrared Emission Spectroscopy
IR: Infrared Spectroscopy
PZC: Point of Zero Charge
SEM: Scanning Electron Microscopy
TAHT: Thermally Activated Hydrotalcite
TC: Total Carbon
TEM: Transmission Electron Microscopy
TGA: Thermo-Gravimetric Analysis
TOC: Total Organic Carbon
XPS: X-ray Photoelectron Spectroscopy
XRD: X-ray Diffraction

Statement of Original Authorship

The work contained in this thesis has not been previously submitted to meet requirements for an award at this or any other higher education institution. To the best of my knowledge and belief, the thesis contains no material previously published or written by another person except where due reference is made.

Signature: _____

Date: _____

Acknowledgments

There are a number of people whom I would like to thank for their contribution to this thesis. Their effort has not been forgotten, nor can the importance of their contribution be underestimated. Among the first people I would like to thank are my supervisors, Prof. Ray Frost and Dr. Wayde Martens, both of whom have been continual sounding boards for ideas and sometimes abstract theories.

I must also thank all of the Technical staff at QUT who have provided assistance: Leonora, Chris, Karl, Dave, Eric, Arianna and the other "techies" of E-block, who have provided training on instruments, technical expertise and other invaluable advice on analytical techniques and trouble shooting. Your work is very definitely the backbone on which the Chemistry Department at QUT operates.

I also have to thank the wonderful people down at the Analytical Electron Microscopy Facility (AEMF) and X-ray Analysis Facility, Loc Duong, Thor Bostrom, Tony Raftery and the others, who have helped me solve problems involving X-ray and electron analysis of my samples.

It is also essential to thank the people who have provided assistance as I have tried different analytical techniques to solve various problems which cropped up and couldn't be solved using conventional analysis methodologies. In particular I would like to thank Dr. Mark Wellard for his patient explanation about using NMR to look at the structures of my samples and Dr. Bill Wood at UQ, who helped me with X-ray Photoelectron Spectroscopy.

I would also like to thank my fellow postgraduate students, as they have often provided sounding boards and a way to let off some steam. In particular, I would like to thank: Ashley Locke, Chris East, Bruno Basic and Henry Spratt. Thank—you for making the experience enjoyable.

Finally, I would like to thank my family for not only being a part of the journey, but also for acting as a captive audience and proof-readers. Mum and Dad, Matt and Tanya, Steffy, Scott and Karen, you have all been there when I have needed support. Your contribution has been immeasurable.

Chapter 1: Introduction

1.1 BACKGROUND

The Bayer Process is the most economical method of preparing alumina, which is further reduced to aluminium, from aluminium containing ores such as bauxite [1, 2]. However, there are a number of contaminants of concern found in the ores, the more serious of which include the organic fractions [1, 2] including humic and fulvic acids. Of the compounds found in the organic fraction, the oxalate anion is the contaminant which has the most significant effect on the quality and quantity of alumina refined from the Bayer Process.

Given the concern over the organic fractions, there is a need for their removal from the Bayer liquor, which will improve the quality of the spent liquor, the recyclability of the liquor and therefore improve the quality and quantity of the alumina products. For these reasons, the applicability of a number of methods for the removal of oxalate anions from Bayer liquors will be examined.

Some of the methods that will be examined include the use of ultra- and nanofiltration, ion exchange, catalytic wet air oxidation, adsorption via hydrotalcite-type materials, Fenton and Advanced Fenton-type oxidative methods. Each of these methods has advantages and disadvantages (which will be discussed in more detail later) which are going to affect the ultimate choice of method for the treatment of the organic contaminants.

1.2 SCOPE

The scope of the project is aimed at a number of areas dealing with the removal of oxalate from Bayer Process Liquors. The research into the use of hydrotalcites is detailed as these are most likely to provide direction for future work.

Hydrotalcites

The hydrotalcite research focuses on the surface chemistry of the materials prepared. There is a need to study the surface area and the adsorption/absorption properties of the materials in relation to the hydrotalcites.

Without an understanding of the surface structure of the hydrotalcite, it is likely to be difficult to accurately model the surface adsorption behaviour of the material and later modify the surface (or prepare a specialist material.) Furthermore, it is vital to understand the adsorption/absorption interactions of the hydrotalcites, including any equilibrium between oxalate and carbonate, the thermodynamics and how these anions interact at the material's surface.

1.3 OBJECTIVES

The main objective of this research project is to examine the applicability of hydrotalcite as an adsorbent to remove oxalate from Bayer Process Liquors. This is because oxalate is the most problematic of the organic contaminants found in the stream (as noted previously). Given the complexity of the problem, it is likely that a number of other aims will need to be achieved in order to successfully treat Bayer Process Liquor for oxalate anions. These aims include:

1. Developing a hydrotalcite that has been successfully intercalated with oxalate for characterisation and analysis;
2. Preparing and characterising hydrotalcite so that the adsorbent, absorbent and ion exchange properties can be examined;
3. Testing the adsorption, absorption and ion exchange properties of these materials to understand their physical behaviour; and
4. Modelling the behaviour of these materials in order to gain an understanding of the surface chemistry of these materials for potential further study into the preparation of future anion adsorbents.

Developing a hydrotalcite intercalated with oxalate for characterisation and analysis

It is important that a thorough understanding of the material properties of an oxalate-intercalated hydrotalcite is determined. This is because very few researchers have characterised oxalate intercalated hydrotalcite past the point of running X-Ray Diffractions (XRD) of the materials [3].

This leaves gaps in the understanding of the surface properties of these materials, particularly in the areas of surface morphology and how oxalate is incorporated into the materials. In order to successfully determine the applicability of hydrotalcite as a potential absorbent/adsorbent, it is important to understand the mechanisms through which oxalate is absorbed/adsorbed by the materials and how the surface morphology of these materials is affected by intercalation.

Preparing and characterising hydrotalcite so that the adsorbent, absorbent and ion exchange properties can be examined

It will also be necessary to gain a thorough understanding of hydrotalcite as a material. To ensure this, it will be necessary to understand the adsorption and absorption of oxalate (if any) onto the material and the surface properties of hydrotalcite.

Once an understanding of the surface properties of hydrotalcite is established, tests of the sorption of oxalate will be performed in order to gain an understanding of the oxalate pick-up of this material.

Testing the adsorption, absorption and ion exchange properties of these materials to understand their physical behaviour

This aim will require extensive testing of adsorption and absorption behaviour of prepared materials within oxalate solutions. Depending on the results, testing of these materials in synthetic Bayer liquors may also be conducted to determine their behaviour in more complex solutions.

Modelling the behaviour of these materials in order to gain an understanding of the surface chemistry of these materials for potential further study into the preparation of future anion adsorbents

After the experimental data is collected, development of a model for the surface chemistry of hydrotalcites will then be required. This model of hydrotalcite surface chemistry will be developed by preparing isotherms of adsorption and also be determining of thermodynamic properties of the oxalate absorption/adsorption processes.

1.4 SIGNIFICANCE

Despite studies into the removal of the organic fractions of Bayer liquors, there have been few studies that have noted anything more than moderate success. This is despite the use of a number of different techniques and materials [1, 4-12].

The use of hydrotalcite and hydrotalcite-like adsorption processes could be used as a gateway to the development of a number of new and innovative materials which can be used for the removal of organic contaminants from Bayer liquors and possibly other relevant applications (including the treatment of other contaminated solutions, including industrial wastes and ground waters.)

1.5 THESIS OUTLINE

The removal of oxalate anions from Bayer Process Liquors is an important stage in the treatment of the wastes generated in Alumina refining, which are harmful to the environment and can be toxic to plants and animals in the areas surrounding the waste deposition sites. This project looks to examine methods for the removal of the more environmentally damaging organic fractions, namely oxalate anions.

Chapter One outlines the background and context of this research, as well as outlining a number of objectives, before discussing the significance of this field of research.

Chapter Two outlines the state of the current literature into the removal of oxalate anions from Bayer Process Liquors, but first examines some of the major contaminants found in the liquors and how they affect the process. Chapter Two also sets out to establish the areas of study which have the most potential for the removal of oxalate anions from the liquor.

Chapter Three examines some of the theory when it comes to the adsorption processes involved in the study, with a particular focus on the adsorption isotherms and the information that they reveal about the processes involved. Furthermore, there is also a discussion of the kinetics and thermodynamics which are applicable to the study, as they will reveal a large amount of information about how the processes occur.

Chapter Four examines the experimental processes that were used, whilst Chapter Five examines the material properties and chapter Six discusses the experimental sorption results and attempts to develop a thorough understanding of the processes occurring during the adsorption studies.

Chapter Seven then draws conclusions from the results and discussion of the experimental work and Chapter Eight suggests recommendations for future research.

Chapter 2: Literature Review

During the literature review, an initial examination of the current literature with regards to the presence of oxalate anions in Bayer Process Liquors was conducted. An examination of the available removal techniques, both physical and chemical was also completed. Initially, the nature of the contaminants regularly found in Bayer liquors was briefly examined, followed by an examination of the available physical removal techniques and the available oxidative, or chemical, removal techniques. Finally, the most appropriate removal technique was identified for further research.

2.1 INTRODUCTION

There has been a considerable amount of literature published on the treatment of organic contaminants in Bayer Process liquors and there has been a considerable amount of research conducted into the removal of these (and other) contaminants from Bayer liquors [1, 2, 4, 7, 10, 13]. This examined some of the methods for removing these anionic contaminants, in particular focussing on the oxalate anion from spent Bayer liquors.

There are a number of removal techniques available for the treatment of Bayer liquors [1, 2, 4, 7, 10, 13], including nanofiltration, ion exchange, catalytic wet air oxidation, Fenton (and advanced Fenton-type) reactions, as well as adsorption using anion-specific adsorbent materials. Each of these methods was examined in detail before concluding which methods of oxalate removal were tested.

2.2 BAYER PROCESS

The Bayer Process is the most economic process by which Aluminium ores, such as bauxite (which is a combination of aluminium hydroxides and assorted impurities) are treated to recover/extract gibbsite ($Al(OH)_3$) for reduction to aluminium metal [1, 2]. A brief diagram showing a simplified flow of caustic through the Bayer Process is shown below.

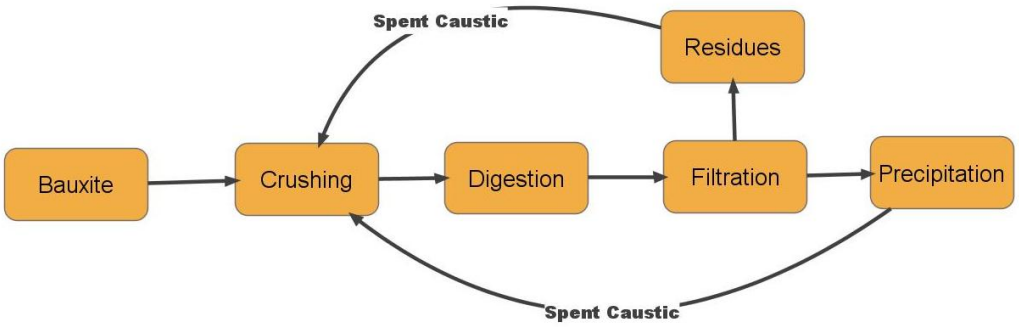

Figure 2.1: Brief outline of the flow of caustic through the Bayer process

The process itself involves the digestion of ground bauxite ore in a solution of hot sodium hydroxide with a concentration of approximately 3M [1] and a temperature somewhere between 150-250 °C under high pressures [1], although the exact conditions vary from refinery to refinery, due to different amounts of boehmite in the ores. Larger boehmite concentrations increase the digestion temperature of the ore, which in turn increases the decomposition of non-volatile organics to oxalate. After the aluminium hydroxide compounds have been dissolved into the solution, the slurry is cooled and diluted before the residues, containing mostly red mud [13], are removed from the solution. This leaves behind the aluminium hydroxide compounds (sodium aluminate [$NaAl(OH)_4$]) which are then passed to the precipitation stage [2].

The next step in the process involves the precipitation of the aluminium hydroxide compounds through the use of seeding with aluminium trihydroxide ($Al(OH)_3$) [2]. The Bayer liquor is then recycled and reused.

During the process, there is a build up of soluble organic compounds that interfere with the precipitation of the aluminium trihydroxide. The organic substance which is generally considered to be the worst contaminant of the Bayer liquor is the oxalate ion. As a result, there have been in a number of studies as to not only the effects that the presence of oxalate (and other organic acids) have on the process [1, 2, 14, 15], but also studies into methods for the removal of these compounds from the liquor. These studies have included the use of oxidiation methods [1, 4, 7, 10]; as well as some studies into the use of hydrotalcite-type compounds as other possible options for the absorption of these organic compounds from the Bayer liquor [13].

The removal of these organic contaminants from spent Bayer liquors, with a specific focus on oxalate anions is the main focus of this project.

2.2.1 NATURE OF THE BAYER LIQUOR

The nature of Bayer liquors from different refineries varies to some degree as different conditions, caused by differences in aluminium-containing ores, result in different levels of contaminants in the spent Bayer liquor [1, 2, 14-23]. All Bayer liquors contain a number of contaminants which have an effect on the efficiency of the process. Shown below is a figure showing some of the major contaminants found in the Bayer liquor and how they are later related to each other within the mixture.

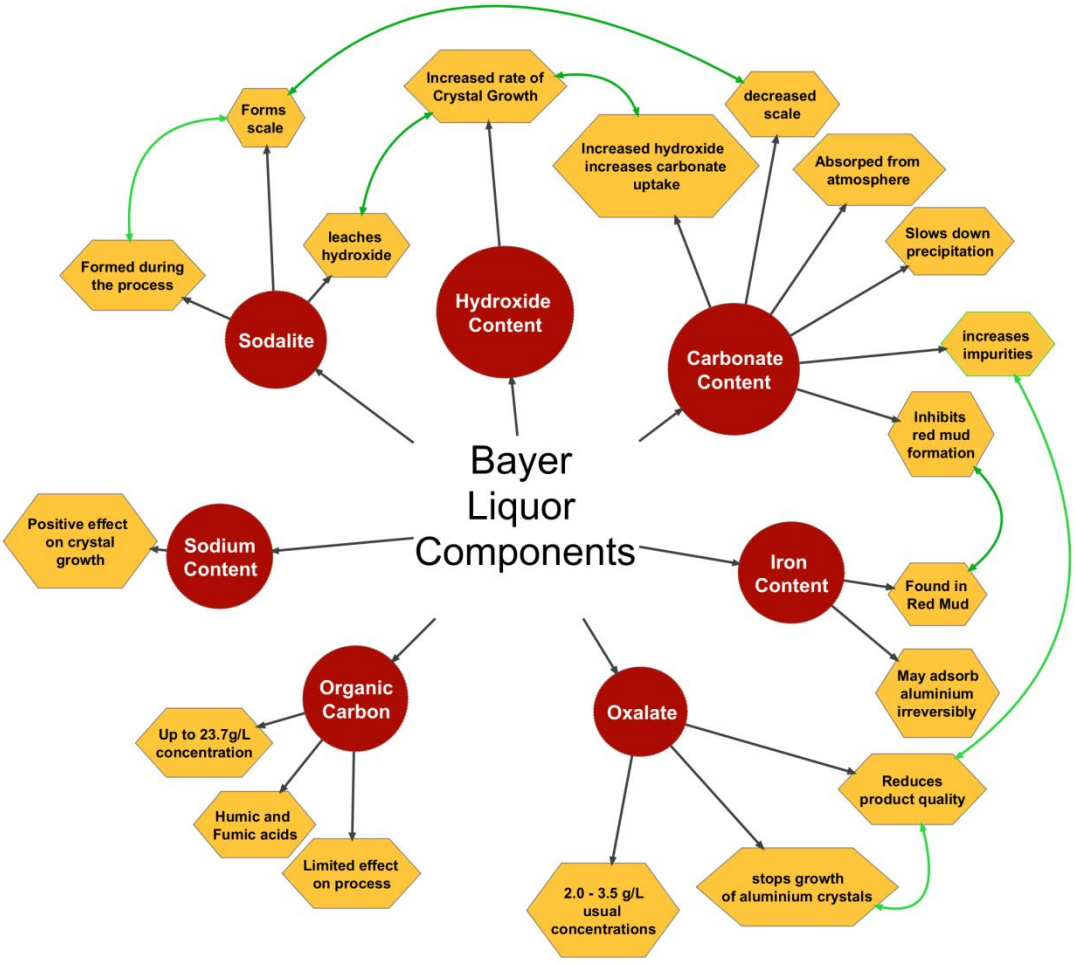

Figure 2.2: Brief outline of some Bayer liquor contaminants and their relationships to each other

2.2.2 MAJOR CONTAMINANTS AND THEIR EFFECTS ON THE PROCESS

There are several major contaminants that have an adverse effect on the efficiency of the Bayer Process. For ease of reference, only the contaminants that have more serious effects on the Bayer Process are discussed.

2.2.2.1 OXALATE ANION ($C_2O_4^{2-}$)

The oxalate ion is considered to be a major issue in the Bayer Process because it co-precipitates from solution with the aluminium trihydroxide, which results in inferior quality product [2]. The current theoretical mechanism of action suggests that the oxalate ions are poisoning the growth of aluminium trihydroxide crystals by precipitating out as aluminium oxalate complexes; as well as adsorbing to the surface of the aluminium trihydroxide crystals; which then prevents the bayerite crystals from settling to the bottom of the tank during the precipitation stage. This results in the non-precipitated crystals being recycled with the rest of the liquor with a resulting loss in efficiency of the process [2].

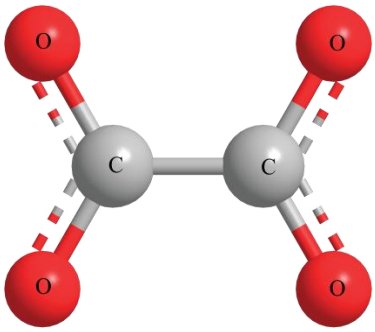

Figure 2.3: Ball and stick model of the oxalate anion

The oxalate ion is generally found in the form of sodium oxalate and can be found in concentrations that vary from 2 g/L to as high as 3.5 g/L [1, 20, 21, 23] although the concentration will vary because of the different bauxite ores used in the Bayer Process by different alumina plants [23]. Guthrie, and Improgno (as noted in Wellington & Valcin, 2007 [1]) reported that oxalate anions, along with formate, ethanoate and succinate formed up to 45% of the total organic components of spent Bayer liquors [19].

2.2.2.2 SODALITE ($NA_2O.AL_2O_3.2SIO_2.2H_2O$)

Sodalite is a compound that is formed in Bayer liquors during the Bayer process which has the effect of leeching hydroxide from the solution and making it less caustic. Furthermore, the sodalite deposits in the form of scale, which then needs to be cleaned from the digesters and heat exchangers [2].

2.2.2.3 ORGANIC CARBON

Organic Carbon compounds, in the form of carboxylic acids, fulvic acids and humic acids are also found in the spent Bayer liquor, sometimes with concentrations of up to 23.7 g/L [1]. These compounds have some effect on the precipitation of aluminium trihydroxide from the Bayer liquor. Their presence should be noted and methodologies for their removal should also be investigated with a view to improving the efficiency of the process liquor.

2.2.2.4 IRON CONTENT

Iron is found naturally in most bauxite deposits and is a major component of the "Red Mud" that is discharged as waste from the process [24, 25]. Palmer, Frost and Nguyen [24] found evidence which suggests that the presence of iron (III) complexes in the Bayer liquor may result in the adsorption of aluminium ions in a process reported to be irreversible, which has a negative effect on the quantity of alumina recovered from the ores.

2.2.2.5 SODIUM CONTENT

Sodium is naturally found in the Bayer liquor and it has been found to have a positive effect on the aggregation and growth of the gibbsite [γ-$Al(OH)_3$] crystals [26]. Furthermore, there is some evidence to suggest that the presence of the sodium ions in the solution stabilises the aluminate ions in the solution [15, 18]. There has also been some study into the use of Lithium and Potassium based caustic compounds as the basis for the Bayer liquor, but Li, Prestige and Addai-Mensah found that the presence of the sodium has greater positive effects than the presence of potassium ions [27, 28] due to sodium ions providing a more favourable crystal formation pathway than potassium ions.

It has to also be noted that the presence of sodium in the Bayer liquor has been linked to the presence of impurities of sodium in the gibbsite products [15, 18].

2.2.2.6 HYDROXIDE CONTENT

The hydroxide concentration helps to control the concentration of the oxalate ion through various processes [2]. In industrial applications of the Bayer Process, the hydroxide concentration is maintained at approximately 3 M, although this varies with the aluminium concentration of the ore. It has been reported that the correct ore to hydroxide ratio increases the growth rate of $Al(OH)_3$ crystals due to interactions between aluminium hydroxide super saturation, temperature, caustic, salt identity and concentration as well as other factors through mechanisms which are not well understood [26].

2.2.2.7 CARBONATE CONTENT

The presence of carbonate in the Bayer liquor is due to the Bayer Process being performed under a normal atmosphere under increased pressure, which results in the adsorption of carbon dioxide from the immediate environment. With an increase in pH, the presence of more hydroxide anions results in an increase of the uptake of carbonate ions into the liquor [24].

There is also evidence to suggest that the presence of carbonate ions in high concentrations in Bayer liquors may reduce the precipitation of iron in red mud [29]; which would have the effect of slowing down the process and increase impurities in the gibbsite precipitate. Zheng [30] found that high carbonate concentrations decrease the precipitation of unwanted scale throughout the machinery of the refining process. The formation of scale during the process results in a loss of hydroxide and aluminium products.

2.2.2.8 SUMMARY

The Bayer process has found widespread use in the alumina industry as the method of choice of producing alumina for further reduction to aluminium metal. However the Bayer liquor, which is a highly caustic solution, suffers from a build up of contaminants including soluble organic compounds and most notably oxalates, which reduce the efficiency and quality of the process. The matrix of contaminants in the system is quite complex and includes the presence of the mineral sodalite; along with carbonate, iron and sodium ions as well as organic acids (including oxalate) all of which have some impact on the quality and quantity of the yield through a number of complex interactions.

The use of oxalate as a marker for the contamination of the system is based on the small quantity which is required to have an adverse effect on the crystal growth of aluminium trihydroxide (as little as 3.5 g/L), which is used as a gauge for the efficiency of the process.

2.3 PHYSICAL METHODS FOR THE REMOVAL OF ORGANIC CONTAMINANTS

There are a number of physical methods that can be used for the removal of materials from solution. However, it is important to keep in mind the properties of the matrix as well as the contaminant to be removed when considering the applicability of any particular removal method. For this reason, the physical methods examined here are all methods which have been examined for the removal of contaminants from Bayer liquors in the past.

The physical methods that will be examined here include nanofiltration (the use of nanoscale membranes to filter out contaminants); ion exchange (physically exchanging contaminant ions from the solution and replacing them with other, less harmful ions) and the use of adsorption processes (where contaminants are adsorbed onto the surface of a material which is then subsequently removed from the system.)

2.3.1 NANOFILTRATION

2.3.1.1 INTRODUCTION

Nanofiltration, a technique using size and charge exclusion to remove contaminant particles at sizes between around 10-100 Angstroms (Å), has been reported since the 90s. Since then, nanofiltration has found increasing use in industry as a separation method, replacing other separation techniques such as extraction, ion exchange, evaporation and distillation for the removal of selected species [31].

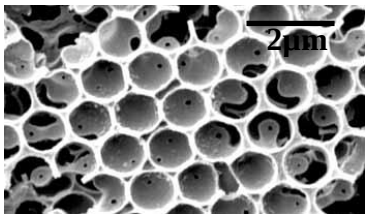

Figure 2.4: SEM image of a nanofiltration membrane[1]

Modern nanofiltration methods are based upon a polyamide-type compound where the selective layer of the filter is a three dimensional structure of polymer chains [32]. The orientation of these polymer chains determines the performance of the nanofilter, and the orientation of the polymer chains is determined by the temperature of solution [33], which is usually limited to under 60 °C. The solution is run through the filter at pressures of between 5 and 50 bar [31] for maximum separation.

The mechanism through which nanofiltration works is based upon a combination of both charge and size exclusion [34]. This makes it an ideal separation method for separating small, charged ions from a solution containing a mixture of charged and neutral solutes which cannot be easily separated by other means. Despite being a very useful technique for separation of very small particles, it still hasn't found widespread use in industrial applications due to the limited lifetime of the membranes, which is limited due to factors such as the viscosity and pH of the solution, as well as its temperature and ionic strength [34]. The other major factor contributing to the limited lifetime of the membranes is the regeneration techniques used to clean the membranes are quite capable of irreversibly damaging the membrane [34, 35].

2.3.1.2 ADVANTAGES

The major advantage of using nanofiltration as a technique for the recycling of Bayer liquor is that it will remove oxalate from the solution [36]. The use of nanofiltration is also suggested to remove most of the other contaminants in the solution as well, some of these being iron, carbonate and organic carbon compounds [1, 2, 15, 19].

1. http://www.mindfully.org/Technology/2003/Nanomaterials-Sustainability-Risk22sep03.htm Accessed 10 September 2009

2.3.1.3 DISADVANTAGES

Unfortunately, there are also a number of disadvantages to the use of nanofiltration in solutions such as Bayer liquors. The most prominent of these disadvantages is membrane fouling, which is generally considered to be irreversible [35].

Membrane fouling in Bayer liquors would most likely be caused by the presence of larger organic materials, which occur naturally in the bauxite ore [37]. There are three major mechanisms for membrane fouling reported in the literature: Pore blockage, pore restriction and cake formation [35, 37]. Van der Bruggen [35] reports that the most common methods of dealing with membrane fouling are:

- Optimise solution pretreatment;
- Chemically clean the membrane (which is usually done with solutions that are outside of the membrane's chemical resistivity); and
- Physical cleaning using methods such as sonication, scrubbing and flushing [35]

Van der Bruggen [35] also reported that the cleaning protocols utilised in the treatment of nanofiltration membranes are dependent upon the nature of the feed solution and that cleaning protocols are usually determined through the use of trial and error [35].

It was also noted that the most commonly reported problems with the nanofiltration membranes are dissolution, deformation and swelling of the membranes [35]. These issues are caused by the high pH modifying the membrane surface [32, 34] and elevated temperatures damaging the membrane [9, 34].

Another issue that needs to be seriously considered is the disposal of materials caught in the filters. The retentate left from the filtering process is going to be high in contaminants which then need to be disposed of. There are some options for the disposal of these waste products, including [35]:

- Incineration;
- Direct or indirect discharge of the contaminants into surface or groundwater; or
- Land filling.

One of the possible solutions to the chemical stability of the nanofiltration membrane is to look into the use of ceramic membranes, which are becoming more and more popular given their thermal stability, reduced chemical reactivity and their longer lifetimes [35]. However, despite these advantages, they are still expensive and not yet readily available [35].

2.3.1.4 RECENT RESEARCH

Marciano *et al.* [6] recently published the results of a study into nanofiltration of Bayer process solutions in which they used a polysulfone filter with 400 Da (amu) cut-off to treat Bayer liquors. Although they found that the membrane that they used was more than adequate for the filtration process, there is nothing to suggest that a study has been conducted on the life-time of the membrane or on the costs associated with nanofiltration of Bayer liquors for extended periods of time.

2.3.1.5 SUMMARY

There is little doubt that the use of a nanofiltration system could be very effective in the removal of oxalate from Bayer liquors, with Marciano *et al.* [6] reporting the successful application of a nanofiltration technique to a pilot-scale study. However, there has been no further research into the application of this methodology to the treatment of spent Bayer liquor focussing in particular on the disposal of the filtrate, which contains high concentrations of oxalate, humic acids and other organic materials. Given the issue of the disposal of the filtrate, and the limited lifetime of the membranes due to the highly caustic nature and ionic strength of the solution, the application of a nanofiltration system to the treatment of Bayer liquors has some serious shortcomings which need to be resolved before this method of treatment becomes economically viable.

2.3.2 ION EXCHANGE

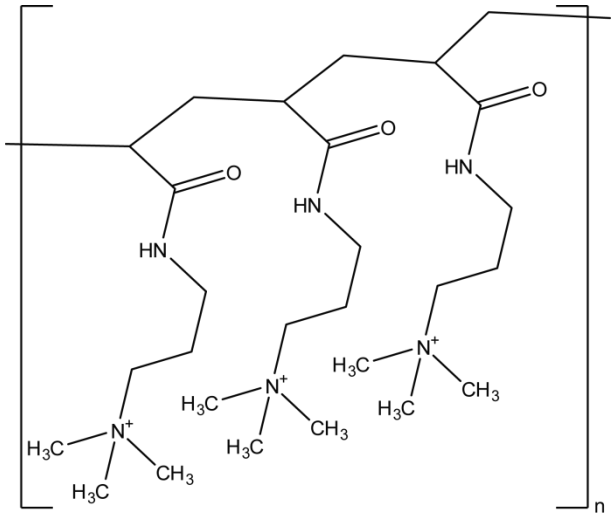

Figure 2.5: Polyacrylic anion exchange resin[2]

2.3.2.1 INTRODUCTION

Ion exchange as a method for treating spent Bayer liquor, appears to have not been studied, with no recorded literature available. Although there are likely to be major issues with the implementation of an ion-exchange system into Bayer Processes, there is little doubt that an ion exchange process would have some advantages when it comes to removing organic contaminants.

2.3.2.2 Advantages

The potential of using an anion exchange resin in the treatment of spent Bayer liquor is based on the ability of a strongly basic anion exchanger to effectively remove oxalate and carbonate ions from the solution. The ion exchangers can then be recycled by treating with sodium hydroxide solution to regenerate them. The other major advantage is that a strongly basic anion exchanger will replace other anionic contaminants with hydroxide anions, replacing caustic lost during the process as well as "cleaning" the liquor for future use.

2.3.2.3 DISADVANTAGES

Unfortunately, there are some major disadvantages to the use of ion exchange resins. The first such disadvantage is that recharging the spent resin is never one hundred percent effective [38, 39]. The second major disadvantage of using strongly basic anionic exchangers is that they are subject to thermal degradation at temperatures above 50 °C. The highly caustic nature of the spent liquor causes irreversible damage to the substrate, which limits the lifetime of the ion exchanger considerably.

The major disadvantage, however, is the deterioration of the resin through various means [38]:

1. Physical movement of the beads in the resin, which reduces the number of active sites for ion exchange.

2. http://www.novasep.com/Technologies/Ion-exchange.asp Accessed 10 September 2009

2. Thermal degradation, believed to be due to the loss of functional group sites due to thermal hydrolysis. Generally, salt-form anionic exchangers are more stable, but basic anionic exchange resins decompose above about 50-60 °C [40].

3. Organic contaminants can undergo chemical reactions within the ion exchange resin, resulting in the production of compounds which may interact with the resin further or may produce more toxic compounds. Sucrose is one of the compounds that has been chemically reacted inside an ion exchange resin [38].

4. Large organic molecules, such as humic and fulvic acids (and their anions) can be non-selectively adsorbed onto the surface of the ion exchange resin, removing exchange sites. This is related to the structure of the ion exchange resin and is irreversible.

2.3.2.4 POTENTIAL

However, despite these disadvantages, there are some considerations which can make the use of an anion exchange resin possible:

- Reillex HPQ anion exchange resin has been shown to be stable to chemical and radiolytic degradation [41].
- Studies [42] have shown that it is possible to prepare anion exchange resins based upon charge separation within the resin, functional group mobility, flexibility and the presence of hydrophilic groups.

2.3.2.5 SUMMARY

Although the use of ion-exchange resins to treat spent Bayer liquors will ensure almost complete removal of anionic contaminants, there are some serious issues which need to be considered. The first of these issues is the possibility of irreversible fouling of the ion exchange materials caused by interactions between the resin and large organic anions; the fact that the recharge of the resin is never 100% effective; There is also the possibility of thermal degradation as well as the prohibitively high cost of maintaining an ion exchange system at an industrial scale.

HYDROTALCITE AND HYDROTALCITE-LIKE ADSORPTION

2.3.3.1 INTRODUCTION

Hydrotalcites are a class of anionic clays that occur both naturally or may be synthetically produced [43-45] which have attracted study since about 1944 [46]. In spite of the extended period of their study, they are generally not as well known as other clays such as the smectite group of minerals [44, 46].

Given the nature of hydrotalcites, there has been considerable amount of research into the possible applications of hydrotalcites, including their use in catalysis, pharmaceuticals and even in polymer chemistry [3, 47, 48]. There has also been considerable research into synthesis procedures used to develop hydrotalcites and hydrotalcite-type compounds [45, 48-55].

2.3.3.2 HYDROTALCITE STRUCTURE

Hydrotalcite compounds have a laminar structure similar to that of the naturally occurring compound Brucite ($Mg(OH)_2$) which is constructed of sheets of $Mg(OH)_2$ structured as octahedral, resulting in hexagonal platelets [56, 57].

By substitution of trivalent metal ions (generally Aluminium [44, 46, 48]) for divalent metal ions in the structure, these layers develop an overall positive charge, which must be neutralised by anions (generally carbonate) being absorbed into the interlayer spaces [46]. Different synthesis methods result in some differences in the crystal structures of these hydrotalcite compounds and their resulting properties and applications [50, 53, 54, 58].

A recent study of the structure of hydrotalcites with differeing aluminium compositions by Sideris *et al.* published in Science in 2008 presented evidence which is suggestive of a honeycomb ordering of aluminium and magnesium atoms in the cationic sheets through the use of multinuclear NMR Spectroscopy [59]. Furthermore, they suggest that changing the prevalence of aluminium (or trivalent) cations in the sheets affects the charge density, which would also have an effect on ion-exchange capabilities, the bonding and orientation of the interlayer species [59].

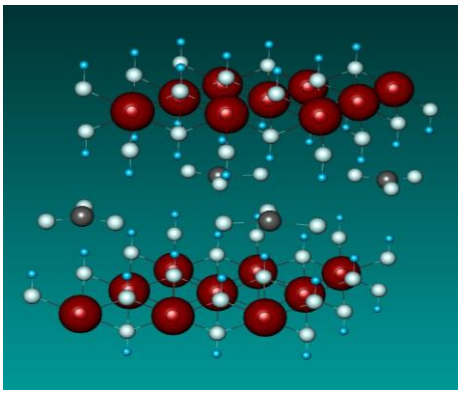

Figure 2.6: Structure of hydrotalcite

There have been a number of studies into the structures of hydrotalcites carried out through the use of X-Ray Diffraction (XRD) [3, 48-58, 60, 61]; Raman Spectroscopy [43, 46, 56]; Scanning Electron Microscopy (SEM) or Transmitting Electron Microscopy (TEM) [50, 52-54, 57, 58, 60]; ThermoRaman Spectroscopy [44]; Infrared Spectroscopy [3, 44, 49, 50, 52, 55, 56, 60]; Thermo-Gravimetric Analysis (TGA) [3, 49, 52, 57, 60]; TGA-DSC (Differential Scanning Calorimetry) [61]; CO_2 and/or N_2 Absorption/Desorption [50-52, 54, 56, 58, 61]; Electron Density Mapping (which is a method of calculating crystal structure, based upon the X-Ray Diffraction data) [57] and ^{27}Al MAS (magic angle spinning) NMR [55].

2.3.3.3 OCCURRENCE OF HYDROTALCITES IN NATURE

There are a number of hydrotalcite compounds that are found in nature. These natural hydrotalcites include, but are not limited to [62, 63]:

Hydrotalcite: $Mg_6Al_2(CO_3)(OH)_{16}\cdot 4H_2O$

Stitchtite: $Mg_6Cr_2(CO_3)(OH)_{16}\cdot 4H_2O$

Pyroaurite: $Mg_6Fe^{3+}{}_2(CO_3)(OH)_{16}\cdot 4H_2O$

Desautelsite: $Mg_6Mn^{3+}{}_2(CO_3)(OH)_{16}\cdot 4H_2O$

Takovite: $Ni_6Al_2(OH)_{16}(CO_3,OH)\cdot 4H_2O$

Reevesite: $Ni_6Fe^{3+}{}_2(CO_3)(OH)_{16}\cdot 4H_2O$

Comblainite: $Ni^{2+}{}_6Co^{3+}{}_2(CO_3)(OH)_{16}\cdot 4H_2O$

Given the highly caustic conditions required for hydrotalcites to form (greater than pH 9), it is rare to find hydrotalcites occurring outside of serpentinites naturally without being some of the by-products of industrial pollution [64].

2.3.3.4 APPLICATIONS OF HYDROTALCITES

Hydrotalcites are compounds that have been extensively studied because of their properties as anionic clays (meaning that they contain anions between the layers) which make them useful in a number of roles as compared to other porous materials which are either cationic or charge neutral [44, 47, 50, 53, 57, 65]:

2.3.3.4.1 Hydrotalcites as catalysts:

Hydrotalcites, due to their layered structure have anionic "bridges" between the positively charged metal-hydroxide sheets, giving them a porous structure, which has been meticulously documented through numerous studies by various instrumental techniques, including XRD, SEM/TEM and Raman Spectroscopy, which are all mentioned above.

Given the flexibility of the composition of hydrotalcite compounds [45] which is due to the large variance in metal ions that can and have been used to modify the surface charge [47], it is possible to vary the anion acting as the pillar and therefore effectively tailor the interlayer space of the hydrotalcite to suit [49, 54, 56]. Given this ability to effectively tailor the hydrotalcite to meet the needs of various applications, gives materials scientists a number of potential uses for these materials [48]. Some of which include:

- Uses in Fluidised Catalytic Cracking Units (FCCUs) [45]
- Supports for noble metal (Pd, Pt) catalysts [45, 48]
- Precursor materials for catalysts through calcining [45, 48].

There have been some studies into tailoring the catalytic properties of hydrotalcite compounds, in which it has been found that increasing the crystal structure and the size of the interlayer spacing tends to increase the catalytic activity of the hydrotalcite [49, 54].

2.3.3.4.2 Ion Exchange and Adsorption

Li and Duan [47], in their extensive review on the applications of hydrotalcite-like compounds noted the potential uses for hydrotalcites in ion exchange and adsorption [47], which has extensively studied and reported [56]. In particular, when dealing with ion exchange and adsorption, they noted that hydrotalcite like compounds had a high uptake of anionic species. However, they noted that if the charge density was too high (due to the presence of trivalent cations) then the uptake of anions decreased. They also observed that the nature of the original anion intercalated between the layers had an effect on ion exchange with carbonate being the most difficult ion to replace. In fact, research presented by Frost and Musemeci [43, 66] found that the presence of atmospheric carbon dioxide may result in the re-adsorption of carbonate into the interlayer and possibly replacing the exchanged anionic pillar.

Li and Duan [47] also noted that there were three main methods of ion exchange and adsorption for hydrotalcites. The first method was ion adsorption onto the surface of the material, which is due to the ionic character of the anion. The second method was direct ion-exchange within the interlayer anions, which can be done either in situ or after the hydrotalcite has been synthesised. The third method discussed was the use of the memory effect of hydrotalcites, which is hydrotalcites reforming their original structure after being calcined and then being placed into a solution containing excess anion [47]. Frost and Musemeci [43, 66] noted that there was some concern that carbonate was the preferential interlayer anion species and that a dry state reaction may result in the readsorption of carbonate into the interlayer.

2.3.3.4.3 Other Applications

Li and Duan [47] (as well as other authors) [3, 43, 45, 47, 54, 56, 60, 61, 66-68] also examine other applications of hydrotalcite materials. Some of these applications include using hydrotalcite compounds as additives in photochemistry, electrochemistry and in functional polymer materials. They have also noted that hydrotalcites are extremely flexible in terms of composition and can be used as drug delivery systems as well as in other applications within the pharmaceutical and biochemical industries [47].

2.3.3.6 SUMMARY

Hydrotalcites are a class of materials with a myriad of applications. The use of a hydrotalcite intercalated with oxalate anions may allow for the selective adsorption and absorption of oxalate from spent Bayer liquors. However, the synthesis of the hydrotalcite may become complicated, with synthesis likely to require the use of a nitrogen atmosphere to prevent the preferential intercalation of carbonate ions.

There is also the probable need for post-treatment of the hydrotalcite in order to regenerate, recycle or dispose of the hydrotalcite material. However, there is enough evidence to suggest that an investigation of the ability of an oxalate-intercalated hydrotalcite to pick up oxalate from Bayer liquors is warranted.

2.4 CONCLUSIONS

Although a number of processes have been considered, some of them (such as ion exchange and nanofiltration) are completely inappropriate for use and others have potential but have serious issues that need to be dealt with before they can be considered as viable alternatives for the treatment of Bayer Process Liquors. Hydrotalcite adsorption/absorption has distinct possibility as a starting point for more advanced adsorption materials for the removal of oxalate anions from Bayer process solutions.

Ion exchange has been noted as being inappropriate for use due to humic and fulvic acid anions masking exchange sites through irreversibly binding to active sites on the resin; as well as issues of membrane solubility whilst under Bayer-type conditions. Nanofiltration was found to be inappropriate due to similar stability issues as well as membrane fouling by humic and fulvic acid anions getting inside the pores and irreversibly blocking them.

Adsorption using hydrotalcites or hydrotalcite-like materials shows promise as adsorption is one of the most commonly used methods to treat contaminated industrial waste waters. As hydrotalcite is an anionic clay, it has the potential to remove most of the anionic contaminants from the solution. Hydrotalcite could also be used as the starting point for more advanced adsorption materials which are specifically designed for the adsorption of oxalate from the spent Bayer liquor.

Chapter 3: Background

3.1 HYDROTALCITE PREPARATION

3.1.1 INTRODUCTION

There has been a wealth of papers published in which hydrotalcites and hydrotalcite-like compounds have been prepared. From an analysis of these papers, it is clear that there are several common (and simple) techniques that can be used to synthesise hydrotalcites and hydrotalcite-like compounds. These techniques range from simple, one-pot synthesis techniques to some more novel methods, including the use of sol-gel techniques [56] and even combustion techniques [55] have been reported.

3.1.2 CO-PRECIPITATION METHOD

The co-precipitation technique for the synthesis of hydrotalcites is reported as the most common [45, 56]. This is due to the co-precipitation method being most compatible with a range of cations, as well as the ease of scaling the synthesis procedure up to industrial scales [45].

$$6Mg(NO_3)_2 + 2Al(NO_3)_3 + 16NaOH + Na_2C_2O_4 + 4H_2O \xrightarrow{N_2} Mg_6Al_2(OH)_{16}(C_2O_4) \cdot 4H_2O + 18NaNO_3$$

Equation 3.1: Preparation of oxalate intercalated hydrotalcite using the co-precipitation method

Preparing hydrotalcites using this method involves the addition of metal cations as their nitrate or chloride salts in the appropriate ratios to a hydroxide solution that has been buffered to a pH of 9. After the hydrotalcite has been formed, the second step in the process is to thermally treat the mother liquor to increase the crystal size and yield of the product.

The first method, which is commonly used, is to heat the mother liquor up to 373 K and allow the solution to stir for a few days in order to promote Dalton Aging; (which is where crystals grow together along edges rather than crystals taking material from other crystals as in Ostwald ripening) whilst the second method involves putting the mother liquor into a hydrothermal bomb and subjecting it to heat and pressures of between 10 MPa and 150 MPa for several days [56].

3.1.3 STRUCTURAL MEMORY EFFECT

Hydrotalcites undergo a number of decomposition steps when heated, eventually forming mixed metal oxides, which are impossible to form through other methods [45]. Hydrotalcite can be reformed by exposing the mixed metal oxide to aqueous solution. The hydrotalcite reforms into its original layered structure, which is where the terminology "structural memory effect" comes from.

It is possible to intercalate any number of anions into the structure of hydrotalcite by the use of the structural memory effect, which is one of the big applications of this method. The major advantage of this method for intercalating hydrotalcites is that almost any anion can be inserted into the interlayer spacing, provided that there is no competition from carbonate, which is by far the preferred interlayer anion and has been suggested to leach into the hydrotalcite over time [43, 66].

$$Mg_6Al_2(OH)_{16}(CO_3)\cdot 4H_2O \xrightarrow{\Delta} 5MgO + MgAl_2O_4 + CO_2 + 12H_2O$$
$$5MgO + MgAl_2O_4 + 13H_2O + C_2O_4^{2-} \xrightarrow{N_2} Mg_6Al_2(OH)_{16}(C_2O_4)\cdot 4H_2O + 2OH^-$$

Equation 3.2: Formation of oxalate intercalated hydrotalcite using the structural memory effect

In order to minimise the intercalation of carbonate back into the hydrotalcite structure, it is common to reform the hydrotalcite structure under an inert atmosphere and using degassed solutions [43, 56, 68]. The use of the structural memory effect is considered to be the optimum method when the anion used is rather large [45, 68], but is not recommended when the intercalating anion is a strong chelator, such as tartrate [45].

3.1.4 ION EXCHANGE METHOD

When a desired anion is not stable in an alkaline solution or a direct reaction between the anion of choice and one of the metals is favoured (for example, a strongly chelating anion such as tartrate), the use of ion exchange in order to intercalate the hydrotalcite is the preferred option. It has also been suggested that the use of the ion exchange method is ideal for the preparation of an intercalated hydrotalcite without the presence of carbonate [45, 56].

A premade hydrotalcite which has monovalent anions such as chloride or nitrate in the interlayer is preferred, but nitrate-intercalated hydrotalcites are more preferred (due to the low charge density of the nitrate anion) [45, 56].

$$Mg_6Al_2(OH)_{16}(NO_3)_2 \cdot 4H_2O + Na_2C_2O_4 \xrightarrow{\Delta} Mg_6Al_2(OH)_{16}(C_2O_4) \cdot 4H_2O + 2NaNO_3$$

Equation 3.3: Preparation of oxalate intercalated hydrotalcite using ion exchange

It is vital to consider the conditions under which the ion exchange is going to take place. For example, careful consideration of the pH at which the ion exchange will occur is important, as the metal hydroxide sheets of the material will start to dissolve if the exchange media is too acidic [56]. It is also important to consider the charge density at the surface of the hydrotalcite (which is related to the identity of the metal ions) as well as selecting a temperature that is not going to affect the structural integrity of the sheets, but also allow for the mobility of the anions in the solution [45, 56]. Furthermore, it is vital to also select the appropriate solvent for the exchange, as exchanging organic anions using an aqueous medium will not result in an optimum ion exchange [56].

3.1.5 RE-CO-PRECIPITATION METHOD

The re-coprecipitation method of making hydrotalcite-type materials is a novel approach to making hydrotalcites intercalated with organic acid anions which was first reported in 2002 [45, 69, 70].

This method involves making a hydrotalcite precursor in the normal manner and then dissolving the hydrotalcite in an excess of aqueous acidic solution of the desired anion at a slightly elevated temperature (usually 323K) until the hydrotalcite has dissolved, followed by re-precipitation in an alkaline solution and reflux to form crystals [45, 69, 70].

$$Mg_6Al_2(OH)_{16}(CO_3)\cdot 4H_2O + 8H_2C_2O_4 \rightarrow 6Mg^{2+} + 2Al^{3+} + CO_3^{2-} + 8C_2O_4^{2-} + 20H_2O$$

$$6Mg^{2+} + 2Al^{3+} + CO_3^{2-} + C_2O_4^{2-} + 16OH^- + 4H_2O \rightarrow Mg_6Al_2(OH)_{16}(C_2O_4)\cdot 4H_2O + CO_3^{2-}$$

Equation 3.4: Formation of oxalate intercalated hydrotalcite using re-co-precipitation

The reported advantage of this technique is that there is no need to take special precautions to prevent the incorporation of carbonate into the interlayer spaces as the carbonate is converted to carbon dioxide during the dissolution stage due to the high pH of the solution while an overwhelming excess of anion during the re-precipitation process appears to prevent the intercalation of carbonate ions [69, 70].

This option may prove to be useful for the industrial scale preparation of anion-intercalated hydrotalcites for use as catalysts, as there is no need to prevent carbon dioxide (and therefore carbonate ions) from being present during the reaction.

3.1.6 SUMMARY

The most viable options for the preparation of the hydrotalcite materials in this study are using the co-precipitation method to prepare the hydrotalcite starting materials, along with the use of co-precipitation and re-co-precipitation methods for the preparation of the oxalate intercalated hydrotalcites. Although the use of the structural memory effect can be used for the intercalation of oxalate into the hydrotalcite structure, the requirement that it be prepared at elevated temperature, followed by intercalation under a nitrogen atmosphere is likely to cause some problems. Furthermore, the use of ion exchange to prepare oxalate intercalated hydrotalcites is not likely to show very good results unless it too, is done under a nitrogen atmosphere at set conditions of temperature and pH.

3.1.7 SURFACE PROPERTIES

There are two surface properties which are of importance in this study, being specific surface area and surface charge density. Understanding these two properties is going to allow the formation of an understanding of how adsorption occurs between the contaminants in Bayer liquors and hydrotalcite.

3.1.8 SPECIFIC SURFACE AREA

The specific surface area is the first surface property to be examined and it has been linked to the adsorption capacity of materials. As such, it can be considered to be important to examine the specific surface area of the materials during the adsorption studies. Developing an understanding of specific surface area, and linking this property to the adsorption capacity of the materials may provide clues to maximising adsorption capacity of future materials.

The specific surface area is found by [71] using:

$$S = q_e N \Omega$$

Equation 3.5: Specific surface area

Where: S = Specific Surface are (m^2/g)
q_e = Target Species adsorbed at equilibrium (mol)
N = Avogadro's number ($6.02x10^{23}$)
Ω = Area occupied by one molecule of the target species

3.2 ADSORPTION PROCESSES

3.2.1 INTRODUCTION

Adsorption is the process of sorbing atoms, ions or molecules onto a surface by either chemical or physical interactions [72]. There are two major types of adsorption: physical and chemical adsorption.

Physical adsorption (physiosorption) is adsorption occurring by physical means, usually Van Der Waals interactions between the sorbent and sorbate (target molecule). These interactions generally occur at long range but are weakly binding [72], meaning that the process is easily reversible.

Chemical adsorption (chemisorption) is based upon chemical bonds forming between sorbent and sorbate, which are usually covalent in nature. Until recently, it was thought that chemisorption could only occur through exothermic processes [72].

In recent years, the body of literature into the use of adsorbents for the treatment of contaminated waters has grown as adsorbents have generally be found to be more applicable than other techniques, cheaper and as efficient [71, 73-79].

Despite the increase in the number of studies into using various materials as adsorbents, the number of studies examining the adsorption processes has not progressed much further than the assumptions of monolayer adsorption suggested in Langmuir, Freundlich and Dubinin-Radushkevich (D-R) adsorption models [74, 80-86].

Erin and Afsin [87] in their study of metal adsorption onto bentonite suggested that ion exchange reactions occur at the active sites as well as the possibility of metal complexes being formed with surface hydroxyl groups of the material.

3.2.2 LANGMUIR ADSORPTION

The Langmuir adsorption model (Suggested by Irving Langmuir in 1916) is the simplest explanation of adsorption processes onto the surface of a material, and it is built around four base assumptions [72, 83]:

5. Each active site can only accept one molecule;
6. Sorbed molecules form a monolayer;
7. All active sites are energetically equivalent; and
8. There is no interaction between sorbed molecules.

This allows for the calculation of the adsorption capacity of a material at equilibrium (q_e) through the use of the Langmuir adsorption isotherm [72, 85]:

$$q_e = \frac{K_L C_e}{1 + aC_e}$$

Equation 3.6: Langmuir adsorption isotherm

Where: q_e = adsorption capacity at equilibrium (mg/g)
K_L = Langmuir constant
a = energy of adsorption
C_e = concentration of target species at equilibrium

However, in practise, the adsorption capacity (q_e) is found by measuring concentration change as the solution comes to equilibrium with the adsorbent and the solution containing the target species and by comparing that concentration change to the concentration of the adsorbent slurry in the system [85]:

$$q_e = \frac{c_i - c_e}{s}$$

Equation 3.7: Adsorption capacity

Where: q_e = adsorption capacity
c_i = initial concentration of target species in solution (mg/L)
c_e = equilibrium concentration of target species in solution (mg/L)
s = slurry concentration of adsorbent (g/L)

By knowing the adsorption capacity (q_e) of the adsorbent and the equilibrium concentration (c_e) of the target species it is possible to find the Langmuir constant (K_L) and the Langmuir energy constant (a) by plotting [74, 85]:

$$\frac{c_e}{q_e} \text{ vs. } c_e$$

Where: c_e = equilibrium concentration of the target species
q_e = adsorption capacity of the material

This should give a linear plot according to the relationship [74, 85]:

$$\frac{c_e}{q_e} = \frac{1}{K_L} + \frac{a}{K_L} c_e$$

Where: c_e = equilibrium concentration of the target species
q_e = adsorption capacity of the material
K_L = Langmuir constant
A = energy of adsorption

From this relationship, the slope of the plot being $\frac{a}{K_L}$ and the intercept being $\frac{1}{K_L}$.

It is also possible to find the maximum adsorption capacity of the material by the relationship [84]:

$$\frac{1}{q_e} = \frac{1}{q_m} + \frac{1}{K_L q_m c_e}$$

Equation 3.8: Theoretical maximum adsorption capacity

Where: q_e = adsorption capacity at equilibrium
q_m = maximum adsorption capacity
K_L = Langmuir constant
c_e = concentration of target species at equilibrium

This is done by plotting $\frac{1}{q_e}\ vs. \frac{1}{c_e}$ which gives an intercept of $\frac{1}{q_m}$.

It is also possible to use the Langmuir model of adsorption to determine the favourability of adsorption according to the relationship [77, 80]:

$$K_R = \frac{1}{1 + K_L c_i}$$

Equation 3.9: Separation factor

Where: K_R = separation factor
K_L = Langmuir constant
c_i = initial concentration of target species

The separation factor (K_R) tells us if adsorption is:

- Unfavourable (K_R is greater than one);
- Favourable (K_R is between 0 and 1);
- Linear (K_R equals 1); or
- Irreversible (K_R equals 0).

3.2.3 FREUNDLICH ADSORPTION

The Freundlich adsorption isotherm is based on the assumption that the number of active sites available for adsorption is dependent upon the concentration of sorbate particles. That is, as the concentration of the target species increases, then the number of available active sites increases until the point of surface saturation is reached [74, 80, 81] and is of the form:

$$q_e = K_F {c_e}^{1/n}$$

Equation 3.10: Freundlich adsorption isotherm

Where: q_e = adsorption capacity
K_F = Freundlich constant
c_e = concentration of target species at equilibrium
$1/n$ = adsorption intensity

That makes it possible to determine K_F (intercept) and $1/n$ (slope) according to the relationship [74, 85]:

$$\log q_e = \log K_F + 1/n \log c_e$$

Where: q_e = adsorption capacity
K_F = Freundlich constant
n = adsorption intensity
c_e = equilibrium concentration of target species

When $1/n$ is less than 1, it is suggestive that the active sites are heterogeneous and thus have different energy levels. If $1/n$ is equal to or greater than one, it is suggestive of homogeneous active sites (all active sites have the same energy levels.)

3.2.4 DUBININ-RADUSHKEVICH ADSORPTION

The Dubinin-Radushkevich (D-R) isotherm can be used to determine the adsorption energy (E) of the material as well as predict the maximum adsorption capacity (q_m) of the material.

From the calculated adsorption energy, it is possible to determine if the adsorption process is a physical or a chemical reaction between active sites on the adsorbent and the adsorbate.

The D-R isotherm is generally given as [88, 89]:

$$q_e = q_m e^{(-B\varepsilon^2)}$$

Equation 3.11: Dubinin-Radushkevich adsorption isotherm

Where: q_e = adsorption capacity at equilibrium
q_m = maximum adsorption capacity
B = a constant related to the energy of adsorption
ε = Polanyi potential:

While the Polanyi potential is generally given as:

$$\varepsilon = RT \ln\left(1 + \frac{1}{c_e}\right)$$

Equation 3.12: Polanyi potential

Where: ε = Polanyi Potential
R = gas constant (8.3145 J/mol/K)
T = temperature (K)
c_e = equilibrium concentration of the target species

It is possible to work out q_m (intercept) and B (slope) from the linear plot of $q_e \; vs. \; \varepsilon^2$ [88, 89]. From there, it is possible to determine the energy of adsorption through the relationship [88, 89]:

$$E = \sqrt{2B}$$

Equation 3.13: Energy of adsorption

Where: E = energy of adsorption (kJ/mol)
B = constant related to the energy of adsorption

From E, it is possible to determine if adsorption is a physical process (E is less than 8 kJ/mol); chemical ion exchange (E is between 8 and 16 kJ/mol) or by chemical bond formation between the adsorbate and adsorbent [88, 89].

3.2.5 TOTH ADSORPTION

The Toth isotherm is an adsorption isotherm that assumes that they distribution of available active sites is skewed towards lower energies and is of the form [86]:

$$q_e = \frac{K_T c_e q_m}{(1 + (K_T c_e)^n)^{1/n}}$$

Equation 3.14: Toth adsorption isotherm

Where: q_e = adsorption capacity at equilibrium
K_T = Toth constant
c_e = concentration of target species at equilibrium
q_m = maximum adsorption capacity
n = intensity of adsorption

As most adsorption studies involving clay-type minerals find that the Langmuir isotherm most accurately models the adsorption processes involved in adsorption treatment of contaminated waters, it can be assumed that the energy distribution of active sites in the clay materials are uniform and therefore the Toth isotherm is not applicable.

3.3 HYDROTALCITE AND HYDROTALCITE-LIKE ADSORPTION

3.3.1 INTRODUCTION

Hydrotalcite adsorption has become more and more popular in recent times as an adsorbent for anion-contaminated waters due to the ability of these materials to adsorb anions. Goh, Lim and Dong [90] as well as Wang *et al.* [91] suggest that there are three reasons for the study of hydrotalcite materials for adsorption studies:

9. High surface area of the hydrotalcite;
10. Flexible interlayer region (allowing for intercalation with different anions); and
11. High anion exchange capacity (although this point is refuted in Mandal and Mayadevi [92].)

As there are these advantages to the use of hydrotalcite adsorbents, there have been several studies into the adsorption behaviour of these materials with three mechanisms being proposed [90]:

1. Surface adsorption;
2. Interlayer anion exchange; and
3. Reconstruction of calcined hydrotalcite-like materials. (This will be covered later in more detail.)

Furthermore, kinetic studies have shed more light on the likely processes of adsorption have suggested that the process occurs through the following stages [90]:

- External mass transfer;
- Intra-particle diffusion; and
- Chemisorption reactions at phase boundaries.

Although it is discussed later, it is suggestive that the fast step of adsorption is most likely to be the mass transfer stage, with intra-particle diffusion being the rate-limiting step to equilibrium.

3.3.2 DESCRIBING ADSORPTION

Goh, Lim and Dong [90] noted that there have been a number of adsorption isotherms used to describe the adsorption process onto hydrotalcites, with the most popular adsorption isotherm being the Langmuir isotherm, followed by use of the Freundlich isotherm before the use of modified Langmuir isotherms [90, 93], which can be considered as a function of their applicability to real-world adsorption systems.

The use of Langmuir adsorption isotherms to explain adsorption processes is suggestive of the formation of a monolayer of adsorbed particles around the hydrotalcite's active sites (areas where there is a localised partial positive charge which allows interactions between sorbate and sorbent molecules). The use of Freundlich adsorption isotherms to describe the behaviour of hydrotalcite adsorbents suggests that there is a narrow distribution in energy levels of the active sites, which is a basic tenant of the Freundlich adsorption isotherm.

3.3.3 KINETICS OF ADSORPTION

The general kinetics of adsorption, as reported by Goh, Lim and Dong [90] in their review of hydrotalcite adsorption suggest that initial adsorption proceeds quite quickly (sometimes as quickly as 15 minutes for initial adsorption to complete) which is suggestive of external mass transfer and the time to equilibrium (which has been reported as being up to three days) is indicative of intra-particle diffusion.

Goh, Lim and Dong [90] also noted that there have been a number of kinetic models used to describe the kinetics of adsorption, with studies showing a variety of kinetics models, such as first order kinetics [94]; second order kinetics [95]; as well as intra-particle diffusion and other models used to describe the adsorption behaviour of these materials.

3.3.4 FACTORS AFFECTING ADSORPTION

There are a number of factors that can have an effect on the rate of adsorption onto hydrotalcites. The major influences include pH; the presence of competitive anions and interlayer ion charge. Each of these factors has a different effect.

Effect of pH

The effect of pH, as described by Goh, Lim and Dong [90], is generally dependent upon both the species of the anion as well as the species of hydrotalcite used in the tests, as shown in nearly all of the studies recorded here [92-96]. However, it is generally considered that increasing pH results in a decrease of adsorption efficiency, and this has been linked to increased competition between the target anion and hydroxide anions. This perception is supported by Das *et al.* as well as Lv *et al.* [94] although Mandal and Mayadevi [92] found little correlation between pH and absorption efficiency for the uptake of fluoride ions from water.

Competitive Anions

Das *et al.* [96] in their study of phosphate pickup in solution found that the presence of competing anions decreased the adsorption efficiency of the hydrotalcite. Furthermore, they went on to suggest that the competitive adsorption of anions onto hydrotalcites was dependant on the charge density of the anions is a significant contributor to the competitive adsorption of anions.

Goh, Lim and Dong [90] in their review of hydrotalcite adsorption only commented in general about the competitive adsorption of anions, noting that divalent anions were more likely to be adsorbed than monovalent anions, with the general order of competitive effect being along the order of:

$$HPO_4^{2-} > SO_4^{2-} > CO_3^{2-} > F^- > Cl^- > Br^- > NO_3^-$$

Interlayer Ion Charge

Although it is generally accepted that the carbonate form of hydrotalcite is the overwhelmingly favoured product, hydrotalcites with chloride and nitrate in the interlayer have been prepared through the use of special conditions, including synthesis under nitrogen atmosphere.

Goh, Lim and Dong [90] postulated that the overwhelming favour for the formation of a carbonate intercalated hydrotalcite is most likely due to:

- Strong electrostatic forces of attraction between the metal hydroxide layers and the carbonate anions; and
- Formation of a prismatically-structured interlayer in which the planes of the CO_3^{2-} anions are parallel to the interlayer.

3.3.5 STRUCTURAL MEMORY EFFECT

It has been suggested that strong interactions between metal oxides and carbonate ions contribute to the low adsorption capacity of hydrotalcite-type compounds [96]. As a result of this, the use of the structural memory effect (in which hydrotalcites reform their structures after being added to water) has been shown to improve the efficiency of contaminant anion pickup and become the major method of anion removal in hydrotalcite adsorption in recent times.

Goh, Lim and Dong [90] found that thermogravimetric analysis (TGA) of hydrotalcite-type materials showed:

- Loss of water below 200 °C;
- Loss of water and carbon dioxide between 250 °C-450 °C;
- Loss of hydrotalcite structure between 450 °C-500 °C; and
- Irreversible structural change over 800 °C.

Furthermore, studies into hydrotalcite adsorption have shown that calcined hydrotalcites have:

- Highly active mixed metal oxides [90];
- High thermal stability [90];
- Larger surface area than uncalcined hydrotalcite [90, 92];
- Alkaline properties [90];
- Small crystal size [90];
- Stability against sintering (formation of metal powder) [90];
- Reformation of structure upon hydration [90]; and
- Better anion adsorption than normal hydrotalcite [90, 96].

The better adsorption capacity of calcined hydrotalcites has been suggested to be caused by 3 factors:

1. Increased surface area [90, 92];
2. Higher porosity [90]; and
3. Fewer carbonate anions in the interlayer spaces [90].

However, Wang *et al.* [91] hypothesised that the improved efficiency of the calcined hydrotalcite is due to the processes of dehydroxylation, decarbonation and formation of mixed metal oxides.

Goh, Lim and Dong [90] go on to further suggest that the mechanism by which the anion adsorption is increased via the memory effect is due to the anion being incorporated into the structure during reformation, rather than through ion exchange after the structure has formed.

3.3.6 GENERAL CRITICISMS OF HYDROTALCITE ADSORPTION STUDIES

Goh, Lim and Dong [90] performed a review of hydrotalcite adsorption studies and noted that there were several factors that needed to be taken into account when considering the applicability of hydrotalcite adsorption methods, most importantly:

- The researcher's use of single-component systems to simulate wastewaters (that is, the oversimplification of the adsorption matrix to an unrealistic system); and

- The use of inert atmospheres (typically nitrogen) during adsorption tests (once again oversimplifying the adsorption system matrix to an unrealistic representation of the wastewater system).

3.4 KINETICS

Kinetic studies of adsorption processes have found that adsorption occurs in three distinct phases [81]:

Phase 1: Fast adsorption; which occurs when all of the active sites are free and fixing anions to the material is easy.

Phase 2: Slow Adsorption; which occurs after the main adsorption sites have been occupied and repulsive forces start acting between adsorbed ions and ions in the surrounding solution. This results in further adsorption interactions requiring more energy in order to force the process to continue.

Phase 3: Equilibrium; which occurs when all of the available adsorption sites have been filled and equilibrium has been established between the adsorbed ions and ions in solution.

A study of the kinetics behind the adsorption processes involved in the adsorption of anions from Bayer liquors should yield some information on how the adsorption occurs, including how adsorption is affected by the concentration of various contaminants within the liquor as well as potentially providing some clues as to the possible mechanisms behind the adsorption process.

3.4.1 FIRST ORDER KINETICS

The first model of kinetics that will be examined is the applicability of first order kinetics to the rate of adsorption of contaminant upon Bayer liquors. This relationship will be explored by developing Lagergren plots ($\ln(q_e - q_t)\ vs.\ t$) according to the relationship [77, 97]:

$$\ln(q_e - q_t) = \ln qe - k_1 t$$

Equation 3.15: First order kinetics model

Where: q_e = amount of target species adsorbed at equilibrium
q_t = amount of target species adsorbed at time t
t = time
k_1 = first order rate constant

From the Lagergren plot, the first order rate constant (k_1) is found from the slope of the graph.

3.4.2 SECOND ORDER KINETICS

Testing for second order kinetics will initially be performed by preparing plots of $\frac{t}{q_t}\ vs.\ t$

The formation of a linear plot shows that the reaction follows second order kinetics [77, 97] according to the relationship:

$$\frac{t}{q_t} = \frac{1}{k_2 q_e^2} + \left(\frac{1}{q_e}\right) t$$

Equation 3.16: Second order kinetic model

Where: t = time
q_t = amount of target species adsorbed at time t
q_e = amount of target species adsorbed at equilibrium
k_2 = second order rate constant

However, the application of the Elovich equation [97] and plotting $q_t\ vs. \ln t$ will give the initial adsorption rate (α) (from the intercept) as well as the desorption constant (β) (from the slope) due to the relationship:

$$q_t = \beta \ln(\alpha\beta) + \beta \ln t$$

Where: α = initial adsorption rate
β = desorption constant
t = time

Which comes from the Elovich equation for second order kinetics [77]:

$$\frac{dq_t}{dt} = \alpha e^{(-\beta q_t)}$$

Where: α = initial adsorption rate
β = desorption constant
q_t = amount of target species adsorbed at time t

3.4.3 INTRA-PARTICLE DIFFUSION

As there is the possibility that adsorption of the contaminants found within the Bayer liquor may be controlled by intra-particle diffusion, it is essential to determine that this is not the rate limiting step. This will be done by drawing a plot of $q_t \; vs. \sqrt{t}$.

If the plot passes through the origin and is linear, then it can be assumed that intra-particle diffusion plays a significant role in the rate of adsorption for the material and the rate constant can be determined from the slope of the plot according to the relationship [77, 97]:

$$q_t = k_i\sqrt{t}$$

Equation 3.17: Intra-particle diffusion model

Where: q_t = amount of target species adsorbed at time t
k_i = rate constant for intra-particle diffusion
t = time

Chapter 4: Experimental Procedures

4.1 ADSORBENT PREPARATION

4.1.1 HYDROTALCITE

All hydrotalcite and precursor hydrotalcite materials were prepared using a co-precipitation method.

Initially, a metal ion solution containing 0.25 M aluminium chloride and 0.75 M magnesium chloride was prepared by dissolving the appropriate amount of metal salt into ultrapure (18.2 MΩ) water. In addition to the metal salts, a small amount of sodium carbonate (1.5 g) was also added to ensure the intercalation of carbonate into the hydrotalcite.

A 50 % w/v sodium hydroxide solution was prepared be adding the appropriate mass of anhydrous sodium hydroxide to the appropriate volume of water slowly. The solution was allowed to cool before being diluted to the appropriate volume.

The metal ion solution was then added to the sodium hydroxide solution at a rate of 10 cm^3 per minute via the use of a peristaltic pump with care being taken to ensure that the pH was maintained over 10. After the metal ions had been added to hydroxide solution, the hydrotalcite was aged at a temperature of 75 to 80 °C for 18 hours.

After the sample had been aged for twenty four hours, it was vacuum filtered and washed with boiling water until the addition of a small amount of silver nitrate solution to the filtered liquor indicated that there was no chloride present. The sample was then dried under vacuum and crushed using a mortar and pestle.

4.1.2 THERMALLY ACTIVATED HYDROTALCITES

Thermally activated hydrotalcites were prepared by taking the appropriate amount of hydrotalcite precursor material; placing it into a ceramic crucible and heating it at 280 °C for a period of 24 hours. A temperature of 280 °C was selected from examination of the TGA data for the temperature of maximum weight loss (see section 5.1.5 on page 60) and the optimum treatment time was determined by examining the mass loss as a function of time at the temperature of maximum weight loss (see section 5.1.8 on page 64)

After the sample had been heated, it was immediately placed under vacuum to ensure minimum contact with atmospheric carbon dioxide before use.

4.2 OXALATE INTERCALATED HYDROTALCITES

As hydrotalcite has a very high affinity for carbonate (intercalating carbonate before any other ion) special preparation techniques were required to minimise the possibility of carbonate being incorporated into the hydrotalcite material. For this reason, two methods of preparation were used: *in-situ* intercalation and re-co-precipitation.

4.2.1 CO-PRECIPITATION METHOD

Initially, a metal ion solution containing 0.25 M aluminium chloride and 0.75 M magnesium chloride was prepared by dissolving the appropriate amount of metal salt into ultrapure (18.2 MΩ) water along with an excess of sodium oxalate. The solution was then degassed using a Schlenk line with repeated vacuum cycles and maintained under an inert atmosphere for two hours before being added to the hydroxide solution.

A 50 % w/v sodium hydroxide solution (used in order to minimise presence of carbonate in the solution) was prepared by adding the appropriate mass of anhydrous sodium hydroxide to the appropriate volume of water slowly. The solution was allowed to cool before being diluted to the appropriate volume and being degassed as above by using a Schlenk line and being stored under an inert atmosphere for a minimum of two hours before further use.

The sodium hydroxide solution had metal ion solution added to it at a rate of 10 cm^3 per minute via peristaltic pump with the pH maintained above 10. After the addition of the metal ions, the hydrotalcite was aged at 80 °C for 18 hours under an inert atmosphere.

The hydrotalcite was vacuum filtered and washed with boiling water using a Schlenk filter. Chloride was then tested for using dilute silver nitrate solution before being dried under vacuum using the Schlenk filter and crushed using a mortar and pestle under an inert atmosphere in a glove bag.

4.2.2 RE-CO-PRECIPITATION METHOD

The use of the re-co-precipitation method does not require the use of inert atmosphere (as previously noted), and as such makes this method worth testing. A modified re-co-precipitation method was used as dissolution of the hydrotalcite precursor using oxalic acid resulted in magnesium oxalate precipitating out of the solution.

Initially, slurry was prepared using 100 cm^3 of ultrapure water for every 10 g of precursor hydrotalcite, followed by heating to 75 °C. The hydrotalcite sample was then dissolved by the drop-wise addition of concentrated nitric acid.

After dissolution, an oxalic acid solution (9.0 g in 100 cm^3 water) was added to the dissolved hydrotalcite, followed by the slow addition of 50 %w/v sodium hydroxide solution until a pH of 10 was maintained. The material was then allowed to age for 24 hours at 75 °C before being vacuum filtered and washed with a minimum of boiling water and being dried under vacuum.

After the sample was dried, it was crushed using a mortar and pestle and immediately stored under vacuum.

4.3 MATERIAL CHARACTERISATION

4.3.1 X-RAY DIFFRACTION (XRD)

X-ray Diffraction of the powdered samples was performed using a Phillips PANalytical X'pert PRO using a copper anode at 40 keV and 40 mA without a monochromator. All samples were analysed using a parallel beam configuration with a step size of 0.02 °2θ, with 0.5 seconds between steps on a continuous scan between the angles of 3 and 75 °2θ in order to ensure that changes in peak position were not an artefact of variations of the height of the sample stage.

The instrument was set up with a fixed divergence slit of 0.4354 ° and a specimen length of 10 mm and a receiving slit size of 0.100 mm. The distance to the receiving divergence slit from the sample was 100 mm and the overall Goniometer radius was 240 mm.

Figure 4.1: Inert atmosphere XRD stage

In order to prevent carbon dioxide from the air reacting with the prepared materials (either thermally activated hydrotalcites or oxalate intercalated hydrotalcites and including the precursor hydrotalcites), a special inert atmosphere XRD stage was used, as shown above in **Figure 4.1**. Each sample was placed into the stage whilst under a nitrogen atmosphere and the stage was then sealed. The sample was then placed into the XRD and analysed within thirty minutes of being prepared.

4.3.2 INFRARED SPECTROSCOPY (IR)

Infrared spectra were collected using a Nicolet 870 FTIR equipped with a Smart Endurance ATR accessory with a diamond window. The spectrum was taken over a range from 4000 cm^{-1} to 565 cm^{-1} with 64 scans being co-added at a resolution of 4 cm^{-1} and a mirror velocity of 0.6329 m/s.

After collection of the background spectrum, a small amount of powdered sample was placed onto the sample window and analysed before ATR correction was then applied.

4.3.3 RAMAN SPECTROSCOPY

Raman spectra of the samples were collected using a Renishaw micro-Raman system using a 633 nm Laser between wave numbers 100 and 4000 cm^{-1} with a resolution of 4 cm^{-1} with 100 scans being coadded together to form the sample spectrum.

Spectra collection was performed by placing a small amount of powdered sample onto the sample stage and focussing the laser beam.

4.3.4 INFRARED EMISSION SPECTROSCOPY (IES)

Infrared emission spectroscopy was carried out on a Nicolet Nexus FTIR instrument over a temperature range of 100-600 °C with 1024 scans being co-added below 200 °C, 512 scans being co-added to 300 °C; 256 scans being co-added to 400 °C for the and 128 scans co-added from 400-600 °C over the spectral range 650-4000 cm^{-1}. Temperatures were stepped in 50 °C steps with a 600 second equilibrium time between measurements.

Background measurements using a graphite sample and the titanium stage were analysed before a small amount of powdered sample was then placed onto the stage and analysed.

4.3.5 BRUNAUER, EMMETT AND TELLER (BET) SURFACE ANALYSIS

BET analysis was performed on a Tristar 3000 BET machine which used a liquid nitrogen bath, and 3/8 inch diamater sample tubes. After the tube had been weighed, approximately 100 mg of sample was placed inside the tube and dried at 105 °C overnight under flowing nitrogen to accurately determine the dry sample weight.

The sample was then analysed using a 99 data point analysis method of a range of nitrogen gas pressures, which was used to determine the BET surface area, the Langmuir surface area and average pore diameter.

4.3.6 SCANNING ELECTRON MICROSCOPY (SEM)

Samples were prepared for SEM imaging by placing a small amount of powdered sample onto an SEM stub and coating the sample with gold before analysis.

The instrument used was an FEI Quanta SEM operating at conditions of 25 kV with a spot size of 3.5. The current was not recorded as EDX patterns were not collected.

4.3.7 TRANSMISSION ELECTRON MICROSCOPY (TEM)

Samples were prepared for TEM imaging by dispersing a very small amount into ethanol by sonicating for 15 minutes at low power. A drop of the sample was then dispersed onto the copper sample grid with a holey film and the ethanol was allowed to evaporate.

The instrument used was a Phillips CM200 operating at 200 kV with a lanthanum boride (LaB_6) cathode and a nominal camera length of one metre.

4.3.8 THERMOGRAVIMETRIC ANALYSIS (TGA)

Thermogravimetric analysis was performed by accurately weighing approximately 30 mg of sample onto the platinum pan. The sample was allowed to equilibrate at room temperature for 10 minutes before being heated at 5 °C per minute up to a temperature of 1000 °C under a nitrogen atmosphere using a Q500 TGA instrument. At the end of the run, the temperature of the pan was allowed to equilibrate to 300 °C before the furnace was opened to the atmosphere.

4.4 ADSORPTION STUDIES

4.4.1 SAMPLE PREPARATION

Hydrotalcite Adsorbents

Adsorbents were prepared by washing hydrotalcite samples with freshly boiled water and filtering the solution to eliminate any contaminants on the surface of the material. The hydrotalcites were then dried and the appropriate amount was placed into a sample tube and stored.

Thermally Activated Adsorbents

Thermally Activated Hydrotalcite samples were prepared from the previously prepared hydrotalcite samples and heating in a furnace at 280 °C for 24 hours. After thermal treatment, the samples were placed in a dessicator and allowed to cool until use.

4.4.2 SAMPLE ANALYSIS

TOC ANALYSIS

TOC analysis was performed on samples using a Shimadzu TOC with TN attachments and an ASI 5000 autosampler using 40 mL sample tubes.. The carrier gas was zero grade air to ensure no carbonate interference.

Full TOC analysis was performed using a total carbon (TC) and inorganic carbon (IC) analysis. Plots were prepared of detector response vs. carbon concentration using sodium oxalate/sodium carbonate standards and these were used to determine the concentrations of the carbonate and oxalate in the adsorption solutions.

CARBONATE ANALYSIS BY TITRATION

Due to instrument failure, the carbonate concentrations in the carbonate adsorption study were determine by the use of titration against 0.1 M hydrochloric acid using methyl orange indicator.

The hydrochloric acid was standardised against a 0.0978 M sodium carbonate solution which was prepared by dissolving 1.0361 g of anhydrous sodium oxalate in 100 cm^3 ultrapure water.

3 cm^3 Samples from the adsorption solutions were taken and titrated against the standardised hydrochloric acid. All titrations were replicated until there was less than 0.05 cm^3 variation between samples. The carbonate concentrations were then calculated using the titration data.

OXALATE ANALYSIS BY TITRATION

Due to an issue of oxalate being kinetically hindered under thermal decomposition during TOC analysis, the oxalate concentrations were determined by titration using potassium permanganate solution.

The potassium permanganate solution was prepared by dissolving 0.8 g potassium permanganate into a 500 cm^3 volumetric flask before a 20 cm^3 aliquot was taken and diluted into a 2000 cm^3 volumetric flask. This solution was then standardised against 1.000 g/dm^3 sodium oxalate

5 cm^3 sample aliquots were taken from the adsorption solutions and 5 cm^3 concentrated sulphuric acid was added to the sample to ensure that the samples were acidified. Samples were then heated using an electronic hot plate to boiling before being titrated against the standardised potassium permanganate solution.

4.4.3 ANHYDROUS SODIUM OXALATE AND SODIUM CARBONATE PREPARATION

Anhydrous sodium carbonate and sodium oxalate used as the primary standards for this research were prepared by weighing out approximately 50 g of each chemical into an evaporating basin and placing in an oven at 150 °C for three hours to drive off any water. After being removed from the furnace, the sodium oxalate and sodium carbonate samples were then allowed to cool to room temperature underneath vacuum and stored until use.

4.4.4 OXALATE STANDARD SOLUTION PREPARATION

Standards were prepared by accurately weighing out the appropriate mass of pre-dried and dehydrated anhydrous sodium oxalate and sodium carbonate to make a stock solution of 15 g/L sodium carbonate and 2.5 g/L sodium oxalate and dissolving them in water that had been freshly boiled for 15 minutes. After the standards had been dissolved, the solution was allowed to cool before being made up to the mark using ultrapure water that had been boiled and allowed to cool.

The other standards were then prepared by serial dilution of the stock solution to make the standard solutions shown in **Table 4.1** below.

Standard	Carbonate		Oxalate		Total Carbon Content
	ppm CO_3^{2-}	ppm C	ppm $C_2O_4^{2-}$	ppm C	ppm C
0	0	0	0	0	0
1	170	34	33	9	43
2	340	68	66	18	86
3	510	102	99	27	129
4	679	136	132	36	172
5	849	170	164	45	214

Table 4.1: Standard Concentrations for both Ions and Carbon in PPM

Calibration curves were prepared by preparing the standards outlined in **Table 4.1** above and being analysed for total carbon (TC) and inorganic carbon (IC) content. From the data collected, a graph of detector response against concentration was prepared and checked for linearity before being used to determine the concentration of the sample solutions. The standard solutions were exposed to the same sample handling techniques as the sample solutions.

4.4.5 OXALATE TEST SOLUTION PREPARATION

The oxalate test solution was prepared by accurately weighing and dissolving 1.05 g of sodium oxalate that had been dehydrated into a 500 cm^3 volumetric flask and dissolving in freshly boiled (and degassed) ultrapure water. The solution was allowed to cool to room temperature before making up to the mark with ultrapure water.

4.4.6 ADSORPTION TESTING PROCEDURES

A number of adsorption studies were performed using both an equilibrium approach (for hydrotalcites) and a kinetic approach for the thermally activated hydrotalcites. A summary of the experiments is shown in **Table 4.2** below.

Adsorbent	Solution	Type of Study
Hydrotalcite	$C_2O_4^{2-}$	Equilibrium
TAHT	$C_2O_4^{2}$	Kinetic
Hydrotalcite	$C_2O_4^{2-}/CO_3^{2-}$	Equilibrium
TAHT	$C_2O_4^{2-}/CO_3^{2-}$	Kinetic
Hydrotalcite	CO_3^{2-}	Equilibrium

Table 4.2: List of adsorption study experiments

Equilibrium Study Approach: Hydrotalcites

Equilibrium studies were performed by preparing a stock solution containing 2.000 g/l sodium oxalate and then serial diluting to the concentrations required (see **Table 4.3** below). Samples were then placed in sealed Schott flasks and 1.000 g of hydrotalcite adsorbent was then placed into the solution. A blank experiment without any hydrotalcite adsorbent was prepared using the same methodology.

Adsorption solutions	Oxalate concentration (ppm)	Carbonate Concentration (ppm)
A	131.35	141.99
B	114.93	124.24
C	98.51	106.49
D	82.09	88.74
E	65.67	71.00
F	49.96	53.25
G	32.84	35.49

Table 4.3: Initial oxalate solution concentrations for equilibrium studies

A carbonate solution adsorption study was also prepared using initial sodium carbonate concentrations as shown in **Table 4.3** above. These solutions were prepared by serial dilution of a stock carbonate solution. A mixed oxalate/carbonate adsorption study was also prepared using the concentrations outlined in **Table 4.3** above for both oxalate and carbonate.

Once the hydrotalcite adsorbent had been placed into the sample and the Schott flask was sealed, the experiments were placed in a shaking water bath at 25 ºC and shaken at 50 rpm for three and a half hours in order to allow the experiment to reach equilibrium. Each experiment was repeated three times.

SAMPLING METHODOLOGY

At the end of the studies, 10 cm^3 of sample was taken from each vial using a syringe with a 0.45 µm filter and placed in a labelled, sealed glass sample vial for storage until analysis. The adsorption isotherms were then prepared and compared against Langmuir (**Equation 3.6**) and Freundlich (**Equation 3.10**) adsorption models in order to determine the theoretical maximum adsorption capacity (**Equation 3.8**) and the energy of adsorption (**Equation 3.13**).

Kinetic Study Approach: Thermally activated hydrotalcites

Adsorption studies were carried out by placing the appropriate amount of adsorbent (5.1570 g thermally activated hydrotalcite) into 500 cm^3 of oxalate test solution whilst being stirred. Samples were then taken at 10 minute intervals until an elapsed time of three hours. The carbon concentration (and therefore the amount of oxalate adsorbed) was then determined through the use of total carbon analysis and inorganic carbon analysis. Each Experiment was repeated 3 times.

SAMPLING METHODOLOGY

Samples were taken for analysis by using a syringe to extract 10 cm^3 of solution from the slurry. After the sample had been taken, it was placed into a glass centrifuge tube and centrifuged at 4000 rpm for 1 minute to separate any particulate materials from the supernatant liquor.

The sample was then poured off from the particulate dregs and placed into a labelled sample tube and stored until analysis, where the data was tested against the first order kinetics model (**Equation 3.15**), the second order kinetics model (**Equation 3.16**) and the intra-particle diffusion model (**Equation 3.17**).

4.4.7 SAMPLING METHODOLOGY

All glassware used in the sampling method was treated in an acid bath (10 % nitric acid) to remove any particulates and organic contaminants.

For TOC analysis, the samples were diluted by pipetting 1.25 cm^3 into a 25 cm^3 volumetric flask and diluting to the mark in order to achieve a 1:20 dilution. The samples were then placed into clean TOC sample tubes and immediately analysed for total carbon (TC) content and inorganic carbon (IC) content and compared against the calibration curves prepared using the standards prepared in **Table 4.1** above in order to determine the TC and IC content, and from there the TOC content, which was then related back to the oxalate concentration.

Chapter 5: Results and Discussion: Materials preparation and characterisation

5.1 CHARACTERISATION OF HYDROTALCITE

After preparation, the hydrotalcite samples were analysed using a number of methods in order to gain an understanding of the structure of the material. These methods included X-Ray diffraction (XRD), thermo-gravimetric analysis (TGA), infrared (IR) and Raman analysis, along with infrared emission spectroscopy (IES); scanning electron microscopy (SEM) and transmission electron microscopy (TEM).

Nitrogen adsorption isotherms were analysed with the BET equation to determine the surface area and the pore volume was calculated using the BJH method. X-ray diffraction patterns, infrared, Raman and infrared emission spectra, along with thermogravimetric analysis all show that the sample was a typical hydrotalcite-like material.

5.1.1 XRD ANALYSIS

No.	Pos. [°2θ]	d-spacing [Å]	Rel. Int. [%]	Matched by
1	11.35	7.79	100	01-089-0460
2	22.40	3.96	24.58	01-089-0460
3	34.34	2.61	13.42	01-089-0460
4	38.49	2.33	6.01	01-089-0460
5	60.40	1.53	10.18	01-089-0460
6	61.72	1.50	8.86	01-089-0460
7	65.41	1.42	1.33	01-089-0460

Table 5.1: Powder XRD peak list of hydrotalcite

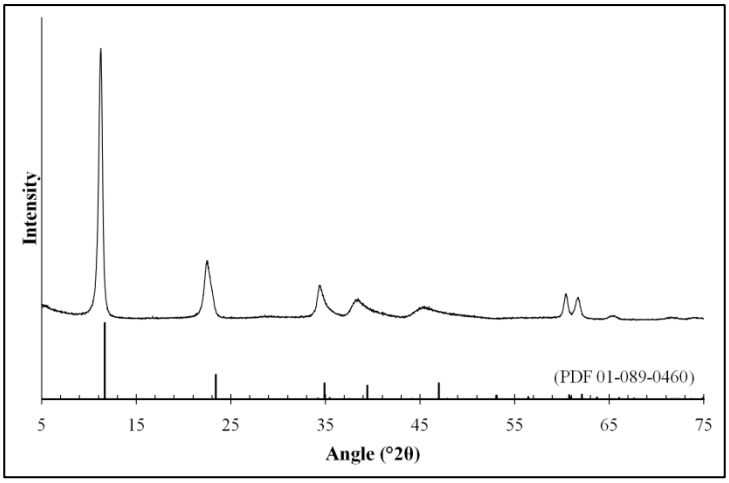

Figure 5.1 XRD pattern of hydrotalcite sample with PDF hydrotalcite standard 01-089-0460

From the XRD data, it can be seen that the material analysed matches well with synthetic hydrotalcite (PDF 01-089-0460 see **Table 5.1**), with most peaks being detected in the pattern (**Figure 5.1**). The peaks that are absent in the samples diffraction pattern are a consequence of the hydrotalcite crystals having a preferred orientation which results in an increased signal for some reflections which are specific to certain orientations. This results in an over-representation of these preferred directions which flood out other reflections present in the diffraction pattern of the sample.

A Rietveld refinement was done on the sample in order to determine the lattice parameters using the $R\bar{3}m$ space group and starting cellages of 3.054 Å for *a* and *b* and 22.81 Å for the *c* parameter. With the Rietveld refinement it was determined that the *a* and *b* parameters of the material were as expected for carbonate intercalated hydrotalcite, while the *c* axis parameter was determined to be 23.55 Å which is larger than is expected for a carbonate hydrotalcite. This enlarged spacing can be rationalised in terms of the water content which is supported from the examination of the IR and Raman spectra and TGA data.

5.1.2 IR ANALYSIS

The band component analysis of the recorded spectrum (see **Table 5.2**, below) shows quite good agreement with literature reports of Infrared spectra of hydrotalcite samples. This includes clearly identifying the metal-oxide and metal-hydroxide vibrations through comparison with studies involving deuteration and intercalation of various anions into synthetic hydrotalcites [98-100]. There is close correlation between the sample and reported peaks of Costa *et al.* [99] over in the 1350-1380 cm^{-1} range which may be ascribed to the ν_3 carbonate antisymmetric stretch which indicates the hydrotalcite has carbonate between the layers.

Sample Peak	Reported Peak [98]	Assignment
594		M-O Bonding
634	635	M-O Stretching mode [98]
733	759	M-OH Translation mode [98]
877	870	M-OH Deformation and υ_2 CO_3^{2-} [98]
1369	1365	υ_3 CO_3^{2-} [98]
1401	1401	υ_{3a} CO_3^{2-} [98]
1629	1642	H_2O OH Bending mode [98]
3074	3063	CO_3^{2-} -H_2O Bridging mode [98]
3336	3318	$MgAl_2$-OH Stretch [98]
3477	3467	Mg_2Al-OH Stretch [98]
3606	3597	Mg_3-OH Stretch [98]

Table 5.2: Infrared peaks for hydrotalcite

The table of peaks (**Table 5.2** above) and the IR spectrum (**Figure 5.2**) demonstrate a typical hydrotalcite Infrared spectrum seen in this study.

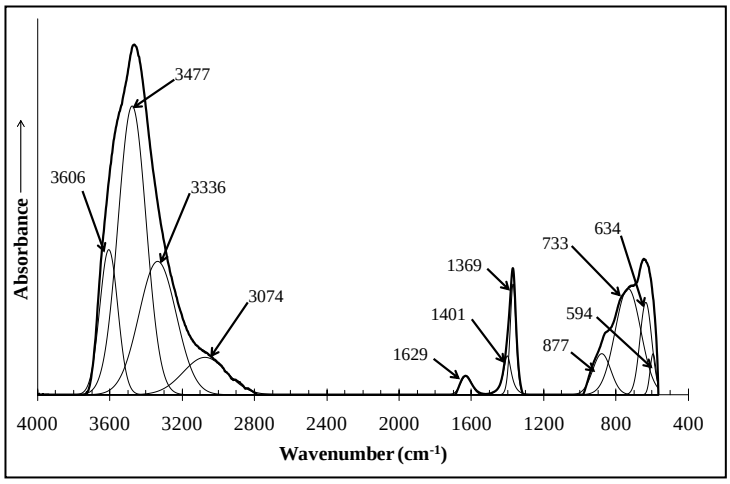

Figure 5.2: ATR-IR spectrum of hydrotalcite with band component analysis

5.1.3 RAMAN ANALYSIS

The spectrum for hydrotalcite can be seen in **Figure 5.3** below and the peaks have been recorded in **Table 5.3** below. It can be seen that there is close agreement between the peaks in the Raman spectrum and the peaks that have been reported in the literature for a carbonate intercalated hydrotalcite [98, 101, 102].

Raman Shift (cm^{-1})	Reported Position (cm^{-1})	Assignment
200		Hydrogen bonding
345		M-O Bonding
377		M-O Bonding
470	470	Al-O-Al- and Mg-O-Mg linkage [103]
549	551	Mg-OH [98, 103]
808		CO_3^{2-}
999	980	Al-OH deformation [103]
1060	1068	υ_1 CO_3^{2-} [98, 103]
3239	3250	Interlayer H_2O [103, 104]
3389	3354	$MgAl_2$-OH
3498	3485	Al_3-OH
3609	3615	Al-OH stretch [104]
3660	3673	Mg-OH stretch [104]

Table 5.3: Raman shifts of hydrotalcite

There is some peak shifting to higher wavenumbers for the metal hydroxide stretching vibrations which occur at 3660 cm^{-1} and 3609 cm^{-1} as reported in the literature [98, 103, 104]. Furthermore, there is also a upward shift for the interlayer water/water-carbonate bridging mode at 3239 cm^{-1}. This is suggestive of some restriction of freedom for these atoms due to hydrogen bonding (which is seen around 200 cm^{-1}). The metal-oxygen linkages at 470 cm^{-1} and the magnesium hydroxide deformation at 549 cm^{-1} are at the same wavenumber as has been reported in the literature. This is suggestive of the metal-oxygen and metal hydroxide bonds forming in a similar manner as those in the other reported hydrotalcites [98, 103, 104].

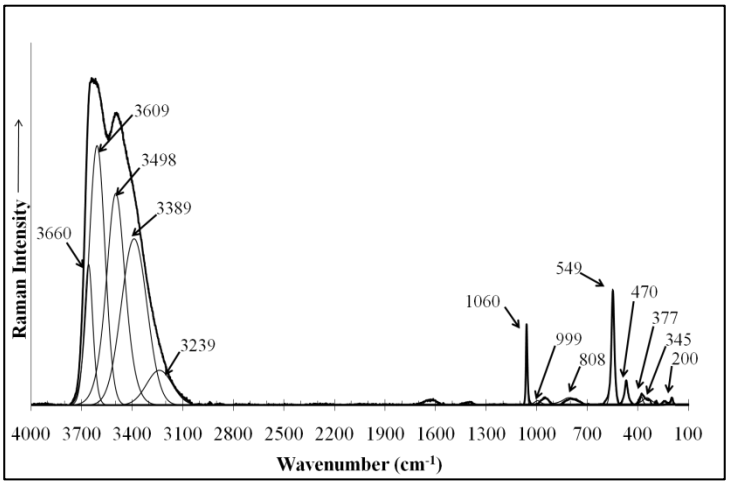

Figure 5.3: Raman spectrum of hydrotalcite

There are also a number of very weak bands in the fingerprint region at 200 cm^{-1}, 345 cm^{-1}, 377 cm^{-1} 808 cm^{-1} and 999 cm^{-1} which have not previously been reported in the literature. These peaks are most likely background peaks.

However, the Raman spectrum corresponds to those previously reported in the literature and it can be confirmed through XRD, IR and Raman spectroscopy that the sample is hydrotalcite.

5.1.4 IES ANALYSIS

Infrared emission spectra are recorded in **Figure 5.4** below and a band fitting analysis for the spectra at each temperature was completed, with the results recorded in **Figure 5.4** below.

	Temperature (°C)										
Wavenumber (cm^{-1})	**100**	**150**	**200**	**250**	**300**	**350**	**400**	**450**	**500**	**550**	**600**
	781 (129)	789 (131)	782 (121)	772 (176)	711 (306)	722 (254)	751 (227)	715 (156)	717 (142)	--	--
	--	--	--	--	--	--	--	--	--	--	809 (180)
	882 (113)	886 (115)	881 (111)	878 (198)	851 (199)	856 (169)	854 (144)	845 (165)	838 (157)	849 (205)	--
	--	--	--	--	--	--	--	--	--	--	871 (140)
	990 (153)	995 (180)	987 (182)	1037 (146)	1021 (161)	1001 (176)	966 (201)	980 (179)	957 (196)	--	967 (146)
	--	--	--	--	--	--	--	--	--	--	1063 (40)
	--	--	--	--	--	--	--	--	--	--	1173 (393)
	1363 (129)	1360 (125)	1365 (137)	--	--	--	--	1378 (106)	1367 (93)	1363 (86)	1364 (96)
	--	--	--	1408 (163)	1419 (139)	1415 (134)	1409 (130)	--	--	--	--
	1527 (161)	1532 (145)	1539 (146)	1557 (131)	1552 (138)	1547 (141)	1530 (142)	1495 (162)	1484 (160)	1478 (148)	1479 (158)
	--	--	--	--	--	--	--	--	--	--	1579 (67)
	1951 (63)	1958 (73)	1957 (80)	1959 (83)	--	--	--	--	--	--	--
	3049 (435)	3153 (503)	3154 (470)	3074 (388)	--	--	--	--	--	--	--
	3365 (298)	3381 (242)	3384 (266)	3381 (336)	3215 (445)	3217 (448)	3401 (283)	3450 (196)	3451 (195)	3421 (174)	3444 (222)
	3523 (188)	3513 (170)	3527 (192)	3554 (191)	3444 (284)	3443 (276)	3540 (180)	3567 (145)	3572 (152)	3563 (165)	3568 (157)
	3633 (112)	3632 (134)	3639 (127)	3648 (111)	3589 (167)	3583 (163)	3629 (113)	3644 (101)	3647 (96)	3652 (101)	3655 (95)
	3705 (52)	3707 (51)	3705 (54)	3705 (53)	3676 (94)	3670 (94)	3688 (54)	3690 (42)	3688 (41)	3691 (45)	3691 (45)

Table 5.4: IES peaks of hydrotalcite (with peak widths (FWHM) in brackets)

The hydroxyl stretching region (3000–4000 cm^{-1}) shows a number of interesting changes occur as the sample is heated. The first of these changes is the disappearance of the H_2O-CO_3^{2-} bridging mode around 3050-3070 cm^{-1} after 250 °C.

Furthermore, there is a decrease in intensity of the metal hydroxide bands from 300 °C onwards, which suggests that dehydroxylation occurs from around 300 °C, with it being almost complete by 550-600 °C; which correlates to the TGA data (S**ection 5.1.5**). The Mg-Al_2-OH band at 3366 cm^{-1} moves to around 3450 cm^{-1} before disappearing in the spectra taken at 600 °C, while the Mg_2-Al-OH and the Mg_3-OH stretches at 3523 cm^{-1} and 3633 cm^{-1} are still present (albeit very weak) at 600 °C, which is indicative of destruction of the hydrotalcite structure by that temperature and the formation of degradation products.

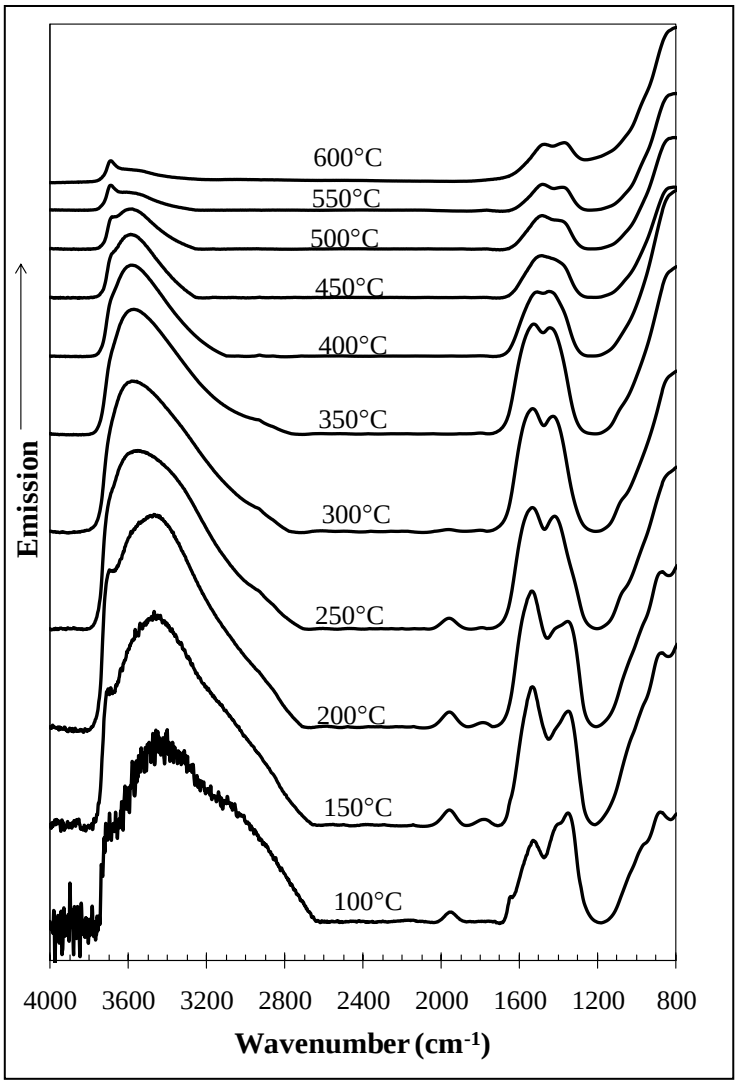

Figure 5.4: Infrared emission spectra (IES) of hydrotalcite

Discussions of the thermal decomposition of hydrotalcites in the literature [105-109] have suggested that the dehydroxylation of the materials involve a collapse of the basal spacing as carbonate becomes incorporated into the brucite-like layer and that the dehydroxylation involves the migration of protons from the internal structure through the brucite-like layer to the outer layer; which manifests as this band around 3707 cm^{-1}.

The carbonate bands are initially three distinct bands around 1300-1550 cm^{-1}, with peaks at 1343 cm^{-1}, 1415 cm^{-1} and 1527 cm^{-1}. A band at 1644 cm^{-1} is assigned to the bending vibration of water. There is suggestion that the carbonate in the sample migrates into the brucite-like layer at temperatures over 250 °C [105, 107] which is shown by the activation of the previously inactive ν_1 band at 1037 cm^{-1} and a band around 1557 cm^{-1}. This is caused by simultaneous dehydration and decarbonisation of the hydrotalcite and the need for carbonate to balance the charge loss during dehydration. It can be a little more difficult to identify this ν_3 carbonate band due to a possible overtone of the M-OH band around 780 cm^{-1} centred around 1560 cm^{-1} resulting in a constructive interference centered around 1550 cm^{-1}.

The presence of the carbonate band at all temperatures, albeit at weakening intensity, is suggestive of the decarbonisation of the material is a function of time, rather than temperature, which is indicated in the TGA data (**Section 5.1.5**) which shows that decarbonisation peaks around 280-300 °C, decarbonisation then occurs at a much reduced rate until around 600 °C [109].

The fingerprint region shows some interesting features, in that the spectra can only be taken to 650 cm^{-1} due to limitations in the instrumentation and therefore only three relevant bands can be made out. There are bands at 781 cm^{-1}, 882 cm^{-1} and 990 cm^{-1}. These are most likely the M-OH translation, the ν_2 carbonate band and also the M-OH deformation mode.

The M-OH translation at 781 cm^{-1} and the M-OH Deformation mode at 990 cm^{-1} both decrease in intensity after 400°C, which is indicative of decomposition of the sample. Given that these reactions are at higher temperatures than the other hydroxyl (3000 cm^{-1} to 4000 cm^{-1}) and carbonate bands (1343 cm^{-1} and 1415 cm^{-1}), it is likely that these bands are related to hydroxyls and carbonates being hydrogen bonded.

5.1.5 TGA ANALYSIS

According to the mass losses recorded in the TGA plot in **Figure 5.5**, it is clear that there are four major mass losses occurring in the sample. The percentage mass loss and the calculated decomposition steps are shown in **Table 5.5**.

From the TGA data, the decomposition steps are the loss of surface adsorbed and some interlayer water up to 155 °C. This is in contrast with Kloprogge and Frost [110] and Palmer *et al.* [24], who suggested that water was eliminated by 70 °C.

Temperature (°C)	% Mass Loss	Actual Mass loss (AMU)	Theoretical Mass loss (AMU)	Proposed Formula
25	0	0	0	$Mg_6Al_2(OH)_{16}(CO_3).5H_2O$
155	12.22	75.5	72	$Mg_6Al_2(OH)_{16}(CO_3).H_2O$
280	7.78	48.1	54	$Mg_6Al_2O_2(OH)_{12}(CO_3)$
303	12.22	75.5	78	$Mg_6Al_2O_3(OH)_{10}$
1000	12.22	75	74	$5MgO + MgAl_2O_4$

Table 5.5: Mass loss steps for hydrotalcite

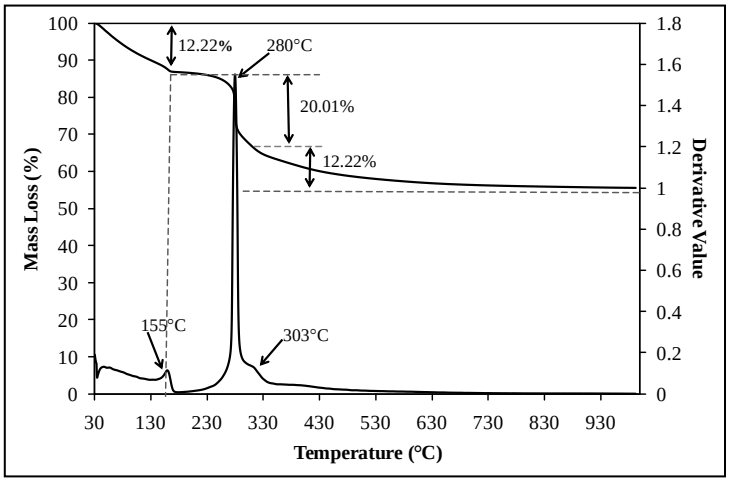

Figure 5.5: TGA analysis of hydrotalcite

The next decomposition step occurs at 280 °C, in which a number of processes are occurring. The first of these is the loss of the last interlayer water through the migration of the brucite-like layer. This is then followed by a change in the structure of the material by a partial dehydroxylation of the brucite layer and the partial incorporation of the carbonate group into the structure [105-107]. This in contrast with by Kloprogge and Frost [110], who claim that decarbonisation occurs between 70 and 230 °C while Hutson [111] suggests that although decarbonisation begins at approximately 100 °C, it does not become a significant process until approximately 200 °C, which is a view shared by Sharma *et al.* [112].

The third decomposition step around 303 °C is the completion of the dehydroxylation followed by completion of decarbonisation, which finishes around 600 °C [109].

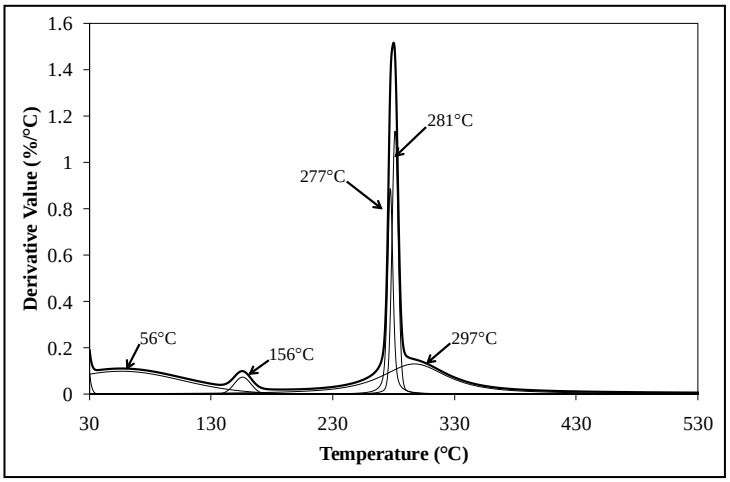

Figure 5.6: Band component analysis of major mass loss peak for hydrotalcite

The dehydroxylation peak centered around 280°C was analysed using band component analysis and showed that there are three simultaneous processes occurring. The first two processes are the simultaneous dehydroxylation of the cation layers [113], while a peak centred around 297 °C is most likely due to decarbonisation of the sample along with the final dehydroxylation of the products to form a mixed metal solid solution, followed by the formation of spinel and periclase at almost 1000 °C. Once again, these conclusions are supported by the IES analysis, which shows that dehydroxylation is almost complete at 600 °C.

5.1.6 NITROGEN ADSORPTION/DESORPTION ANALYSIS

The summary of BET data (see **Table 5.6** below) shows that the material has a moderate surface area.

Property	Hydrotalcite Sample
BET Surface Area (m^2/g)	34.6 ± 0.1
Single Point Surface Area (m^2/g)	33.9
Langmuir Surface Area (m^2/g)	48 ± 1
Total Pore Volume (cm^3/g)	0.2
Average Pore Diameter (nm)	22.1

Table 5.6: BET analysis of hydrotalcite

When compared to values reported in the literature [91, 114-119], which range from 5-100 m^2/g, the hydrotalcite material prepared could be considered to not have a very large surface area, which is most likely due to the preparation technique. The large variation seen in the materials reported in the literature are most likely due to a number of different preparation techniques being used and a range of crystallite sizes being obtained.

5.1.7 SEM/TEM ANALYSIS

Hydrotalcite is regularly reported in the literature to be a substituted form of Brucite [$Mg(OH_2)$] with a similar hexagonal crystal shape [3, 43, 48-50, 54, 58, 66]. It can be seen from the SEM and TEM pictures [see **Figure 5.7**; **Figure 5.8**; **Figure 5.9** and **Figure 5.10** below] that the hydrotalcite crystals are hexagonal in shape, which correlates to what is reported by Bontchev *et al.* [60] who report hydrotalcite to have a hexagonal/rhombohedral crystal shape.

The SEM images (**Figure 5.7** and **Figure 5.8** below) show definite hexagonal platelets that appear to stack together rather well. However, there is also a number of clumps (see **Figure 5.7**) in which platelets have a random arrangement of crystals; particularly around the edges of the clumps (see **Figure 5.8**).

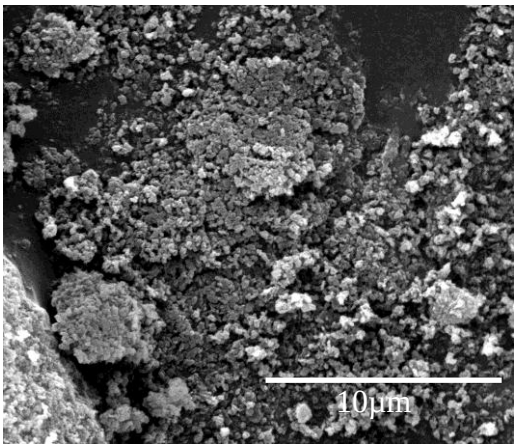

Figure 5.7: SEM image of hydrotalcite at a magnification of 12 kx

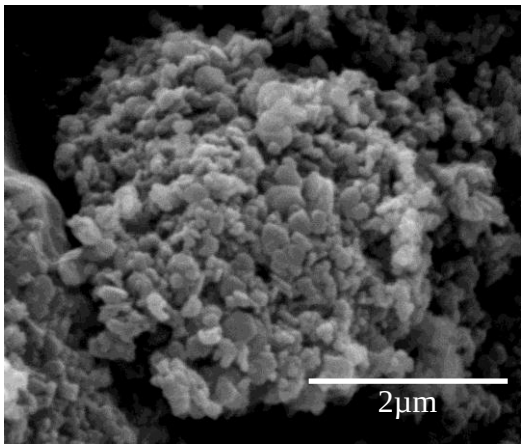

Figure 5.8: SEM image of hydrotalcite at a magnification of 50 kx

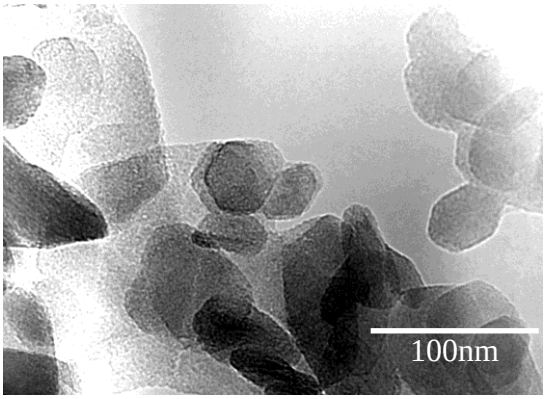

Figure 5.9: TEM image of hydrotalcite at a magnification of 400 kx

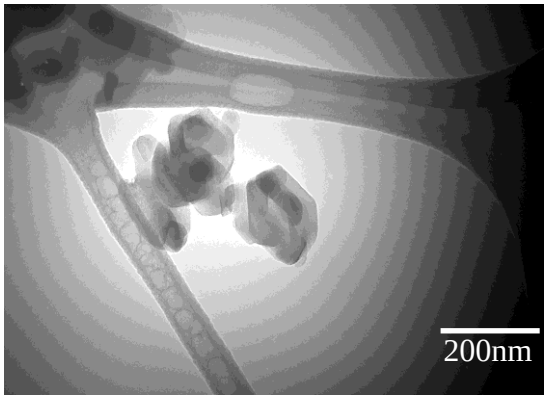

Figure 5.10: TEM of hydrotalcite at a magnification of 120 kx

It can be seen in the TEM image in **Figure 5.9** that the crystals are well defined with evidence of Dalton ageing in the middle-right of the image (shown by two crystals growing into each other). The TEM image in **Figure 5.10** shows that the average hydrotalcite crystal size is less than 200 nm.

5.1.8 THERMAL DECOMPOSITION STUDY

In order to determine the best time to thermally treat the hydrotalcite, a sample was placed in the TGA and heated with the same thermal treatment regime as would be used for the thermally activated hydrotalcites (see **section 4.1.2**) and the mass loss recorded (see **Figure 5.11**).

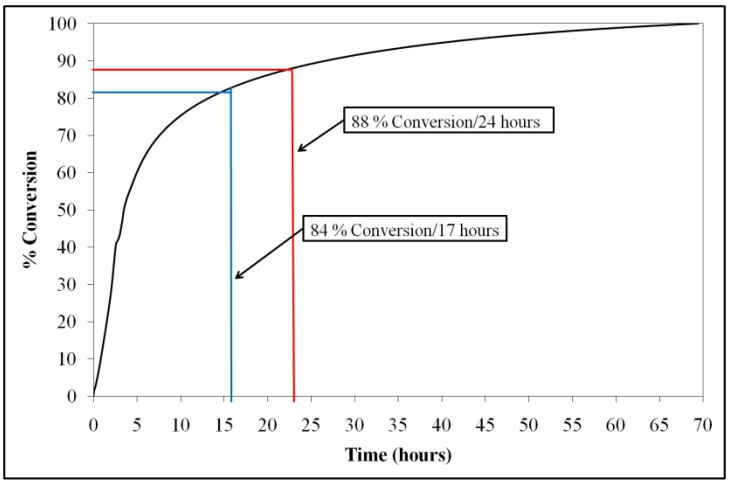

Figure 5.11: Plot of % conversion vs. time for hydrotalcite heated to 280 °C

As can be seen in **Figure 5.11**, the decomposition of hydrotalcite under a 280 °C thermal treatment regime appears to be exponential. For this reason, a plot of time on mass at time against time (t/mt vs. t, **Figure 5.12**) is strongly indicative of 2nd order kinetics decomposition, with an R^2 value of 0.9983.

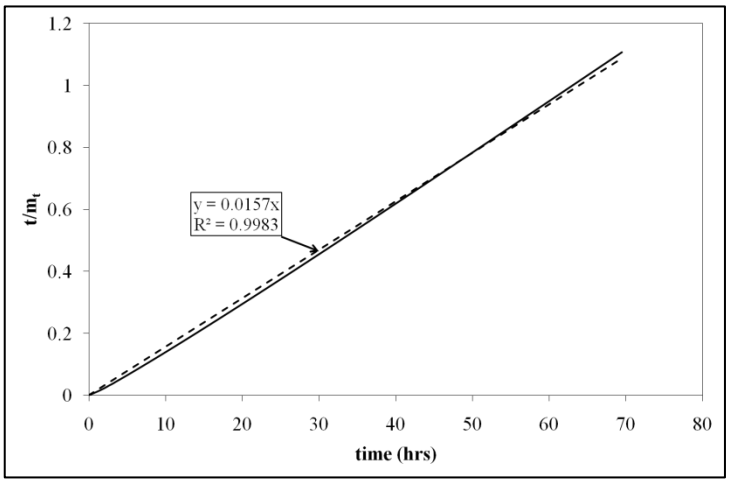

Figure 5.12: Plot of t/mt vs. t for hydrotalcite thermally treated to 280 °C

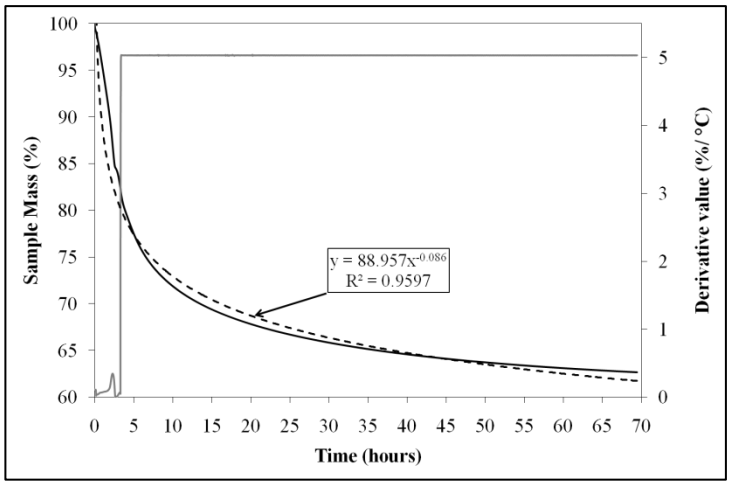

Figure 5.13: TGA plot of mass loss at 280 °C vs. time for hydrotalcite

The mass–time plot in **Figure 5.11** shows that the thermal treatment regime of heating at 5 °C per minute to 280 °C gives dehydration of surface water for the first three hours before decomposition begins after 3.5 hours as shown in the TGA plot derivative (**Figure 5.13**).

From the mass loss vs time plot (**Figure 5.11**), a treatment time of 17 hours suggests that approximately 84 % of the hydrotalcite decomposes given experimental conditions including sample size, heat transfer and the assumption that 70 hours of treatment time is maximum conversion.

Thermal treatment times of 17 and 70 hours were chosen as the sample preparation times as 17 hours (see **Section 5.2**) would correlate to the sample being prepared and heated during the morning and treated during the afternoon and overnight; while 70 hours of treatment time (See **Section 5.3**) correlated with 3 days worth of thermal treatment, allowing for sample preparation and cooling. Of which, both timeframes would be convenient.

Based on the decomposition plot (**Figure 5.11**), it was determined that a 24 hour treatment time gave approximately 90 % decomposition of the sample (according to the plot, it gives 88 % decomposition) which is between complete decomposition and minimum treatment time

5.2 CHARACTERISATION OF THERMALLY ACTIVATED HYDROTALCITE (TAHT 17)

In order to prevent the thermally activated hydrotalcite reforming during analysis, only small amounts of material were taken from the sample for each analysis undertaken and kept under nitrogen until the analysis was completed. The material was characterised using powder XRD, infrared and Raman spectroscopy, SEM and TEM imaging as well as BET analysis in order to get an understanding of how the structure of the material and its surface was changed by calcination.

Analysis of the X-ray diffraction pattern, coupled with infrared and Raman spectral analysis indicates that there has been some change to the structure of the material. There is also evidence of an increase in the BET surface area.

5.2.1 XRD ANALYSIS

The X-ray diffraction pattern was collected using the special stage shown in Figure 4.1 and the peak list is shown in Table 5.7 below with the XRD pattern seen in **Figure 5.14**.

No.	Pos. [°2θ]	d-spacing [Å]	Rel. Int. [%]	Matched by
1	11.70	7.56	100	01-089-0460
2	23.57	3.77	8.29	01-089-0460
3	34.41	2.60	4.46	01-089-0460
4	38.57	2.33	8.69	01-089-0460
5	60.34	1.53	12.73	01-089-0460
6	61.78	1.50	5.08	01-089-0460
7	65.75	1.42	0.95	01-089-0460

Table 5.7: Powder XRD peak list of thermally activated hydrotalcite (TA17)

Although there are similarities with the calculated hydrotalcite XRD pattern (PDF 01-089-0460) there are some differences, including the presence of a region around 33 to 44 °2θ which appears as being quite broad (albeit slightly shifted) which indicates a presence of magnesium oxide in the form of a solid solution/periclase with a small crystallite size [108].

When this region is considered with the position of the peaks when compared to the hydrotalcite sample from which this material was prepared, there is evidence suggestive of some contraction of the interlayer spaces.

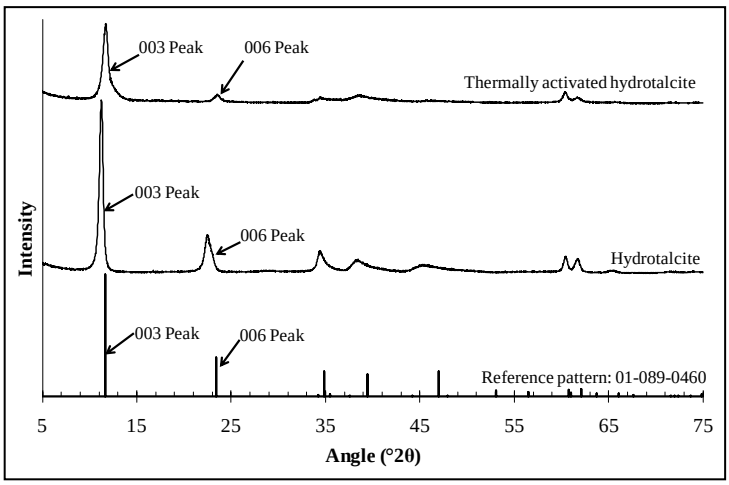

Figure 5.14: XRD comparison of hydrotalcite and thermally activated hydrotalcite (TA17)

A direct comparison between the X-ray diffraction patterns of both materials (see **Figure 5.14**) clearly indicates the differences in the two materials. In particular, as noted earlier, the differences between the relative intensities between the calcined and starting materials, as well as the broad reflections in the region between 33 and 44 °2θ, which are suggestive of the formation of periclase. There is also clear evidence of asymmetry in the 003 peak, which is biased to higher angles, which is what would be expected if the interlayer spaces had started to collapse.

The Rietveld refinement shows that there has been decomposition of hydrotalcite to periclase, with the composition of the sample (as per the Rietveld refinement) being 32.6 % periclase and 67.4 % hydrotalcite.

The Periclase cell parameters are 4.32 ± 0.01 Å for the *a*, *b* and *c* axes, which are larger than the 4.19Å cell parameters given by the reference standard (PDF 01-075-1525). For the hydrotalcite, the *a* and *b* cell parameters were determined to be 3.04 ± 0.04Å while the *c* axis parameter was 22.5 ± 0.2Å. The shortened hydrotalcite *c* axis parameter is suggestive of layer collapse.

5.2.2 IR ANALYSIS

The recorded spectrum (see **Table 5.8**) shows some correlation between the expected infrared peaks for hydrotalcite (see above) although there have been some changes to the infrared spectrum, which can be seen in **Figure 5.15** and **Figure 5.16**.

Sample Peak (cm^{-1})	Reported Peak (cm^{-1})[98]	Assignment
580		M-O Bonding
601		M-O Bonding
635	635	M-O Stretching mode [98]
725	759	M-OH Translation mode [98]
869	870	M-OH Deformation and υ_2 CO_3^{2-} [98]
1023		CO_3^{2-} [104]
1354	1365	υ_3 CO_3^{2-} [98]
1418	1401	υ_{3a} CO_3^{2-} [98]
1527		H_2O OH bending mode [98]
1577		H_2O OH bending mode [98]
3374	3318	$MgAl_2$-OH Stretch [98]
3509	3467	Mg_2Al-OH Stretch [98]
3617	3597	Mg_3-OH Stretch [98]
3707		Mg-OH Stretch [104]

Table 5.8: Infrared peaks of thermally activated hydrotalcite (TA17)

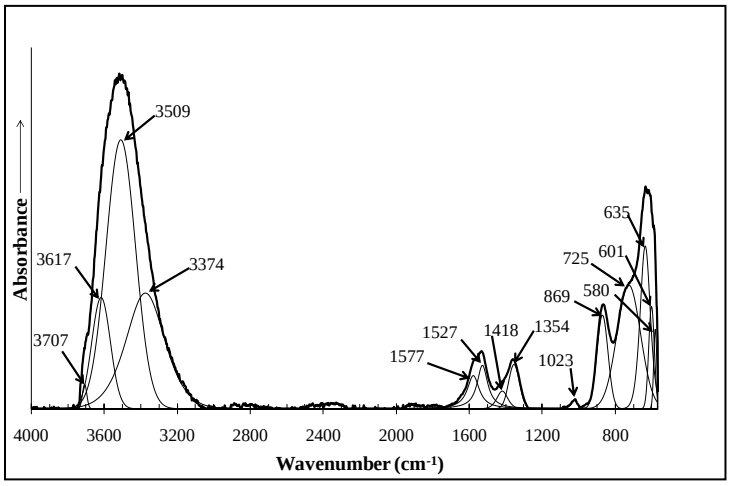

Figure 5.15: Infrared spectrum of thermally activated hydrotalcite (TA17) with band component analysis

From the band component analysis, there have been a number of changes to the material upon heating. The first of these changes is the appearances of a number of new bands centred at 580 cm^{-1}, 601 cm^{-1}, 1023 cm^{-1}, 1527 cm^{-1} and 3707 cm^{-1}.

Along with these new bands, there have also been a number of bands that have disappeared with heating, in particular the water bands at 1642 cm^{-1} and 3074 cm^{-1}. The metal hydroxide bands at 3374 cm^{-1}, 3509 cm^{-1} and 3617 cm^{-1} have shifted to higher wavenumbers due to a reduction in hydrogen bonding and the metal hydroxide deformation mode around 735 cm^{-1} has shifted to a lower wavenumber.

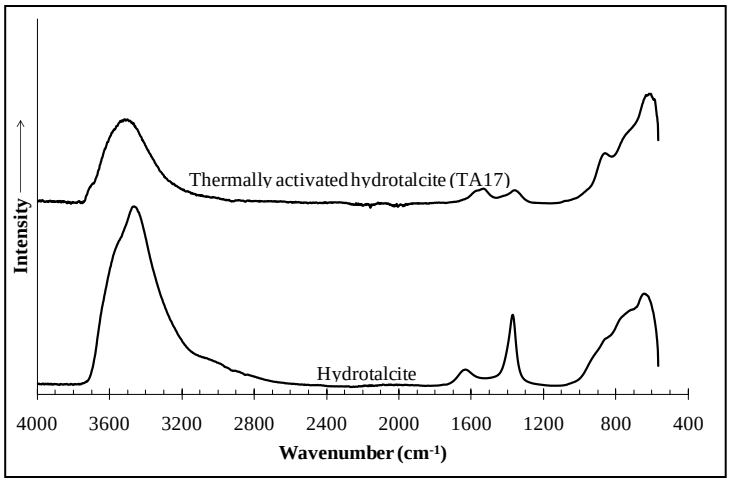

Figure 5.16: Comparison of hydrotalcite and thermally activated hydrotalcite infrared spectra (TA17)

The bands at 1642 cm^{-1} and 3074 cm^{-1} have been identified as water absorbed into the interlayer of the material and acting as a bridge between the carbonate anions and the metal hydroxide sheets [98, 100]. After thermal treatment, these bands are no longer present in the IR spectrum, which is indicative of the hydrotalcite dehydrating during heating.

The region around the carbonate ν_3 anti-symmetric stretching vibration (1200 cm^{-1} to 1800 cm^{-1}) is of interest due not only to the loss of the water band at 1642 cm^{-1}, but also due to the movement of the υ_3 carbonate bands at 1634 cm^{-1} and 1401 cm^{-1} and the appearance of new bands at 1527 cm^{-1} and 1577 cm^{-1}. These changes in this region of the IR spectrum indicate that the carbonate anions in the sample have undergone a change in symmetry (from C2v to B2h) from acting as an interlayer anions to being incorporated into the metal ion layer on heating due to the removal of water from the hydrotalcite [105, 107, 108].

There have also been several changes to the bands around the hydroxyl stretching region of the spectrum. The first difference to be noted is that the peak positions have all changed, with the bands at 3374 cm^{-1} and 3509 cm^{-1} having moved to higher wavenumbers by around 30 cm^{-1}. Furthermore, the Mg_3-OH stretch at 3617 cm^{-1} has moved by around 9 cm^{-1}. These shifts are most likely caused by the thermal treatment conditions.

A new, weak peak at 3707 cm^{-1} has appeared. The appearance of this band has been linked to the migration of protons through the metal cation layer and is related to the dehydroxylation process [105, 107, 108].

In the fingerprint region of the spectrum (the area below 1000 cm^{-1}) there have been a number of minor changes that have occurred to the spectrum. The first is the appearance of peaks at 580 cm^{-1} and 601 cm^{-1}. The second is the movement of the M-OH translation from 759 cm^{-1} to 725 cm^{-1}. The third change to occur is the appearance of a peak around 1023 cm^{-1}.

On direct comparison of the two spectra next to each other (**Figure 5.16**) it is clear that the intensity of the infrared bands is greatly decreased and is suggestive of partial decarbonisation and dehydroxylation of the hydrotalcite. Furthermore, there is clear evidence that the carbonate in the interlayer has not only decreased, but has changed in symmetry due to the change in the peak shapes between 1300 cm^{-1} and 1700 cm^{-1}.

5.2.3 RAMAN ANALYSIS

The spectrum for the hydrotalcite can be seen in **Figure 5.17** below and the peaks have been recorded in **Table 5.9** below.

Raman Shift (cm^{-1})	**Reported Position (cm^{-1}) [98]**	**Assignment**
113		H-Bonding
148		M-O Bonding
171		H-Bonding
188		H_2O intermolecular stretch [120]
215		H-Bonded M-OH
287		H-Bonded M-OH
467	465-475	Al-O-Al- and Mg-O-Mg linkage [103]
548	551	Mg-OH [98, 103]
1061	1068	υ_1 CO_3^{2-} [98, 103]
1083		CO_3^{2-}
1100		CO_3^{2-}
1231		CO_3^{2-}
1600		H_2O υ_2 bend[121]
3397	3354	$MgAl_2$-OH
3531	3485	Al_3-OH stretch
3619	3615	Al-OH stretch [104]
3669	3673	Mg-OH stretch [104]

Table 5.9: Raman shifts for thermally activated hydrotalcite (TA 17)

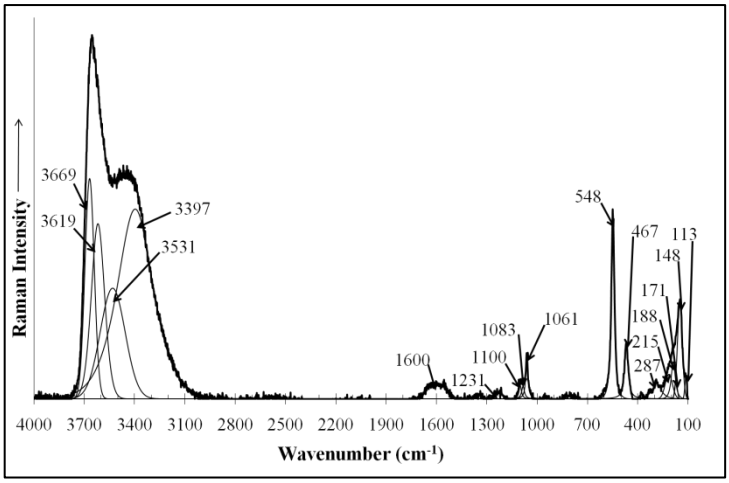

Figure 5.17: Raman spectra of thermally activated hydrotalcite (TA17)

As can be seen from the table of peaks (**Table 5.9**) and the spectra (**Figure 5.17**); there have been a number of changes to the spectrum when compared to that of the original hydrotalcite (**Figure 5.18**) including a decrease in the spectrum's intensity, as well as a broadening of the metal-hydroxide peaks and some changes to the fingerprint region of the spectrum.

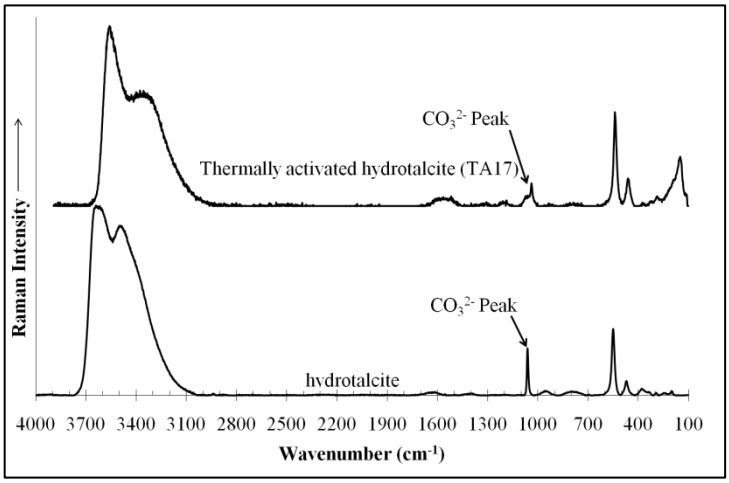

Figure 5.18: Comparison of hydrotalcite and thermally activated hydrotalcite (TA17) Raman spectra

The hydroxyl stretching region shows a number of differences to the precursor hydrotalcite. The first difference is that the peak at 3397 cm^{-1}, which is found at 3389 cm^{-1} in the precursor and is assigned as the $MgAl_2$-OH stretch has moved slightly higher and is comparatively more intense than in the precursor hydrotalcite. In addition, the peak at 3531 cm^{-1}, which is found at 3485 cm^{-1} in the precursor material has become less intense and has been assigned to Al_3-OH stretching. Furthermore, the peak at 3619 cm^{-1}, which is assigned as an Al-OH stretch usually found at 3615 cm^{-1} is also much less intense. The peak at 3669 cm^{-1} (Mg-OH stretch usually found at 3673 cm^{-1}) has become more intense. This is suggestive of dehydroxylation occurring around the aluminium atoms in the metal hydroxide sheets.

The bands around 1000 cm^{-1} and 1300 cm^{-1}, which is the location of the carbonate peaks in the spectrum are interesting in that the intense carbonate peak at 1068 cm^{-1} has been shifted to 1061 cm^{-1} and two more peaks have appeared at 1083 cm^{-1} and 1100 cm^{-1}, acting as a shoulder. The presence of these two peaks, coupled with a marked decrease in the intensity of the carbonate peak suggests that there has been decarbonisation during thermal treatment as well as a change in the symmetry of the carbonate between the layers.

The appearance of a low, broad peak at 1231 cm^{-1} is probably due to carbonate being absorbed into the metal ions layers of the material and reflects what has been seen the in the infrared spectrum. The presence of a peak at 1600 cm^{-1} is probably water adsorbed to the surface of the material and can be attributed to the water –OH bending modes [121]. The small peak at 188 cm^{-1} is probably the intermolecular water stretch (183 cm^{-1}) [120] and provides evidence that some free water has been adsorbed onto the surface of the material.

There are a number of peaks which occur in the fingerprint region which are not easily identified without band component analysis. These bands occur at shifts of 113 cm^{-1}, 148 cm^{-1}, 171 cm^{-1}, 215 cm^{-1} and 287 cm^{-1}. The band at 148 cm^{-1} is particularly intense, whilst the other bands are fairly weak. As these bands do not appear in the Raman spectrum of the precursor material, it is most likely that they are the product of the decarbonisation and dehydroxylation of the sample.

5.2.4 NITROGEN ADSORPTION/DESORPTION ANALYSIS

When the nitrogen adsorption data for the thermally activated hydrotalcite is compared with the precursor hydrotalcite nitrogen adsoprtion data, it is clear that thermal treatment has resulted in an increase of surface area and pore size. This can be equated to the decrease in size of the hydrotalcite crystals as well as loss of a clear hexagonal crystal structure casued by the thermal treatment process. **Table 5.10** compares the surface properties of the thermally activated hydrotalcite and the precursor hydrotalcite.

	Hydrotalcite	Thermally Activated Hydrotalcite
BET Surface Area (m^2/g)	34.6 ± 0.1	47.0 ± 0.1
Single Point Surface Area (m^2/g)	33.9	45.9
Langmuir Surface Area (m^2/g)	48 ± 1	64 ± 1
Total Pore Volume (cm^3/g)	0.2	0.4
Average Pore Diameter (nm)	22.1	37.6

Table 5.10: Comparison of nitrogen adsorption properties for hydrotalcite and thermally activated hydrotalcite (TA17)

As can be seen by the data, thermal treatment for 17 hours increases the active surface area by approximately 35 % while the total pore volume more than doubles and the average pore area almost doubles. This is suggestive that thermal activation at 280 °C for 17 hours has a definite positive impact on the surface properties of the material.

5.2.5 SEM/TEM ANALYSIS

The scanning electron micrographs show that the sample material is physically smaller than the precursor materials, SEM images of each are shown below (see **Figure 5.19**, **Figure 5.20** and **Figure 5.21**). There is also evidence that the crystal structure of the material has broken down somewhat, which is supported by the evidence of low broad peaks in the region between 33 °2θ and 45 °2θ in the XRD data (see **Figure 5.14** on page 67).

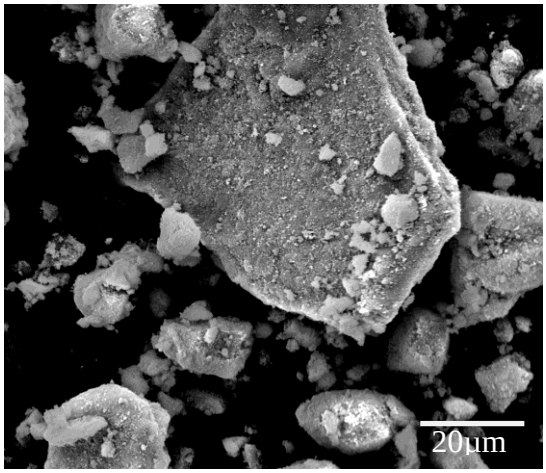

Figure 5.19: SEM image of thermally activated hydrotalcite (TA17) at a magnification of 2500 x.

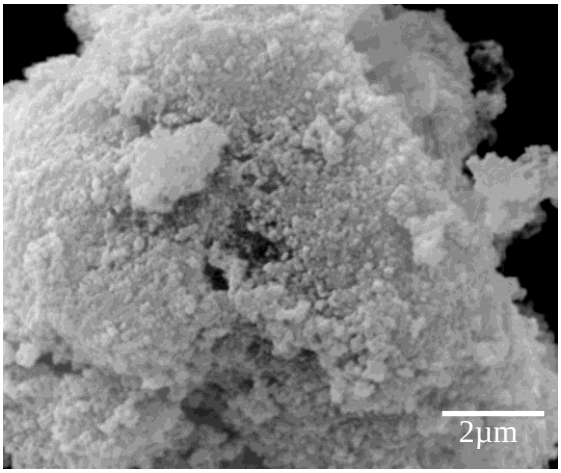

Figure 5.20: SEM image of thermally activated hydrotalcite (TA17) at magnification of 24 kx.

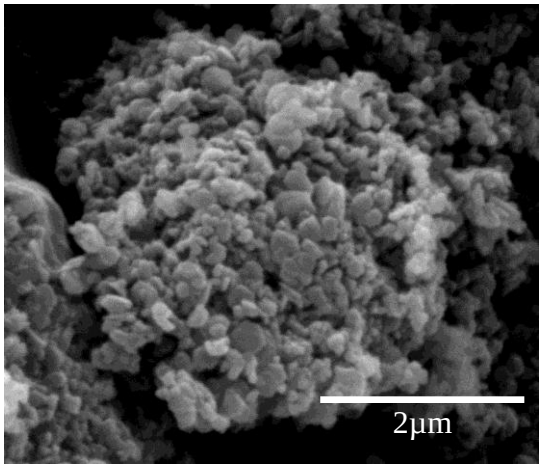

Figure 5.21: SEM image of hydrotalcite precursor material at a magnification of 50 kx.

It can be seen from the SEM Image in **Figure 5.19** that there is little evidence of a structure being present at low magnification and low resolution.

At a higher a magnification of 24000x (see **Figure 5.20**), it can be seen that the thermally activated hydrotalcite particles are very small (in the order of nanometres) and it is extremely difficult to determine if there is a crystal structure to the thermally activated hydrotalcite particles.

When the SEM images of the thermally activated hydrotalcite (**Figure 5.19** and **Figure 5.20**) are compared with the SEM image of the precursor hydrotalcite (see **Figure 5.21**) it is evident that there has definitely been a major decrease in the size of the hydrotalcite particles.

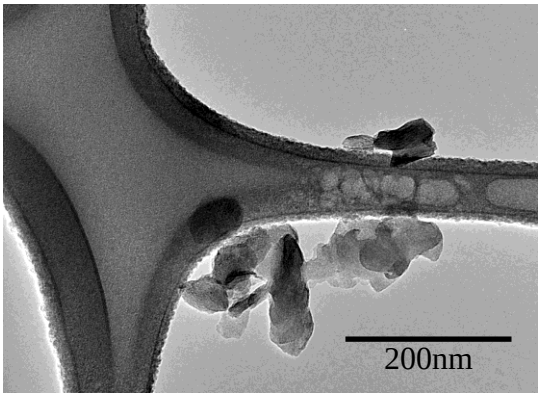

Figure 5.22: TEM image of thermally activated hydrotalcite (TA17) at a magnification of 200 kx

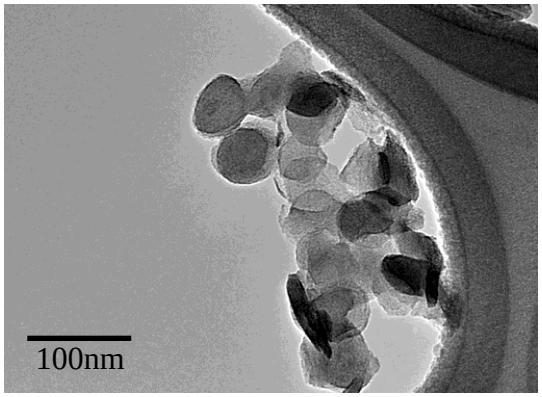

Figure 5.23: TEM image of thermally activated hydrotalcite (TA17) at a magnification of 250 kx

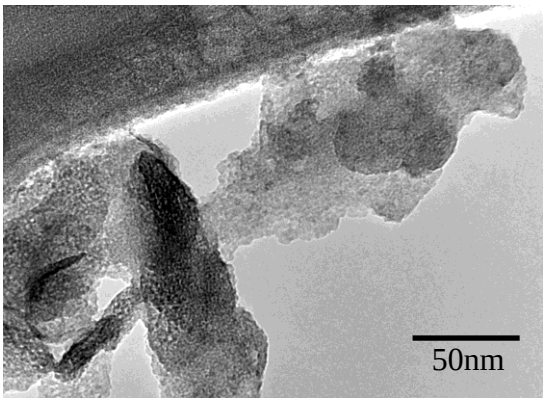

Figure 5.24: TEM image of thermally activated hydrotalcite (TA17) at a magnification 500 kx

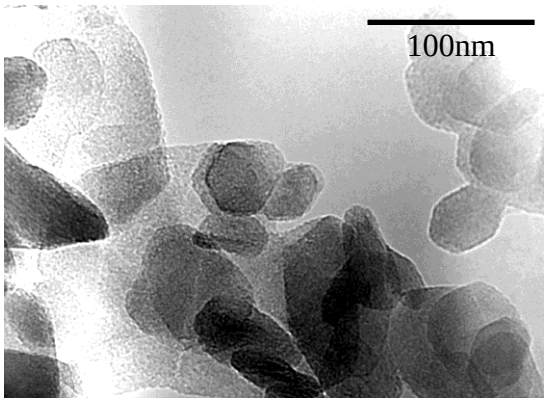

Figure 5.25: TEM image of precursor hydrotalcite at a magnification of 400 kx

It can be seen from the TEM images (see **Figure 5.22**, **Figure 5.23** and **Figure 5.24**) there have been considerable changes between the thermally activated hydrotalcite sample and the precursor materials (see **Figure 5.25** above) including some condensation of the crystals, which is consistent with what could be expected when the material has been dehydrated. The graininess of the crystals is also consistent with the growth of new crystals of mixed metal oxides from within the precursor crystals.

Furthermore, the crystals no longer have a clear hexagonal crystal shape as was seen in the TEM images of the precursor material (see **Figure 5.25**) with the appearance of fuzzy edges and an amorphous-looking region in **Figure 5.22** (which is shown in more detail in **Figure 5.24**) which is most likely small crystals of a solid solution of aluminium and magnesium oxides. This correlates with what was seen in the region between 33 and 50 º2θ in the powder XRD pattern (**Figure 5.14**).

5.3 CHARACTERISATION OF THERMALLY ACTIVATED HYDROTALCITE (TAHT 24)

5.3.1 XRD ANALYSIS

The X-ray Diffraction data for the thermally activated hydrotalcite (see **Table 5.11** and **Figure 5.26**) shows that there have been some significant changes from the precursor material. The first major change is the movement of the major reflection from around 11.2 °2θ to 13.3 °2θ which is a significant shift from the precursor hydrotalcite and may be due to almost complete elimination of carbonate from the sample resulting in collapse of the interlayer spaces. The presence of a very small peak at 11.15 °2θ is evidence that some hydrotalcite has not completely decomposed upon thermal treatment.

No.	Pos. [°2θ]	d-spacing [Å]	Rel. Int. [%]
1	11.15	7.90	7.83
2	13.32	6.68	100
3	26.30	3.42	2.33
4	33.94	2.60	1.2
6	36.57	2.44	15.82
7	43.45	2.08	7.19
8	60.27	1.53	19.18

Table 5.11: XRD peak list for thermally activated hydrotalcite (TAHT 24)

The region between 32 and 55 °2θ corresponds to the formation of periclase and brucite, which both have peaks in this region, along with other mixed metal oxides. The broad peaks in this region indicative of very small crystallites, which is similar to what was seen in the samples that had been thermally activated over 17 hours.

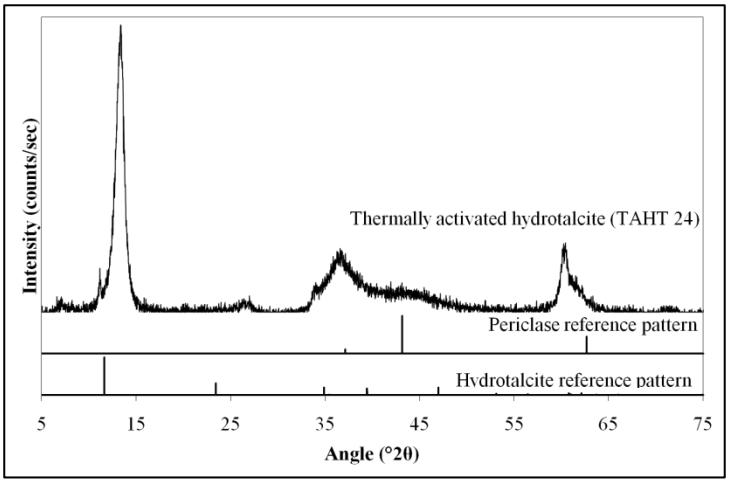

Figure 5.26: XRD pattern of thermally activated hydrotalcite (TAHT 24)

5.3.2 IR ANALYSIS

The infrared spectrum of the material (see **Figure 5.27**) and the corresponding peaklist (see **Table 5.12**) shows that there are some similarities and some differences between the thermally activated hydrotalcite and the precursor material.

Sample Peak (cm^{-1})	Reported Peak (cm^{-1})[98]	Assignment
762	759	M-OH Translation mode [98]
1031	870	M-OH Deformation
1352	1365	υ_3 CO_3^{2-} [98]
1526		CO_3^{2-}
2967		M-OH Stretching Vibration
3327		M-OH Stretching Vibration
3562		M-OH Stretching Vibration

Table 5.12: Infrared peak list of thermally activated hydrotalcite (TAHT 24)

The first of these differences is in the carbonate ν_3 anti-symmetric stretching vibrations, which shows two bands at 1351 and 1525 cm^{-1}, which are significantly different for the parent hydrotalcite. The appearance of the second carbonate band at 1525 cm^{-1} is clear evidence of a major change to the chemical structure of the material upon heating, which is the absorption of the carbonate into the metal ion layer.

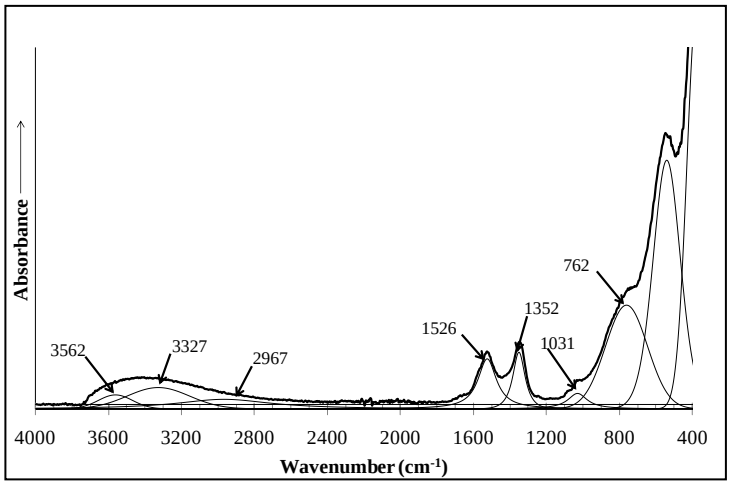

Figure 5.27: Infrared spectrum of thermally activated hydrotalcite (TAHT 24)

The second major change is in the hydroxyl stretching region, which shows significantly decreased intensity and peak broadening, which would be expected if the sample had partly rehydrated and started to reform.

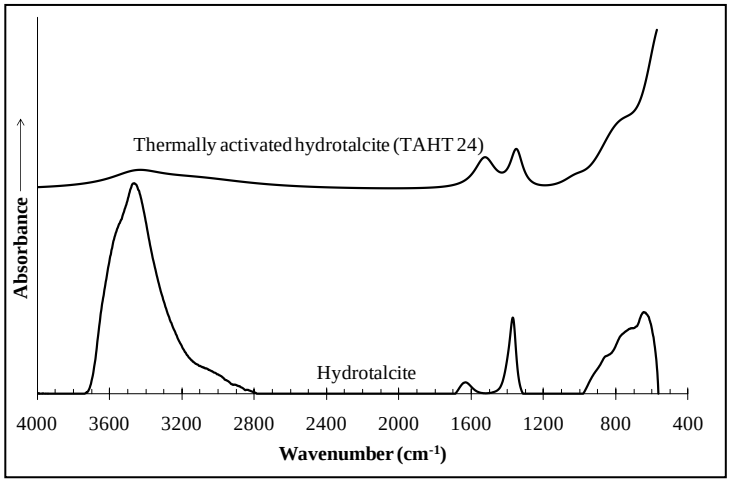

Figure 5.28: Comparison of IR spectra for thermally activated hydrotalcite (TAHT 24) and hydrotalcite

These differences from the spectra of the precursor hydrotalcite are most pronounced when the two spectra are compared against each other as in **Figure 5.28**. The differences in the carbonate and hydroxyl stretching regions are obvious in this figure and clearly indicate that the structure has changed. The differences in the spectra in the fingerprint region of the sample are most likely due to the use of a different instrument to collect the sample spectrum.

5.3.3 RAMAN ANALYSIS

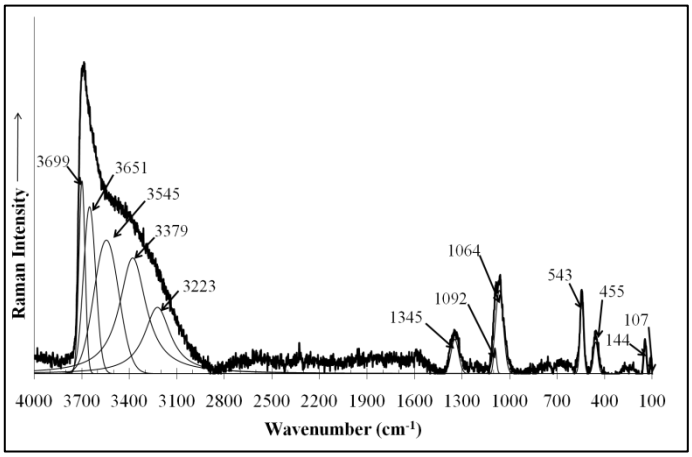

Figure 5.29: Raman spectrum of thermally activated hydrotalcite (TAHT 24)

Raman analysis of the hydrotalcite was performed and the results can be seen in the figure and table below (**Figure 5.29** and **Table 5.13**).

The band component analysis of the material (**Table 5.13**) shows that there are some differences in the material when compared to the precursor hydrotalcite. The most notable differences are the presence of two more carbonate related bands (denoted as C-O vibrations) at 1092 cm^{-1} and 1345 cm^{-1}, which is indicative of a change in the chemical environment of the interlayer carbonate ion. The most likely explanation of these vibrations is that the carbonate has been pushed out of the interlayer spaces and is bonded to the metal cations of the hydrotalcite [105, 107, 108].

The presence of the band at 1064 cm^{-1} is most likely caused by some reformation of the hydrotalcite caused by exposure to the atmosphere during sample preparation for Raman analysis.

Raman Shift (cm^{-1})	**Reported Position (cm^{-1}) [98]**	**Assignment**
107		H-Bonding
144		H Bonding
455	465-475	Al-O-Al- and Mg-O-Mg linkage [103]
543	551	Mg-OH [98, 103]
1064	1068	υ_1 CO_3^{2-} [98, 103]
1092		CO_3^{2-}
1345		C-O Stretching$^-$
3223	3239	H_2O υ_2 bend[121]
3379	3354	$MgAl_2$-OH
3545	3485	Al_3-OH stretch
3651	3615	Al-OH stretch [104]
3699	3673	Mg-OH stretch [104]

Table 5.13: Raman peak list for thermally activated hydrotalcite (TAHT 24)

The presence of the water band at 3223 cm^{-1} is most likely due to small amounts of water being adsorbed on the surface of the material. The other hydroxyl stretching bands are suspected to be indicative of partial reformation of the hydrotalcite upon exposure to the atmosphere.

5.3.4 NITROGEN ADSORPTION/DESORPTION ANALYSIS

The nitrogen adsorption analysis (see **Table 5.14**) of the material shows some difference to the precursor hydrotalcite material. The surface area analysis is consistently 212 % times bigger than the surface area of the precursor hydrotalcite, which shows a decrease in crystallite size. This decrease in crystallite size is supported by the broad series of reflections in the XRD diffraction pattern (**Figure 5.26**).

There has also been a 203 % increase in the total pore volume whilst the average pore diameter has decreased slightly to 96 % compared to the precursor material. This is suggestive that not only has the crystallite size decreased, but the material has become more porous.

	Thermally Activated Hydrotalcite (TAHT 24)	Hydrotalcite Sample
BET Surface Area (m^2/g)	73.6 ± 0.1	34.6 ± 0.1
Single Point Surface Area (m^2/g)	72.1	33.9
Langmuir Surface Area (m^2/g)	101 ± 3	48 ± 1
Total Pore Volume (cm^3/g)	0.4	0.2
Average Pore Diameter (nm)	21.2	22.1

Table 5.14: BET Analysis of thermally activated hydrotalcite (TAHT 24)

5.3.5 SEM/TEM ANALYSIS

SEM imaging of the material shows that there has been a marked decrease in crystal size, as shown in **Figure 5.30**, **Figure 5.31**, **Figure 5.32** and **Figure 5.33** below.

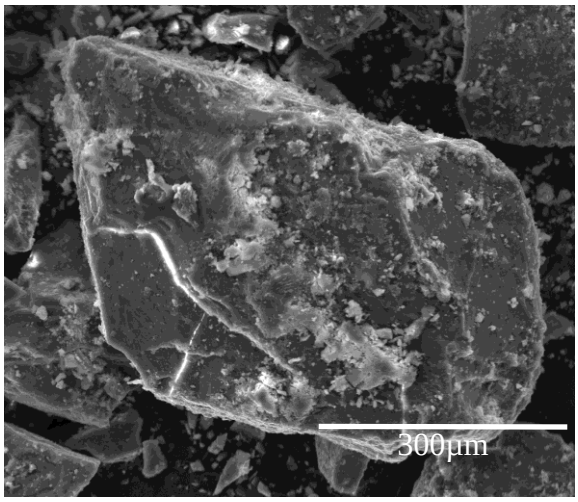

Figure 5.30: SEM image of thermally activated hydrotalcite (TAHT 24) at a magnification of 375x

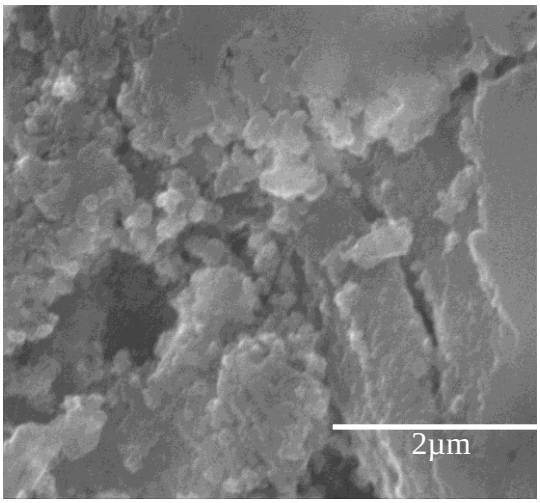

Figure 5.31: SEM image of thermally activated hydrotalcite (TAHT 24) at a magnification of 50 kx

It can be seen by the image at 375x magnification (**Figure 5.30**) that the material forms large secondary particles. The image at 50 kx (**Figure 5.31**) shows that the usually hexagonal platelets have started to fuse together with treatment. It is also clear that there has been a decrease in crystallite size as shown by the TEM images at 250 kx and 600 kx magnification (**Figure 5.32** and **Figure 5.33**), with the average crystallite size being less than 50 nm.

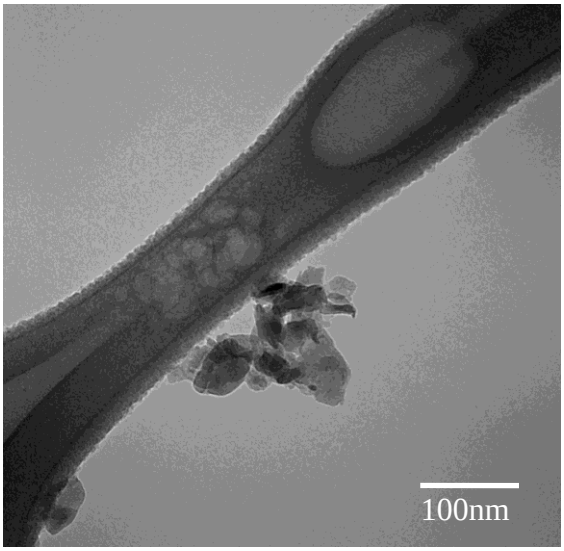

Figure 5.32: SEM image of thermally activated hydrotalcite (TAHT 24) at a magnification of 250 kx

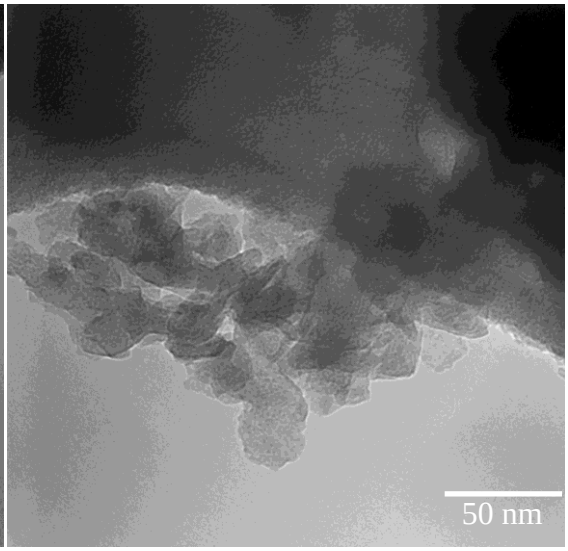

Figure 5.33: SEM image of thermally activated hydrotalcite (TAHT 24) at a magnification of 600 kx

5.4 CHARACTERISATION OF THERMALLY ACTIVATED HYDROTALCITE (TAHT 70)

5.4.1 XRD ANALYSIS

XRD analysis of the material was conducted and the results are shown in **Figure 5.34** and **Table 5.15**. It can be seen from the figure that there has been considerable changes to the material properties, with clear evidence of collapse of the basal spacing, which is shown by the changes in the major hydrotalcite peak, which now sits at 13.49 º2θ as compared to around 11.15 º2θ of the precursor hydrotalcite material (see **Figure 5.34**).

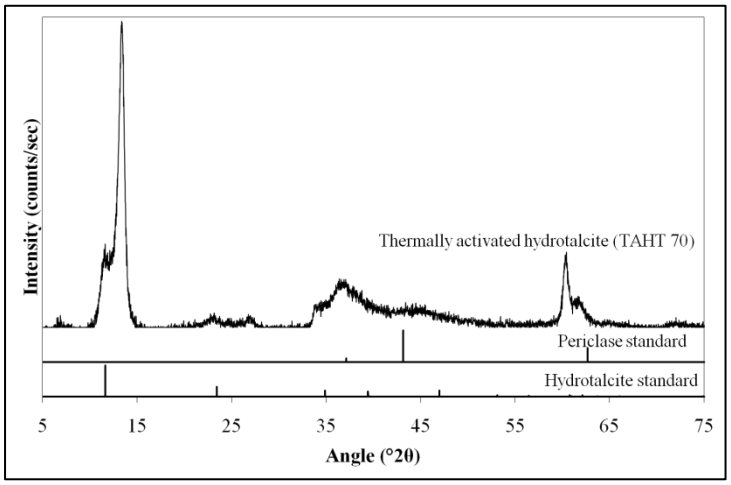

Figure 5.34: XRD of thermally activated hydrotalcite (TAHT 70)

The peak at 11.59 º2θ is in a position expected for the precursor hydrotalcite, and the intensity of the peak is most likely due to some reformation of the material through exposure of the sample to the atmosphere during sample preparation and handling.

The series of broad reflections between 32 and 50 º2θ are due to the formation of mixed metal oxides, including, brucite ($Mg(OH)_2$) periclase (MgO) as well as other metal oxides and hydroxides.

No.	Pos. [°2θ]	d-spacing [Å]	Rel. Int. [%]
1	11.50	7.696	22.74
2	13.32	6.646	100
3	22.94	9.876	2.23
4	26.89	3.316	2.68
5	33.88	2.646	1.27
6	36.62	2.452	4.74
7	44.59	2.031	0.8
8	60.40	1.533	21.17
9	61.85	1.500	6.58

Table 5.15: XRD Peaks for thermally activated hydrotalcite (TAHT 70)

5.4.2 IR ANALYSIS

The table below (**Table 5.16**) shows a list of peaks for the thermally activated hydrotalcite and the expected peaks for hydrotalcite. As can be seen from the IR spectrum (see **Figure 5.35**) and the list of peaks (**Table 5.16**) the water bands are no longer present in the sample. Furthermore, there is evidence of the carbonate being drawn up into the metal cation layer by the splitting of the carbonate ν_3 band into two bands at 1349 cm^{-1} and 1532 cm^{-1}.

Sample Peak (cm^{-1})	Precursor Hydrotalcite Peak (cm^{-1})	Assignment
599	594	M-O Bonding
657	634	M-O Stretching mode [98]
749	733	M-OH Translation mode [98]
839	877	M-OH Deformation
1016	--	υ_1 CO_3^{2-} [105, 107]
1349	1369	υ_3 CO_3^{2-} [98]
1532	1401	CO_3^{2-}
1577	1629	H_2O OH Bending mode [98]
2334	--	Adsorbed CO_2
2364	--	Adsorbed CO_2
3217	3336	$MgAl_2$-OH Stretch [98]
3426	3477	Mg_2Al-OH Stretch [98]
3562	3606	Mg_3-OH Stretch [98]
3648	--	M-OH Stretch
3716	--	M-OH Stretch

Table 5.16: IR Peak list for thermally activated hydrotalcite (TAHT 70)

There is some evidence which suggests that other reactions have occured in the sample. The presence of M-OH stretches at 3706 cm^{-1} and 3648 cm^{-1}, coupled with the band at 1016 cm^{-1} (which is most likely the ν_1 carbonate vibration [105, 107]) and the movement of the M-OH deformation down to 839 cm^{-1} from 877 cm^{-1} suggest that there has been some formation of brucite within the sample. The two peaks at 2334 cm^{-1} and 2364 cm^{-1} are atmospheric carbon dioxide peaks from the background taken by the instrument.

Further evidence of incomplete reformation of the material is the presence of surface adsorbed water (the water bending mode at 1577 cm^{-1} (as compared to 1629 cm^{-1}) but the lack of a band due to interlayer water-carbonate bridging (which is typically around 3050 cm^{-1}) which would be expected if the sample had been able to completely reform hydrotalcite.

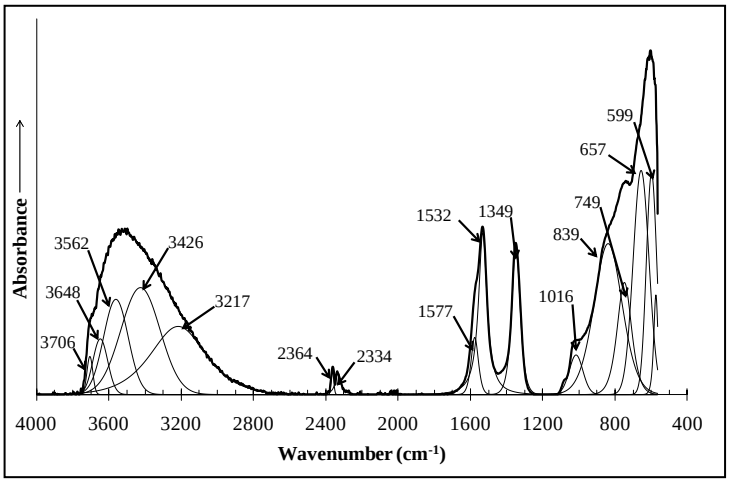

Figure 5.35: IR spectrum of thermally activated hydrotalcite (TAHT 70)

The band at 657 cm^{-1} is most likely a metal-oxygen vibration that is not linked to the M-O stretching mode which is usually found at 635 cm^{-1} in hydrotalcite. This is suggestive of the formation of another metal oxide within the sample material.

5.4.3 RAMAN ANALYSIS

A Raman spectroscopy was performed on the thermally activated hydrotalcite and the results can be seen in the spectrum (**Figure 5.36**) and peak list (**Table 5.17**) below.

Raman Shift (cm^{-1})	Precursor Material (cm^{-1})	Assignment
144		Intermolecular H_2O stretch [120]
464	465-475	Al-O-Al- and Mg-O-Mg linkage [103]
545	552	Al-O-Al Stretch [104]
1058	1068	υ_1 CO_3^{2-} [98, 103]
1354		C-O Stretching mode
1588		H_2O OH Bend
3314	3354	$MgAl_2$-OH
3483	3485	Al_3-OH stretch
3617	3615	Al-OH stretch [104]
3675	3673	Mg-OH stretch [104]

Table 5.17: List of Raman peaks for thermally activated hydrotalcite (TAHT 70)

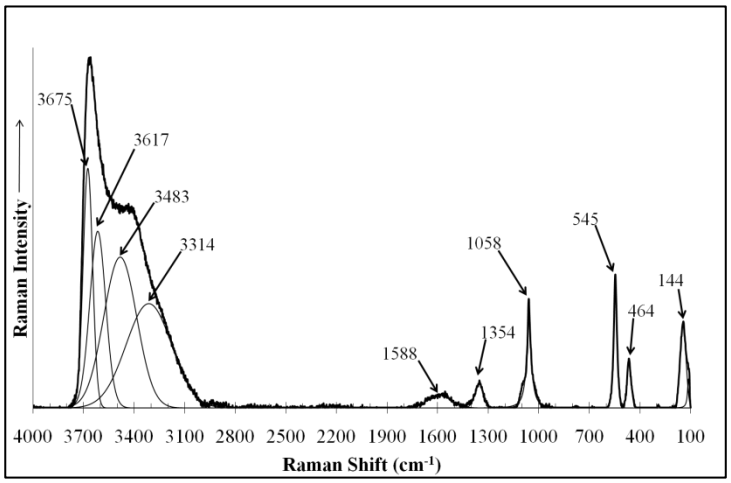

Figure 5.36: Raman spectrum of thermally activated hydrotalcite (TAHT 70)

From the peak list (see **Table 5.17**) it can be seen that there are a number of peaks that can be linked to the typical hydrotalcite bands. The M-O-M linkage vibration at 464 cm^{-1} as well as the Al-O-Al stretch at 545 cm^{-1} in the thermally activated hydrotalcite is in similar locations to the precursor materials. The ν_1 carbonate band is also present in the sample, although it has been shifted to a lower wavenumber. The presence of the $MgAl_2$-OH (3314 cm^{-1}), Al_3-OH (3483 cm^{-1}), Al-OH (3617 cm^{-1}) and Mg-OH stretches (3675 cm^{-1}) are all indicative of the presence of some hydrotalcite within the sample.

There is a small, broad peak around 1354 cm^{-1} in the sample which is a carbon-oxygen vibration and may be caused by the presence of carbonate molecules adsorbed to the surface of the material. There is also a band at 1588 cm^{-1} which is a surface adsorbed water vibration.

5.4.4 NITROGEN ADSORPTION/DESORPTION ANALYSIS

The nitrogen absorption/desorption analysis (**Table 5.18**) shows that there has been a decrease in not only the surface area of the material but also in the porous spaces of the material. This indicates that the thermal treatment has resulted in the formation of materials which are slightly less porous and with a smaller surface area than the precursor hydrotalcite. In fact, the material is much less porous with a much smaller surface area (in the order of 50 %) than the thermally activated hydrotalcites which have been treated for 24 hours, as well as a smaller surface area than the sample that had been treated for 17 hours.

	Thermally Activated Hydrotalcite (TAHT 70)	Hydrotalcite Sample
BET Surface Area (m^2/g)	30.8 ± 0.1	34.6 ± 0.1
Single Point Surface Area (m^2/g)	30.3	33.9
Langmuir Surface Area (m^2/g)	42 ± 1	48 ± 1
Total Pore Volume (cm^3/g)	0.2	0.2
Average Pore Diameter (nm)	21.7	22.1

Table 5.18: BET analysis of thermally activated hydrotalcite (TAHT 70)

5.4.5 SEM AND TEM ANALYSIS

The SEM images show that the individual platelets (**Figure 5.38**) are much smaller than the precursor hydrotalcite (and the other thermally activated hydrotalcites) (see **Figure 5.8**) and that they also form larger particles which can be distinguished at low magnification (**Figure 5.37**). The TEM imaging shows that the crystallites are slightly larger than 100 nm in size (**Figure 5.39**), which is comparable to the precursor material (but smaller than the other thermally activated hydrotalcite samples) (**Figure 5.10**) and that they have started to lose their clear hexagonal shape (**Figure 5.40**). This loss of hexagonal shape is indicative of breakdown of the material from hydrotalcite to mixed metal oxides.

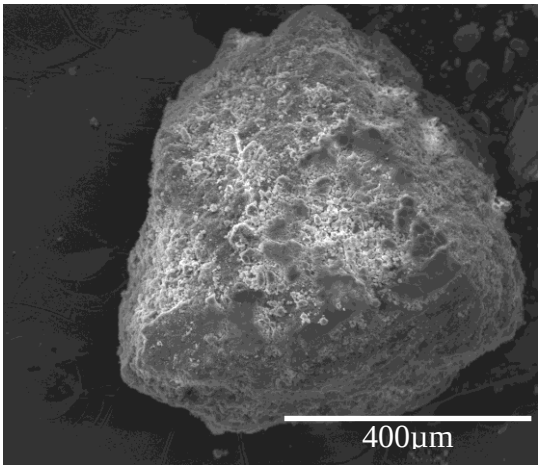

Figure 5.37: SEM image of thermally activated hydrotalcite at a magnification of 300x

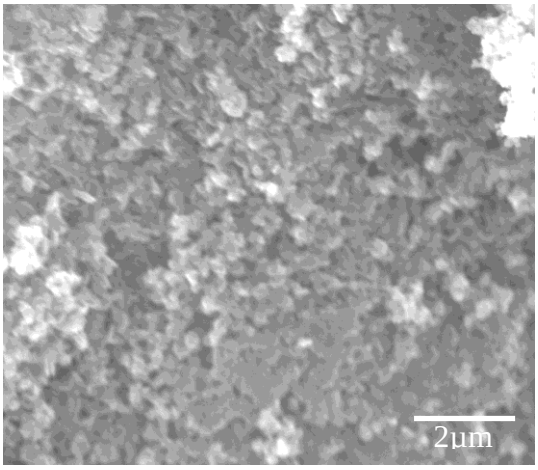

Figure 5.38: SEM image of thermally activated hydrotalcite at a magnification of 25 kx

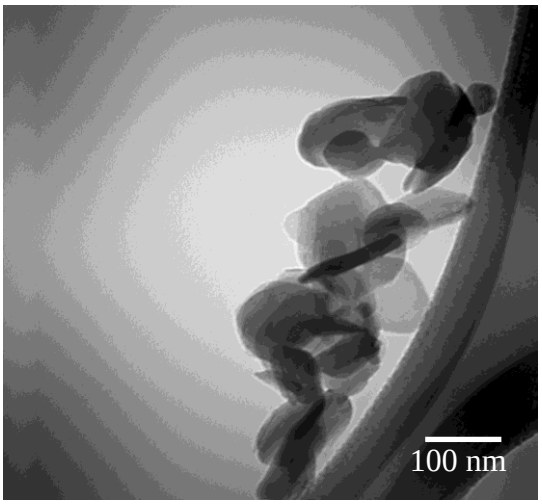

Figure 5.39: TEM image of thermally activated hydrotalcite at a magnification of 200 kx

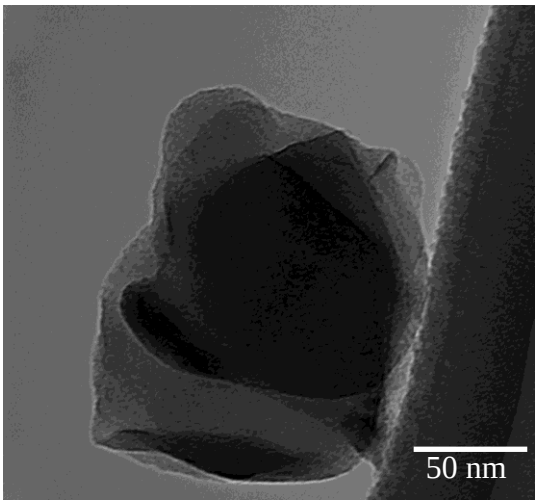

Figure 5.40: TEM image of thermally activated hydrotalcite at a magnification of 400 kx

5.5 CHARACTERISATION OF OXALATE INTERCALATED HYDROTALCITE (CO-PRECIPITATION METHOD)

The intercalation of oxalate into the structure of hydrotalcite shows a number of differences to the precursor hydrotalcite. A number of these changes can be seen in the XRD data, IR, Raman and infrared emission spectra, nitrogen adsorption and thermogravimetric analysis of the oxalate intercalated samples.

5.5.1 XRD ANALYSIS

Number	Position (°2θ)	d-spacing (Å)	Relative Intensity (%)	Predicted Position (PDF 01-089-0460) (°2θ)	Shift (°2θ)
1	11.2	7.9	100	11.6	0.4
2	22.5	3.9	32.56	23.4	0.9
3	34.3	2.6	11.52	34.9	0.6
4	38.1	2.4	3.42	39.4	1.3
5	44.7	2.0	2.03	46.9	2.2
6	60.2	1.5	9.70	60.8	0.5
7	61.5	1.5	8.53	62.1	0.6
8	65.3	1.4	1.68	66.0	0.7
9	71.5	1.3	0.52	71.6	0.1

Table 5.19: Powder XRD peak list for oxalate intercalated hydrotalcite

From the data in **Table 5.19**, it is clear that there has been a shift of the measured peaks from the peaks that could be expected if the intercalated ion was carbonate. As all of the peaks have been shifted to lower angle, it is an indication that the interlayer spacing of the hydrotalcite has increased, which is what could be expected if the interlayer anion was oxalate.

From the XRD pattern, it is clear that the material is highly crystalline, as shown by the well defined peaks in **Figure 5.41** below.

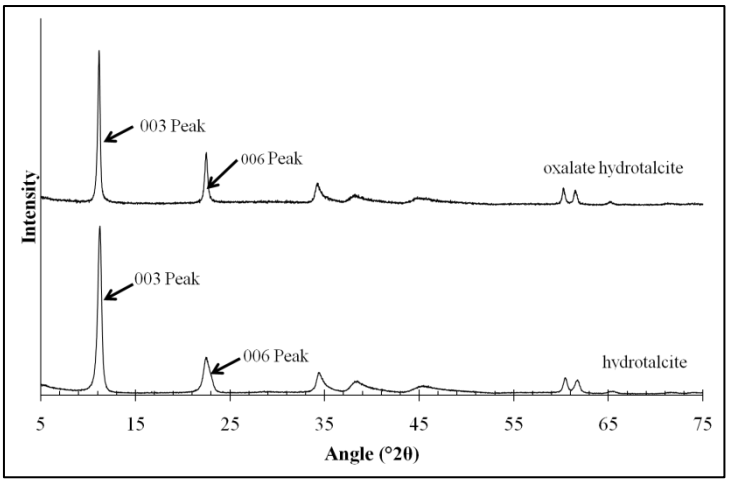

Figure 5.41: Powder XRD of hydrotalcite and oxalate intercalated hydrotalcite

Given the XRD peak shifts, there is evidence to suggest that oxalate was intercalated into the material. Furthermore, given that the Infrared and Raman spectra show clear evidence oxalate being present in the material and there are no peaks that may be associated with free sodium oxalate present in the powder XRD pattern which is suggestive that the oxalate was successfully intercalated into the interlayer spaces of the hydrotalcite. However, as the peak positions are not the same as has been reported in the literature [3, 45, 57], with the exception of Prevot [3], it can be suggested that the oxalate has been intercalated into the material in a preferred orientation along the metal hydroxide sheets.

When the oxalate intercalated hydrotalcite is compared to hydrotalcite that has carbonate in the interlayer spacing, it is observed that the XRD peaks have been shifted to slightly lower angle, which is evidence that the interlayer spacing has increased slightly. As seen in **Table 5.19**, the shifts between the actual position of the peak for the oxalate intercalated hydrotalcite and the calculated peak position for the reference standard (PDF 01-089-0460) are all very slight and this is shown in the comparison between the oxalate intercalated hydrotalcite and the prepared reference hydrotalcite which was used as the precursor material for the thermally activated hydrotalcites (see page 53).

5.5.2 IR ANALYSIS

The recorded spectra of the oxalate intercalated hydrotalcite (**Table 5.20** and **Figure 5.42**) and the infrared spectra for anhydrous sodium oxalate (**Table 5.21**) are recorded below. When the peaks are compared (see **Table 5.20** and **Table 5.21**) it is clear that the oxalate has quite clearly been intercalated into the hydrotalcite structure. The incorporation of oxalate into the structure is also confirmed by the thermal analysis (IES and TGA, see below).

Sample Peak (cm^{-1})	Reported Peak [98] (cm^{-1})	Assignment
579		M-O Bond
602		M-O Bond
637	635	M-O stretch [98]
712	733	M-OH Translation
858	870	M-OH Deformation [98]
1014		CO_3^{2-}
1301	1313	ν_{11} C-O Stretch [122]
1371	1365	CO_3^{2-} [98]
1600		H_2O OH Bend
1632	1640	C=O Stretch
3401	3074	H_2O-CO_3^{2-} Bridging mode
3508	3318	$MgAl_2$-OH Stretch [98]
3577	3467	Mg_2Al-OH Stretch [98]
3641	3606	Mg_3-OH Stretch [98]
3677		Mg-OH

Table 5.20: Infrared Peaks of oxalate intercalated hydrotalcite

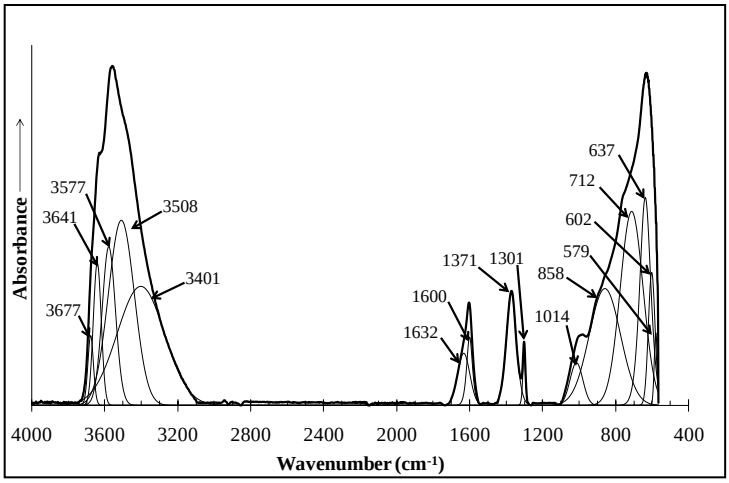

Figure 5.42: Infrared spectrum of oxalate intercalated hydrotalcite with band component analysis

When compared to the infrared spectrum of oxalate and hydrotalcite reference materials (see **Figure 5.43**) a number of similarities between the different materials appear as well as the differences which correlate to the presence of oxalate in the interlayer spaces.

The metal-hydroxide peaks present in the hydroxyl stretching region (3000 cm^{-1}-4000 cm^{-1}) are similar to the bands found in the precursor hydrotalcite materials, albeit they have been shifted significantly to higher wavenumbers, which is indicative of a change in the amount of strain present in the layers. The appearance of an extra band around 3677 cm^{-1} is probably a magnesium hydroxide stretching mode.

The presence of the water stretching bands at 1600 cm^{-1} is what could be expected, particularly due to the presence of a water bridging mode at 3401 cm^{-1} in the hydroxyl stretching region. The appearance of a number of C-O stretches that either correlate with carbonate or oxalate appear at 1632 cm^{-1}, 1371 cm^{-1}, 1301 cm^{-1} and 1014 cm^{-1}. The expected peaks for carbonate in hydrotalcite are 1640 cm^{-1}, 1365 cm^{-1} and 1313 cm^{-1}. Because of the similarities in carbonate and oxalate stretches due to the carbon-oxygen stretching vibrations, it is difficult to accurately assign bands to carbonate or oxalate in this situation. Confirmation of oxalate intercalation had to be performed using another method, such as IES (**Section 5.5.4**) or TGA (**Section 5.5.5**).

Sample Peak (cm^{-1})	Reported Peak [122] (cm^{-1})	Assignment
771	766	COO Deformation
1313	1319	ν_{11} C-O Stretch
1335		
1414	1405	C=O Stretch
1630	1640	C=O Stretch

Table 5.21: Infrared Peaks of anhydrous sodium oxalate

In the fingerprint region of the spectrum (below 1000 cm^{-1}), there is close correlation between the oxalate intercalated hydrotalcite and the reference material, with the exception of the presence of a band at 712 cm^{-1}, instead of at 733 cm^{-1}, which is the M-OH translational mode, which has moved due to changes within the layers caused by hydrogen bonding due to the intercalation of oxalate

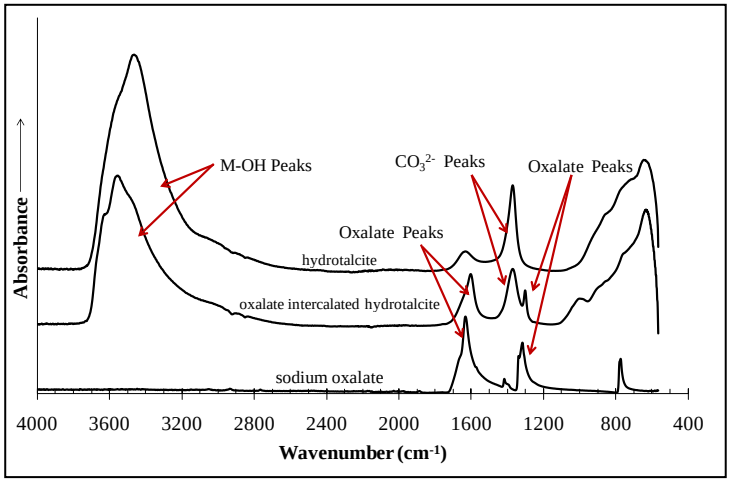

Figure 5.43: Comparison of the infrared spectra of anhydrous sodium oxalate, hydrotalcite and oxalate intercalated hydrotalcite

5.5.3 RAMAN ANALYSIS

The peak list is shown in **Table 5.22** below, with the spectra of the oxalate intercalated hydrotalcite being shown in **Figure 5.44** below. Also shown below are the Raman spectra of oxalate intercalate hydrotalcite as well as hydrotalcite, sodium oxalate and sodium carbonate, which show the correlation between the oxalate intercalated hydrotalcite, the reference hydrotalcite and the reference sodium oxalate.

Raman Shift (cm^{-1})				Assignment
Oxalate intercalated hydrotalcite	**Hydrotalcite Reference Material**	**Sodium carbonate Standard**	**Sodium oxalate Standard**	
122				Hydrogen bonding
144				M-O Bonding [104]
470	474			Al-O-Al and Mg-O-Mg linkage [98]
548	549			Mg-OH Stretch [98]
	692	706		ν_4 CO_3 Band [98]
878			887	δ+ (O-C=O) [123]
1045	1061	1080		υ_3 CO_3 Band [98]
1058				υ_{3a} Carbonate [98]
1107				ν_{as} C-O [124]
1222				O-C-O Wag [124]
1255				O-C-O Wag [124]
1439		1451	1459	ν_s (C-O) [123]
1550				ν_s (C-O) [124]
1611				Water bend
1660				Water bend
3361	3239			Interlayer H_2O [103, 104]
3504	3389			Mg_2Al-OH [102]
3531	3498			$MgAl_2$-OH [98]
3604	3609			Al_3-OH[102]
3658	3660			Mg-OH Stretch [104]

Table 5.22: Peak list for hydrotalcite; oxalate intercalated hydrotalcite; sodium oxalate and sodium carbonate reference materials

In the hydroxyl stretching region (3000-4000 cm^{-1}) there is some variation between the oxalate intercalated hydrotalcite and the hydrotalcite reference material. The first of these variations is in the metal hydroxide bands, which have been shifted to higher wavenumbers, which is suggestive of a variation in chemical environment, caused by the presence of oxalate. This strain is likely caused by the presence of the oxalate anions in the structure of the material.

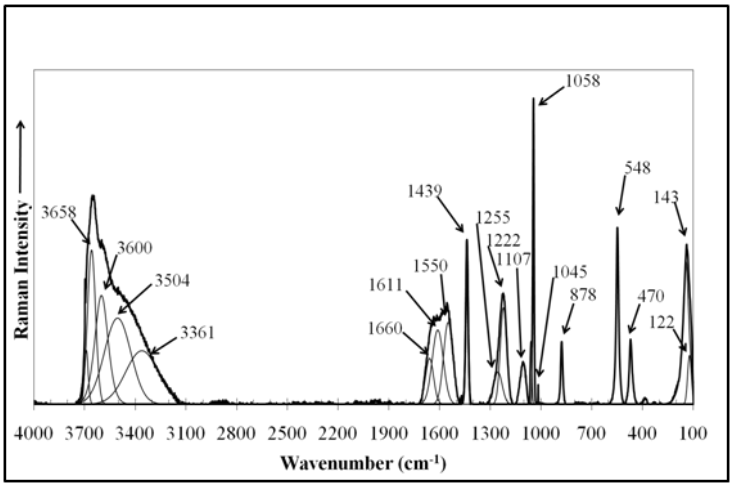

Figure 5.44: Raman spectrum of oxalate intercalated hydrotalcite prepared *in-situ* with band component analysis

There are a number of bands present at 1107 cm^{-1}, 1222 cm^{-1}, 1255 cm^{-1}, 1439 cm^{-1} (ν_s) and 1550 cm^{-1} which can be tentatively assigned to carbon-oxygen bonds in the oxalate anions.

The expected carbonate peaks turn up, but instead of turning up at 1061 cm^{-1} and 1451 cm^{-1}, the peaks are present at 1045 cm^{-1}, 1058 cm^{-1} and 1439 cm^{-1}. This variation in peak positions is most likely explained by the presence of oxalate anions, which are competing with the carbonate anions within the interlayers, constraining the available space and electrostatic repulsion changing the vibrations.

In the lower wavenumber regions (from 100 cm^{-1} to 600 cm^{-1}) there is little difference between the metal-oxygen bands around 470 cm^{-1} - 550 cm^{-1}, which indicates that there has been little change to the metal hydroxide sheets. Furthermore, there is a peak apparent at 156 cm^{-1}, which has been assigned as a metal-oxygen band [104] and there is also a band at 135 cm^{-1} which is most likely a hydrogen bonding band [120, 121, 125]. The presence of these peaks suggests that there is little difference between the metal cation layers of the oxalate and carbonate intercalated hydrotalcites.

5.5.4 IES ANALYSIS

The data for the infrared emission of oxalate intercalated hydrotalcite prepared in-situ can be seen in **Figure 5.45** and the band component analysis can be seen in **Table 5.23**.

With the oxalate intercalated into hydrotalcite *in-situ*, there are some marked differences compared to the reference hydrotalcite. The first of these is in the hydroxyl stretching region, where the water-carbonate bridging mode around 3000 cm^{-1} is present until 400 °C, whereas it disappears around 250 °C in the original hydrotalcite sample

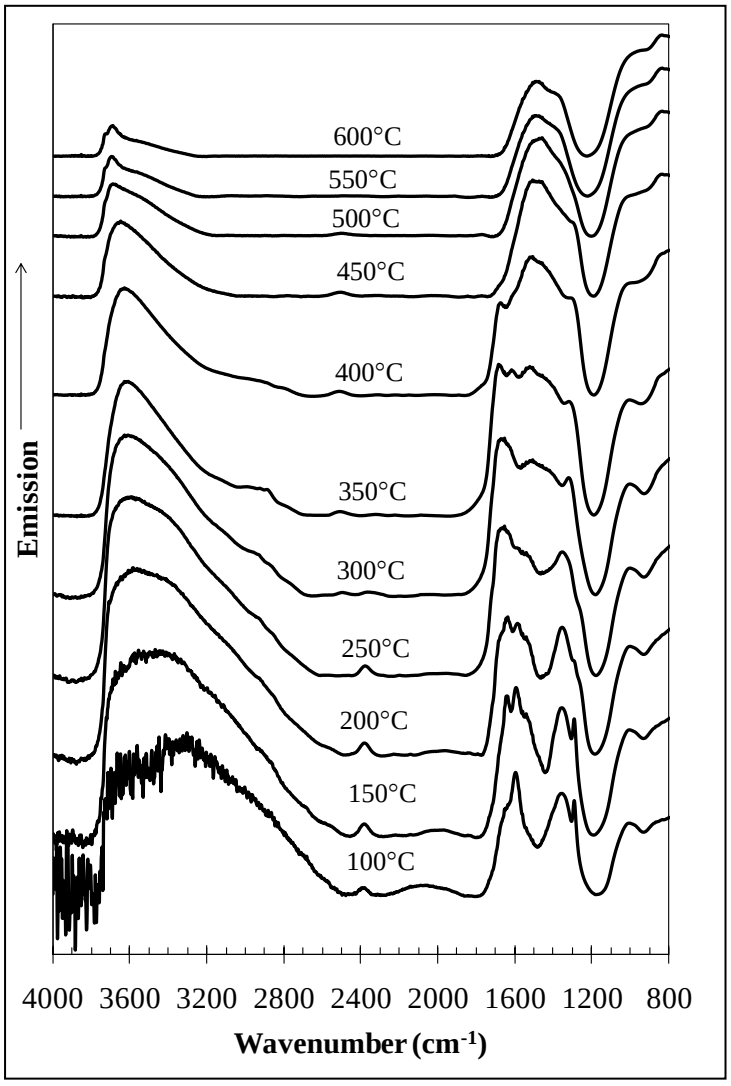

Figure 5.45: Infrared emission spectra for oxalate intercalated hydrotalcite prepared by *in-situ* intercalation

The next major change is when the dehydroxylation begins in the oxalate intercalated sample. In the hydrotalcite reference material, dehydroxylation has begun at 300 °C, whilst the dehydroxylation does not become apparent until 350-400 °C in the oxalate intercalated sample.

The decomposition of the hydroxyl bands in the *in-situ* intercalated hydrotalcite are otherwise similar to the reference material. The hydroxyl bands from 3371 cm^{-1} to 3662 cm^{-1} become less intense until they are almost gone by 600 °C. The magnesium hydroxide stretch around 3710 cm^{-1} remains relatively constant, resulting in the broad band from 3000 cm^{-1} to 4000 cm^{-1} at 100 °C to become much less intense with a spike at 3706 cm^{-1} at 600 °C, which is very similar to the reference hydrotalcite material.

Wavenumber (cm^{-1})	Temperature (°C)										
	100	**150**	**200**	**250**	**300**	**350**	**400**	**450**	**500**	**550**	**600**
	903 (200)	891 (226)	891 (198)	855 (251)	849 (239)	874 (230)	885 (233)	894 (228)	893 (230)	883 (238)	876 (240)
	1026 (121)	1030 (133)	1027 (134)	1025 (136)	1026 (139)	1036 (138)	1040 (135)	1041 (136)	1040 (140)	1038 (151)	1036 (154)
	1288 (19)	1286 (30)	1263 (43)	1254 (45)	--	--	--	--	--	--	--
	1357 (142)	1354 (124)	1349 (141)	1335 (134)	1309 (98)	1296 (85)	1288 (73)	1287 (72)	--	--	--
	1543 (178)	1540 (144)	1556 (183)	1516 (242)	1459 (231)	1415 (186)	1367 (136)	1365 (134)	1358 (105)	1371 (126)	1364 (113)
	1593 (53)	1590 (28)	1586 (32)	1639 (121)	1635 (147)	1586 (196)	1519 (234)	1507 (187)	1496 (158)	1507 (173)	1499 (181)
	1658 (88)	1650 (94)	1666 (90)	1689 (72)	1691 (73)	1690 (78)	1679 (72)	--	--	--	--
	2068 (198)	1996 (134)	1975 (180)	1987 (138)	--	--	--	--	--	--	--
	2384 (34)	2380 (46)	2379 (56)	2375 (57)	--	--	--	--	--	--	--
	3001 (508)	3055 (515)	3070 (519)	3102 (475)	3043 (376)	2934 (239)	3052 (389)	--	--	--	--
	3371 (387)	3341 (325)	3380 (335)	3402 (310)	3376 (329)	3277 (372)	3404 (301)	3415 (301)	3435 (247)	3426 (177)	3431 (180)
	3576 (129)	3507 (217)	3527 (183)	3561 (184)	3544 (197)	3485 (235)	3556 (185)	3558 (180)	3569 (161)	3566 (162)	3568 (157)
	3662 (85)	3625 (135)	3636 (126)	3652 (109)	3639 (117)	3606 (145)	3645 (114)	3649 (108)	3655 (99)	3657 (97)	3658 (95)
	3715 (45)	3701 (72)	3704 (62)	3705 (56)	3697 (65)	3681 (93)	3703 (71)	3705 (66)	3708 (63)	3708 (66)	3706 (69)

Table 5.23: Table of infrared emission bands for oxalate intercalate hydrotalcite prepared by *in-situ* intercalation with peak widths (FWHM) in brackets

There are major differences between the carbonyl (1000-2000 cm^{-1}) regions of the reference material and the *in-situ* oxalate intercalated hydrotalcite. The most obvious one is the number of different peaks present in the oxalate intercalated sample. At 100 °C, there are five peaks in the carbonyl region, compared to the three in the reference material, which is caused by the intercalation of oxalate into the interlayer spaces.

Bands at 1288 cm^{-1}, 1543 cm^{-1} and 1593 cm^{-1} can all be linked to the oxalate in the sample, and they are present until 250 °C, where the band originally at 1288 cm^{-1} disappears and the band at 1543 cm^{-1} rapidly shifts to around 1460 cm^{-1}; whilst the band at 1593 cm^{-1} rapidly shifts to around 1635 cm^{-1}.

Because these frequency shifts occur around the temperature of decomposition for sodium oxalate as noted in CAS 62-76-0; (one of the reagents in the preparation of the sample,) it is suggestive of the breakdown of sodium oxalate on the surface. It also explains why the carbonate bands at 1364 cm^{-1} and 1499 cm^{-1} are so intense at 600 °C when compared to the reference hydrotalcite.

However, bands that are linked to the presence of oxalate in the sample 1357 cm^{-1}, 1658 cm^{-1} and 3001 cm^{-1} are still present at 400 °C, which is suggestive of oxalate still being present at that temperature.

The fingerprint region (less than 1000 cm^{-1}) shows two bands of interest in this material. The first band of interest is the band at 1026 cm^{-1}, which gradually shifts to 1036 cm^{-1} over the course of the heating and can be linked to the ν_1 carbonate band. As this ν_1 carbonate band does not decrease in intensity like in the IES of the reference hydrotalcite (**Section 5.1.4**), this band can be linked to the presence of sodium carbonate in the sample which was most likely formed when the oxalate in the sample decomposed.

The band at 903 cm^{-1} is similar to the band found at 880 cm^{-1} in the reference hydrotalcite, and was previously linked to ν_2 carbonate band (**Section 5.5.2** above). This band also exhibits the same behaviour of the ν_2 carbonate band in the reference hydrotalcite, suggesting that the structure of the oxalate intercalated hydrotalcite has not completely broken down upon heating.

5.5.5 TGA ANALYSIS

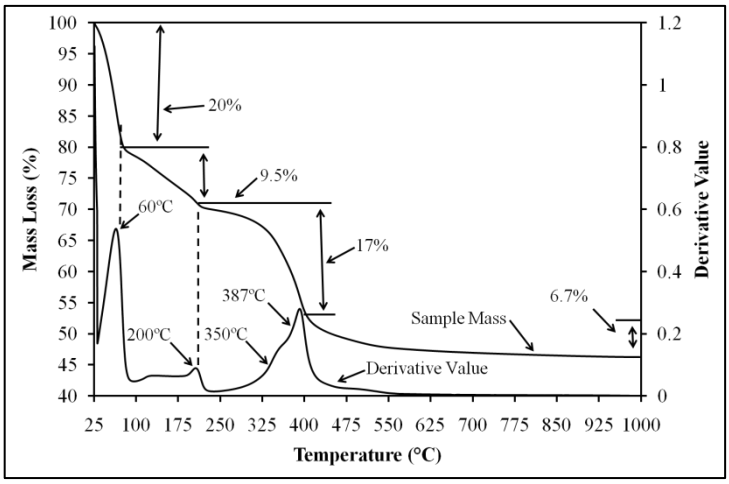

Figure 5.46: TGA for oxalate intercalate hydrotalcite prepared by *in-situ* intercalation

The thermogravimetric analysis of the sample shows a number of features that differ from the reference material (on page 57). The first of these differences is a mass loss step around 60 °C, which corresponds to the loss of loosely bound surface water. The large proportion of the mass loss indicates that this sample was still quite wet when analysed, despite being stored under vacuum for over a month.

Temperature (°C)	Mass Loss (%)	Actual Mass (AMU)	Theoretical Mass (AMU)	Proposed Formula
25	0	743.2	743.8	$Mg_6Al_2(OH)_{16}(C_2O_4).10H_2O$
60	20	594.6	599.8	$Mg_6Al_2(OH)_{16}(C_2O_4).2H_2O$
200	9.5	532.3	545.8	$Mg_6Al_2O(OH)_{14}(C_2O_4)$
388	17	397.6	393.8	$Mg_6Al_2O_2(OH)_6(CO_3)$
1000	6.7	343.8	343.8	$5MgO + MgAl_2O_4$

Table 5.24: Mass loss steps for oxalate intercalated hydrotalcite prepared by *in-situ* intercalation

The 9.5 % mass loss around 200 °C corresponds to the loss of water molecules that are more tightly bound to the hydrotalcite and found in the interlayer spaces.

The decomposition of the layered structure of the material is much different to the reference material in that instead of a single decomposition step at 280 °C, there are a number of simultaneous decomposition steps occurring from around 300 °C. The quite obvious shoulder around 350 °C corresponds to the loss of carbon monoxide and water from the sample and is indicative of a simultaneous dehydroxylation and decomposition of the oxalate to carbonate. Furthermore the second decomposition step at 388 ºC is further dehydroxylation, balanced by the simultaneous absorption of carbonate into the metal cation layer (see section 5.5.4, above) followed by some decarbonisation of the sample. The mass loss tails to at least 550 ºC, which is completion of the decarbonisation step.

5.5.6 NITROGEN ADSORPTION/DESORPTION ANALYSIS

It can be seen that the surface area reported here is a much larger surface area than standard hydrotalcite (in the order of 325 %). It is most likely that the crystals are smaller than the hydrotalcite prepared as a reference material, which results in the oxalate hydrotalcite having a larger surface area than the reference hydrotalcite, and this can be seen in the SEM Images (see **Figure 5.47**, **Figure 5.48** and **Figure 5.49** below).

	Oxalate intercalated Hydrotalcite	**Hydrotalcite Sample**
BET Surface Area (m^2/g)	112.7 ± 0.2	34. 6 ± 0.1
Single Point Surface Area (m^2/g)	110.7	33.9
Langmuir Surface Area (m^2/g)	154 ± 4	48 ± 1
Total Pore Volume (cm^3/g)	0.8	0.2
Average Pore Diameter (nm)	27.3	22.1

Table 5.25: BET analysis of oxalate intercalated hydrotalcite

5.5.7 SEM/TEM ANALYSIS

The SEM images (see **Figure 5.47**, **Figure 5.48** and **Figure 5.49** below) show that the material has a definite crystalline structure, although individual crystals are impossible to see on anything other than at 40 kx magnification, which shows that there may be some crystals, but that they are so small that they cannot be individually resolved without TEM imaging.

Figure 5.50 is a representative TEM image of the hydrotalcite crystals that are found in the sample. The image clearly shows that the hexagonal brucite structure of hydrotalcite has been retained; while **Figure 5.51** shows layering in a region with a high concentration of crystals and **Figure 5.52** is a close up of the circles area in **Figure 5.51** showing that the layers in the crystal structure are irregularly spaced. These layers have an average spacing of approximately 5.4 Å in this sample, which is most likely the basil spacing. It has to be remembered that the interlayer spacing reported here is for that small area, whilst XRD is a bulk characterisation method, which can result in differences in interlayer spacing between analysis methods.

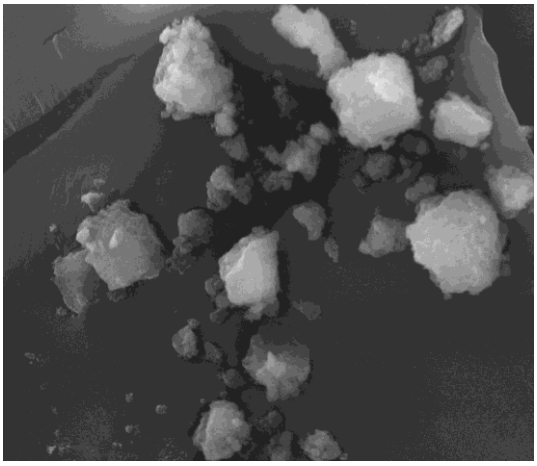

Figure 5.47: SEM image of oxalate intercalated hydrotalcite at a magnification of 2400x

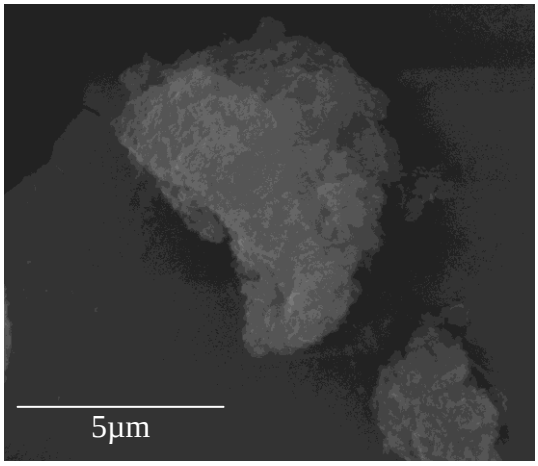

Figure 5.48: SEM image of oxalate intercalated hydrotalcite at a magnification of 20 kx

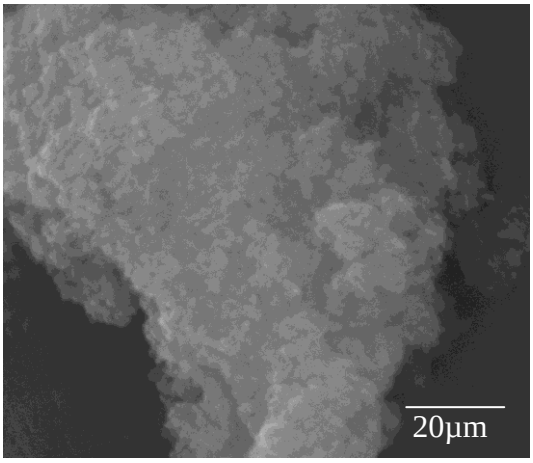

Figure 5.49: SEM image of oxalate intercalated hydrotalcite at magnification of 40 kx

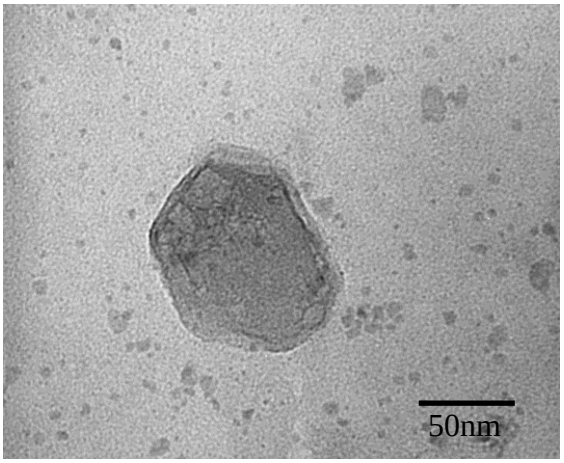

Figure 5.50: TEM image of a single oxalate intercalated hydrotalcite crystal at a magnification of 250 kx

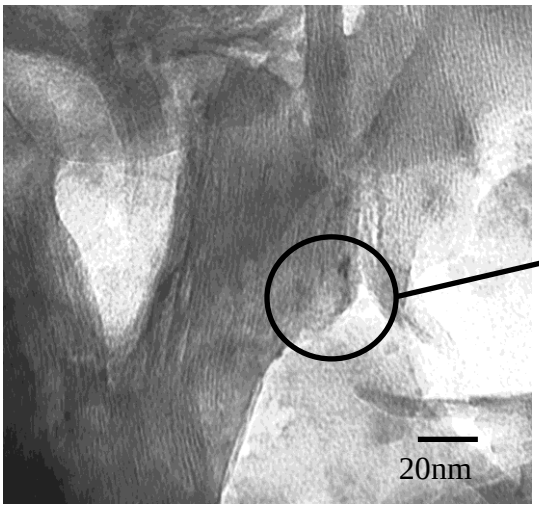

Figure 5.51: Hi resolution TEM image showing layers in oxalate intercalated hydrotalcite at a magnification of 390kx

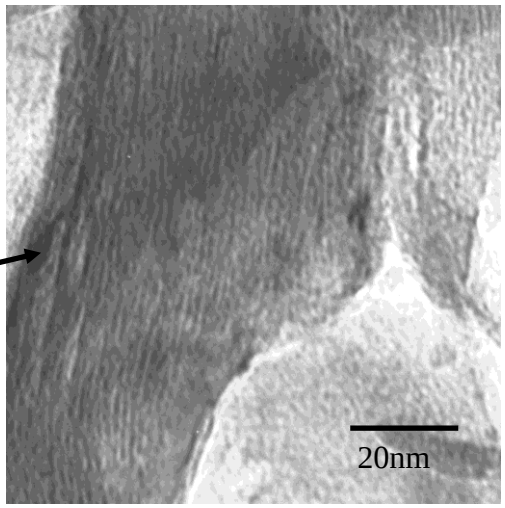

Figure 5.52: Hi resolution image of circled area in **Figure 5.51**

5.6 CHARACTERISATION OF OXALATE INTERCALATED HYDROTALCITE (RE-CO-PRECIPITATION METHOD)

Characterisation of hydrotalcite intercalated by oxalate through the use of a modified re-co-precipitation method shows some interesting changes when characterised. Particular areas of interest include the vibrational spectroscopy and the thermogravimetric analysis. BET and electron microscopy also show some differences to the precursor hydrotalcite.

5.6.1 XRD ANALYSIS

The XRD pattern is shown in **Figure 5.53** below with the major reflections reported in **Table 5.26**.

Number	Position (°2θ)	d-spacing (Å)	Relative Intensity (%)	Oxalate HT (CPM) Peak Position (°2θ)
1	11.2	7.7	100	11.2
2	22.6	3.9	35.8	22.5
3	34.2	2.6	13.3	34.3
4	38.7	2.3	9.4	38.
5	45.7	2.0	4.2	44.7
6	60.2	1.5	11.1	60.2
7	65.3	1.4	2.1	61.5
8	72.1	1.3	1.5	65.3

Table 5.26: Powder XRD of oxalate intercalated hydrotalcite prepared by the re-co-precipitation method

The XRD pattern is quite clearly defined which suggests that the material is highly crystalline, which is shown in **Figure 5.53**. Furthermore, the peaks are narrow, which is suggestive of larger crystal sizes.

A comparison between the XRD patterns for the oxalate intercalated hydrotalcite prepared using the re-co-precipitation method and the reference hydrotalcite (**Figure 5.54**) shows that there has been some shift in the 003 peak, which is suggestive of the intercalation of hydrotalcite. Furthermore, there is some variation in relative intensities for some of the other peaks, which is also suggestive of intercalation of oxalate having occurred.

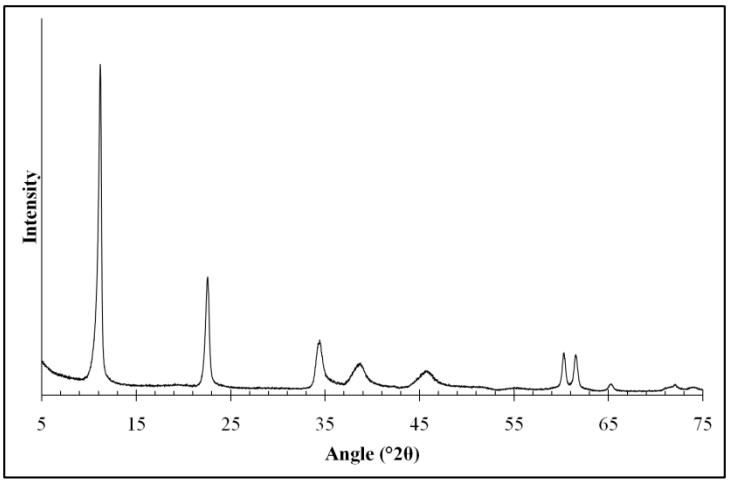

Figure 5.53: XRD of Oxalate intercalated hydrotalcite prepared by the re-co-precipitation method

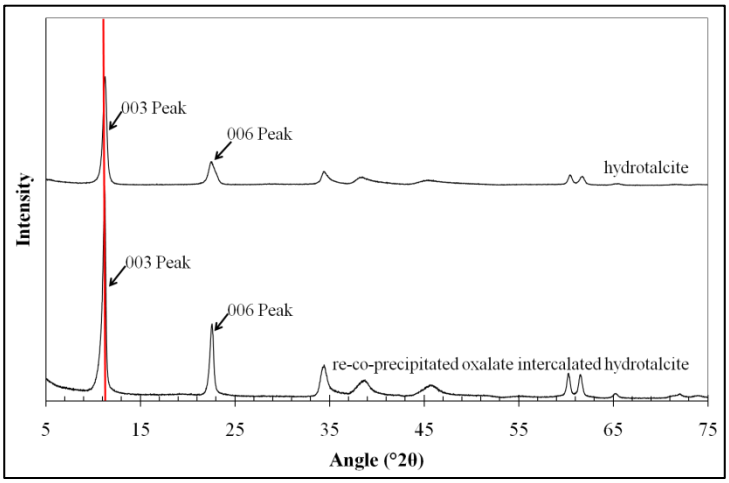

Figure 5.54: XRD comparison of hydrotalcite and oxalate intercalated hydrotalcite prepared by the re-co-precipitation method

A comparison of the XRD pattern of the oxalate intercalated hydrotalcite to the precursor material, it can be seen that there is a very slight shift in the 003 This is some indication that the interlayer anion may be something other than carbonate. This is supported by the infrared and Raman spectra.

A Rietveld refinement of the unit cell size was undertaken using the unit cell parameters of the hydrotalcite standard material (3.054 ± 0.002 Å for the *a* and *b* unit parameters and 22.81 ± 0.02 Å for the *c* unit parameter.) The Rietveld refinement determined that the *a* and *b* axis parameters of the material had increased very slightly to 3.068 ± 0.001 Å whilst the *c* unit parameter had significantly increased from 22.81 Å to 23.61 ± 0.02 Å, which is what could be expected upon the intercalation of oxalate into the hydrotalcite material.

5.6.2 IR ANALYSIS

The IR spectrum shown in **Figure 5.55** below is very similar to the IR spectra for oxalate intercalated hydrotalcite shown earlier in **Figure 5.42**. The peak list is shown in **Table 5.27** below.

Sample Peak (cm^{-1})	Precursor Peak (cm^{-1})	Assignment [98]
598	594	M-O-M Bridging mode
735	634	M-O Stretching mode
726	733	M-OH Translation mode
878	877	M-OH Deformation and υ_2 CO_3^{2-}
1301		oxalate
1368	1369	υ_3 CO_3^{2-}
1398	1401	υ_{3a} CO_3^{2-}
1601		H_2O OH bending mode/oxalate
1633	1629	H_2O OH Bending mode
1655		Oxalate
3095	3074	CO_3^{2-} -H_2O Bridging mode
3371		Al_3-OH Stretch
3492	3336	$MgAl_2$-OH Stretch
3582	3477	Mg_2Al-OH Stretch
3653	3606	Mg_3-OH Stretch

Table 5.27: Infrared peaks of oxalate intercalated hydrotalcite prepared by re-co-precipitation

The hydroxyl stretching region from 4000 cm^{-1} to 3000 cm^{-1} shows a number of peaks which correlate to the typical metal hydroxide bands present in hydrotalcite. The peaks in the fingerprint region (575 cm^{-1} to 1000 cm^{-1}) also show close correlation to what is expected for hydrotalcite materials (as shown by the analysis of the hydrotalcite precursor on page 53.)

The presence of oxalate in the sample is confirmed by peaks at 1301 cm^{-1} and 1655 cm^{-1}. There is also a very large band at 1601 cm^{-1} as well as another, less intense band around 1633 cm^{-1} which is also probably a water band.

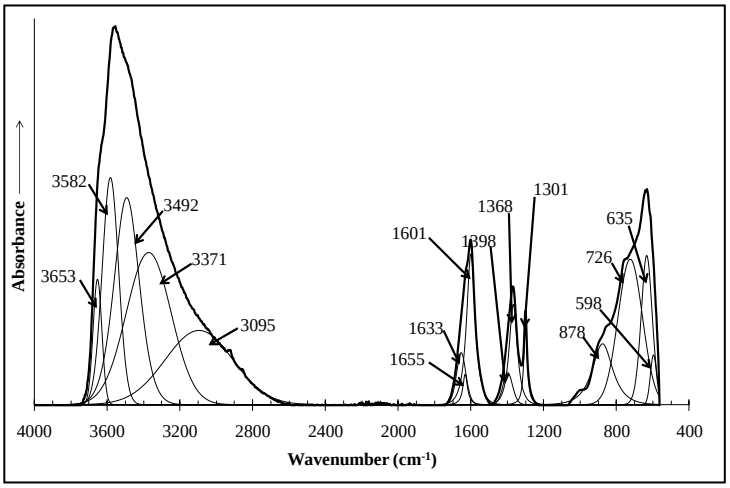

Figure 5.55: Infrared spectrum of oxalate intercalated hydrotalcite prepared by re-co-precipitation

A comparison between the two oxalate intercalated hydrotalcites shows that there are some changes in the spectroscopy of the two materials; with the most notable change being around the 1600 cm^{-1} band.

The peak at 1655 cm^{-1} in the hydrotalcite prepared by re-co-precipitation is much more intense than the same band in the hydrotalcite prepared by *in-situ* intercalation.

5.6.3 RAMAN ANALYSIS

The Raman spectrum of the sample shown below is very similar to the other oxalate intercalated hydrotalcite shown above (**Section 5.5.3** on page 92) which is seen in the spectrum (**Figure 5.56**) and the table (**Table 5.28**) below.

The bands in the hydroxyl stretching region (4000 cm^{-1} to 3000 cm^{-1}) are very similar, although the band around 3688 cm^{-1} is now missing and a number of other bands have been shifted to lower wavenumbers, which is suggestive that there has been a change to bonding between the oxalate, water and the metal cation layer within the crystals due to the change in preparation techniques.

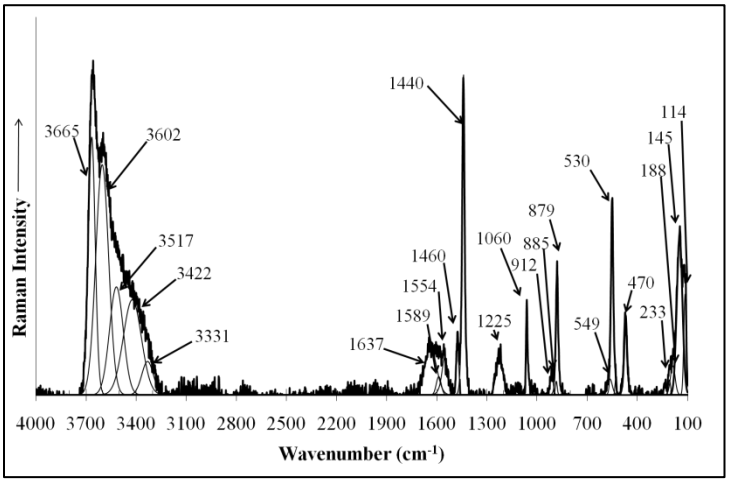

Figure 5.56: Raman spectrum of oxalate intercalated hydrotalcite prepared by re-co-precipitation

The next major change to the Raman spectrum of the sample is that the bands around 2000 cm^{-1} have disappeared, which is suggestive of the carbon-carbon bonds being more constrained than in the other oxalate intercalated hydrotalcite sample.

In the fingerprint region of the spectrum (below 1000 cm^{-1}) a number of peaks have had shoulders appear, most notably around 880 cm^{-1}, 540 cm^{-1} and 200 cm^{-1}. The shoulders appearing around 880 cm^{-1} and 540 cm^{-1} suggest that there has been a change to the local environment for the vibrating units which correlate to those stretches.

The band at 114 cm^{-1} and the bands between 180 cm^{-1}-230 cm^{-1} are most likely hydrogen bonding stretches. The increased number of hydrogen bonding bands is once again suggestive of a slight change to those vibrations; most likely due to constraint of the oxalate anions in the interlayer space.

Raman Shift (cm^{-1})				Assignment
Oxalate intercalated hydrotalcite	**Hydrotalcite Reference Material**	**Sodium carbonate Standard**	**Sodium oxalate Standard**	
114				Hydrogen Bonding
145				Hydrogen Bonding
156				M-O Bonding [104]
188				Intermolecular H_2O [120]
208				Hydrogen Bonding
233				Hydrogen Bonding
470	474			Al-O-Al and Mg-O-Mg linkage [98]
530				Al-OH Stretch
549	549			Mg-OH Stretch [98]
	692	706		ν_4 CO_3 Band [98]
879				C-O Bond
885			887	δ+ (O-C=O) [123]
912				C-O Bond
1060	1061	1080		υ_3 CO_3 Band [98]
1225				O-C-O Wag [124]
1440				C-O
1460		1451	1459	ν_s C-O [123]
1476				ν_s C-O [124]
1554				ν_s C-O [124]
1589				ν_s C-O [124]
1637				H_2O OH Bend
3331	3239			Interlayer H_2O [103, 104]
3422	3389			Mg_2Al-OH [102]
3517	3498			$MgAl_2$-OH [98]
3602	3609			Al_3-OH [102]
3665	3660			Mg-OH Stretch [104]

Table 5.28: Raman peaks for oxalate intercalated hydrotalcite prepared by re-co-precipitation

5.6.4 IES ANALYSIS

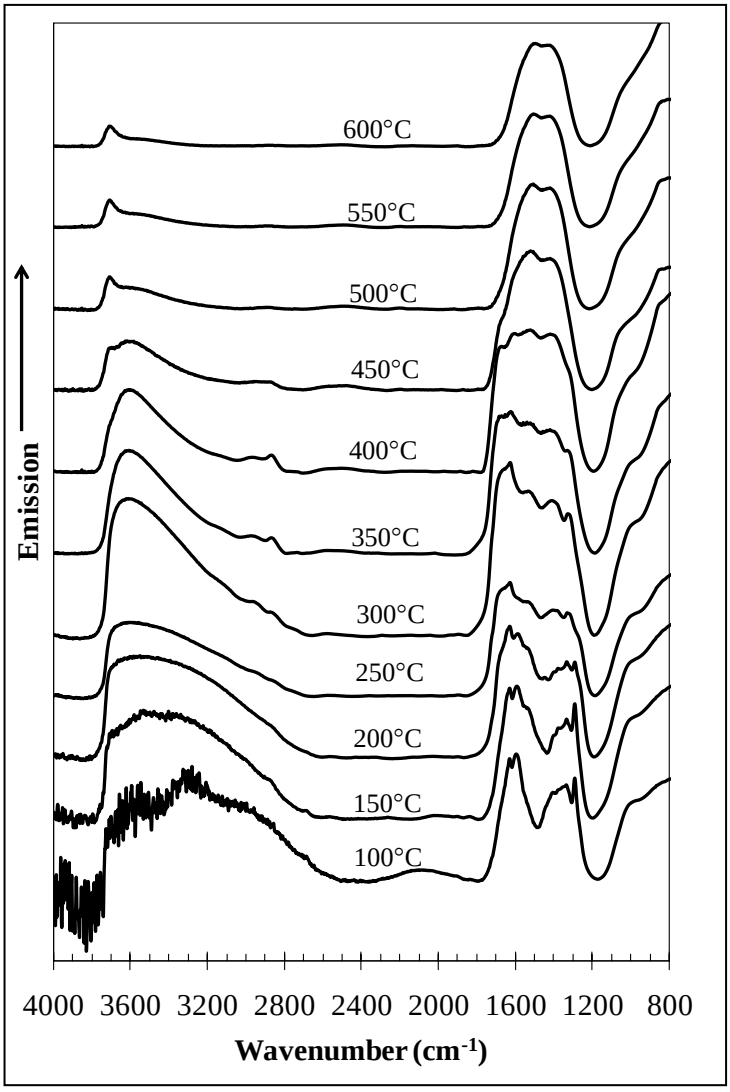

Figure 5.57: Infrared emission spectra of oxalate intercalated hydrotalcite prepared by re-co-precipitation

The oxalate intercalated hydrotalcite (see **Figure 5.57** and **Table 5.29**) prepared by re-co-precipitation shows some differences compared to the precursor material in the hydroxyl stretching region (3000 cm^{-1} to 4000cm^{-1}). The first of these is that the dehydroxylation of the material does not begin to occur until approximately 400 °C. This is shown by a rapid decrease in the intensity of the metal hydroxide stretches around 3350 cm^{-1} ($MgAl_2$-OH), 3570 cm^{-1} (Mg_2Al-OH) and 3662 cm^{-1} (Mg_3-OH). The Mg-OH Stretch around 3712 cm^{-1} becomes a clear band and then the most intense peak in this region after 450 °C, indicating the migration of protons from the interlayer to the outside of the layers as the structure breaks down to allow dehydroxylation to occur [105, 107].

The carbonate region shows the presence of two bands that are related to the presence of oxalate around 1330 cm^{-1} and 1630 cm^{-1}. The band at 1328 cm^{-1} migrates to 1306 cm^{-1} as the sample decomposes at around 400 °C and the band at 1632 cm^{-1} migrates to 1626 cm^{-1} as the oxalate decomposes to carbonate.

The fingerprint region of the spectrum (less than 1000 cm^{-1}) shows two bands of interest. The first band is around 930 cm^{-1}, which disappears at 450 °C and could be linked to the presence of oxalate in the sample (as the other oxalate bands disappear at the same time).

Wavenumber (FWHM) (cm^{-1})	Temperature (°C)										
	100	**150**	**200**	**250**	**300**	**350**	**400**	**450**	**500**	**550**	**600**
	783 (210)	747 (244)	775 (233)	809 (236)	849 (252)	856 (240)	865 (220)	871 (204)	869 (239)	866 (268)	861 (238)
	926 (154)	910 (178)	926 (179)	944 (174)	1005 (111)	1013 (108)	1009 (104)	992 (100)	--	--	--
	1028 (121)	1029 (141)	1033 (135)	1035 (133)	1073 (88)	1082 (81)	1078 (87)	1067 (99)	1042 (135)	1038 (138)	1034 (142)
	1278 (57)	--	1264 (54)	1263 (57)	1262 (57)	--	--	--	--	--	--
	1290 (17)	1287 (51)	1290 (27)	--	--	1301 (92)	1306 (76)	--	--	--	--
	1328 (53)	1332 (28)	1321 (55)	1314 (61)	1311 (60)	1313 (40)	--	--	--	--	--
	1367 (59)	1370 (112)	1378 (110)	1388 (132)	1396 (139)	1404 (151)	1392 (146)	1373 (137)	1386 (136)	1386 (136)	1383 (135)
	1423 (111)	--	1451 (60)	--	--	--	--	--	--	--	--
	1551 (97)	1542 (169)	1537 (141)	1535 (162)	1523 (124)	1519 (111)	1533 (152)	1520 (185)	1534 (182)	1528 (176)	1522 (177)
	1592 (45)	1593 (46)	1586 (37)	1584 (32)	--	--	--	--	--	--	--
	1632 (45)	1634 (35)	1634 (73)	1629 (78)	1638 (123)	1636 (152)	1634 (99)	1626 (107)	--	--	--
	1665 (83)	1662 (85)	--	--	--	--	--	--	--	--	--
	--	--	1683 (60)	1688 (76)	1699 (60)	1701 (54)	1697 (65)	1688 (53)	--	--	--
	3007 (451)	3066 (413)	3188 (377)	3190 (366)	3173 (286)	3132 (238)	3163 (269)	3230 (387)	--	--	--
	3340 (300)	3325 (311)	3414 (259)	3416 (250)	3393 (245)	3382 (274)	3398 (245)	--	--	--	--
	--	3484 (217)	3547 (179)	3547 (172)	3533 (174)	3533 (189)	3528 (190)	3463 (245)	3387 (270)	3408 (281)	3467 (227)
	3570 (144)	3591 (154)	3636 (123)	3633 (118)	3622 (121)	3620 (131)	3610 (121)	3583 (158)	3554 (182)	3570 (195)	3586 (149)
	3662 (73)	3673 (87)	3690 (74)	3686 (71)	3677 (76)	3671 (81)	3669 (86)	3660 (103)	3657 (101)	366 (85)	3669 (76)
	3712 (32)	3714 (42)	3717 (32)	3713 (35)	3708 (40)	3707 (47)	3716 (49)	3714 (52)	3712 (52)	3712 (51)	3712 (52)

Table 5.29: IES peak data of oxalate intercalated hydrotalcite prepared by re-co-precipitation

The second band of interest is the ν_1 carbonate band at 1034 cm^{-1} which becomes clearly present after 250 ºC. This band is linked to the movement of carbonate from the interlayer spaces into the metal cation layer as dehydroxylation begins. The appearance of this band corresponds with the start of the decomposition of oxalate. This suggests that a number of simultaneous processes are occurring in this sample. These simultaneous processes are:

- Decomposition of oxalate to carbonate;
- Dehydroxylation of the metal cation layer; and
- Migration of carbonate anions into the metal cation layer.

These last two steps are the same as in the decomposition of hydrotalcite, which was first proposed by Stanimirova *et al.* in 1999 [105].

5.6.5 TGA ANALYSIS

The TGA data (**Figure 5.58**) shows significant differences to the precursor hydrotalcite sample and the oxalate intercalated hydrotalcite prepared by *in-situ* intercalation (**Figure 5.46**). The first difference is in the water loss steps below 200 ºC, which is significantly lower than the *in-situ* intercalated oxalate hydrotalcite and slightly lower than the precursor hydrotalcite. These mass loss steps can be attributed to the loss of water that has been absorbed into the interlayer spaces. The reason for the elevated temperatures is most likely due to a lack of escape routes for interlayer water molecules due to the small pores found in the nitrogen adsorption analysis (**Section 5.6.6**).

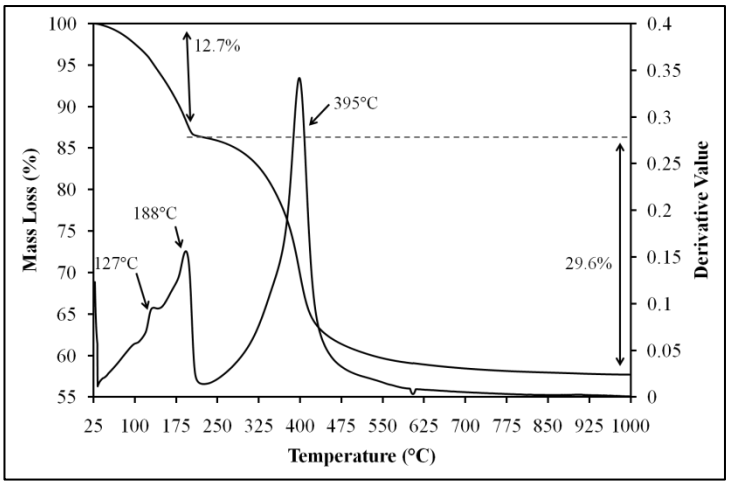

Figure 5.58: TGA of oxalate intercalated hydrotalcite prepared by re-co-precipitation

The second mass loss step occurs as a large band centred around 400 °C.

This mass loss can be attributed to the tree simultaneous process outlined before: dehydroxylation, decomposition of the oxalate to carbonate and the migration of the carbonate into the metal cation layer. The mass loss then tails off slowly to approximately 775 °C, and this is linked to decarbonisation and dehydroxylation of the sample (which is supported in **Section 5.6.4** above.)

5.6.6 NITROGEN ABSORPTION/DESORPTION ANALYSIS

	Oxalate intercalated Hydrotalcite	**Reference Hydrotalcite Material**
BET Surface Area (m^2/g)	54.4 ± 0.1	34.6 ± 0.1
Single Point Surface Area (m^2/g)	53.4	33.9
Langmuir Surface Area (m^2/g)	74 ± 2	48 ± 1
Total Pore Volume (cm^3/g)	0.2	0.2
Average Pore Diameter (nm)	15.3	22.1

Table 5.30: BET analysis of oxalate intercalated hydrotalcite prepared by re-co-precipitation

Calculations from the nitrogen isotherm data of the material shows that there has been an increase in the BET, Langmuir and single point surface areas (which have increased to about 155 % of the precursor material), as well as the average pore diameter (which has increased to 109 % of the precursor hydrotalcite) although the total pore volume has decreased slightly (down to 69 % of the precursor hydrotalcite material). This is consistent with what could be expected by the intercalation of oxalate instead of carbonate into the interlayer spaces, as oxalate is a larger anion than carbonate, which in turn prevents access of N_2 molecules into the interlayer spaces.

5.6.7 SEM/TEM ANALYSIS

The SEM images (**Figure 5.59** and **Figure 5.60**) show that the particles in the sample are moderately sized, but are too small to be accurately resolved using SEM imaging. Furthermore, the SEM images show that the individual crystals show some evidence of being arranged into a preferred orientation when agglomerated.

The TEM Images (**Figure 5.61** and **Figure 5.62**) show obvious signs of preferred orientation as small groups of crystals are all aligned in the same way, being either showing their hexagonal face or their edges in the image. From the images, it is clear that the crystals are hexagonal with a crystal size somewhere between one hundred and two hundred nanometres across; the measurement is however biased towards larger crystal sizes.

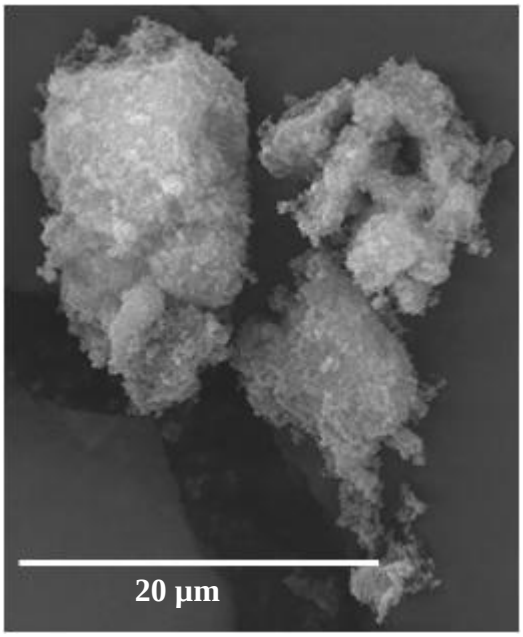

Figure 5.59: SEM image of oxalate intercalated hydrotalcite prepared by re-co-precipitation at a magnification of 5000 x

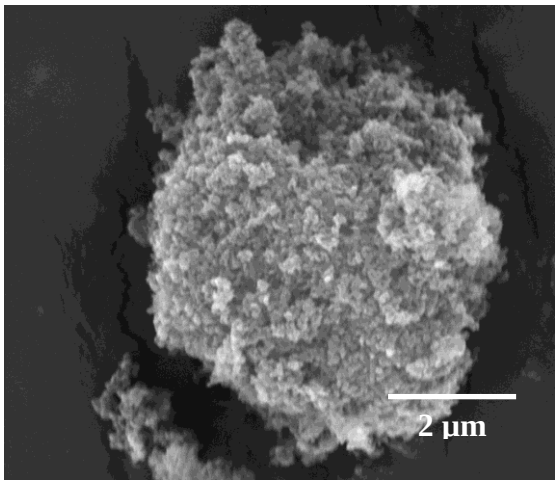

Figure 5.60: SEM image of oxalate intercalate hydrotalcite prepared by re-co-precipitation at a magnification of 30 kx

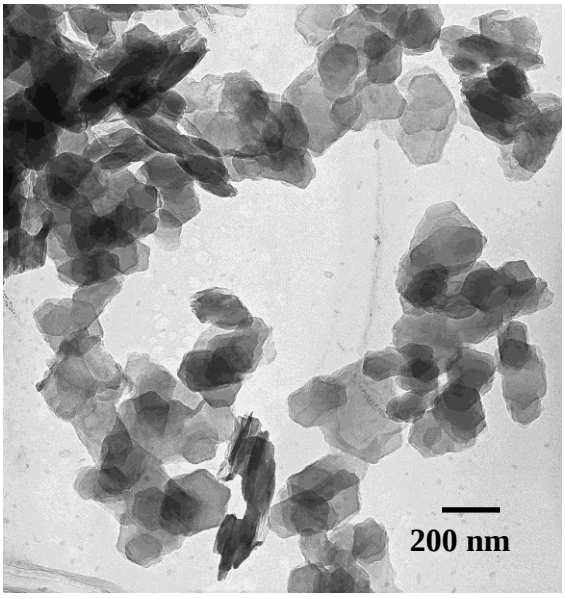

Figure 5.61: TEM image of oxalate intercalate hydrotalcite prepared by re-co-precipitation at a magnification of 380 kx

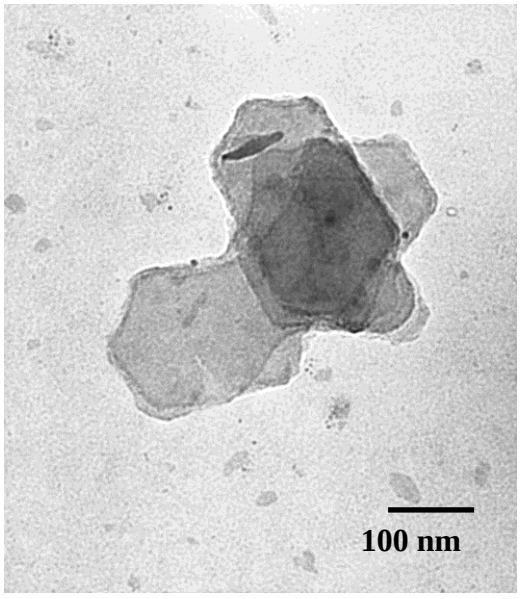

Figure 5.62: TEM image of oxalate intercalated hydrotalcite prepared by re-co-precipitation at a magnification of 415 kx

Figure 5.63 shows the layers inside one of the crystals at a size of 20 nm and calculations show that the average size of the layers is around 0.47 nm, which is consistent with the basil spacing of the hydrotalcite (which is around 0.45 nm).

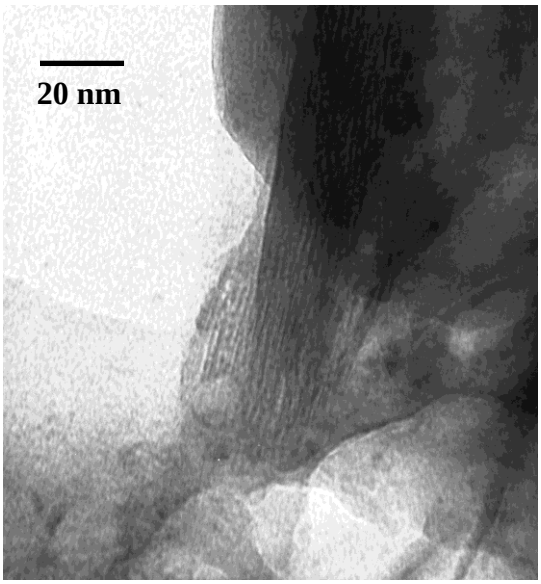

Figure 5.63: TEM image of oxalate intercalated hydrotalcite prepared by re-co-precipitation at a magnification of 540 kx

5.7 HYDROTALCITE RE-CO-PRECIPITATED IN SYNTHETIC BAYER LIQUOR

In order to test the theory that hydrotalcite dissolved in acid could be reformed in synthetic Bayer liquor to adsorb oxalate, a sample of 100 g of hydrotalcite was dissolved in the minimum amount of concentrated nitric acid possible. The dissolved hydrotalcite was added to a synthetic Bayer liquor of the same composition as the adsorption experiments and allowed to settle overnight before it was filtered.

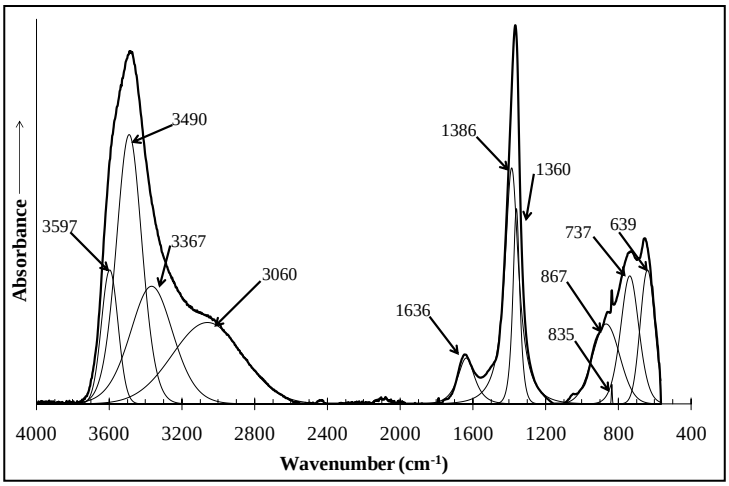

Figure 5.64: Infrared spectrum of hydrotalcite reformed in synthetic Bayer liquor

An infrared spectrum of the filtered and dried hydrotalcite was then recorded. From the infrared spectrum recorded below, it is clear that the material is a typical hydrotalcite that has intercalated carbonate rather than oxalate. This can be shown by the peaks at 1360 cm^{-1}, 1386 cm^{-1} and 835 cm^{-1}. The last two peaks most likely being due to the presence of free carbonate on the sample surface.

This experiment shows that the reformation of dissolved hydrotalcite into synthetic Bayer liquor will not result in the intercalation or adsorption of oxalate into the material and further research into this area was not undertaken.

5.8 MATERIALS PREPARATION AND CHARACTERISATION

5.8.1 XRD ANALYSIS

An analysis of the X-ray diffraction patterns (**Figure 5.65**) reveals that there is little change in the 003 peak positions for the hydrotalcite and oxalate intercalated hydrotalcites. However, there is a change of the 003 peak position from 11.15 °2θ to around 13.3 °2θ with thermal treatment.

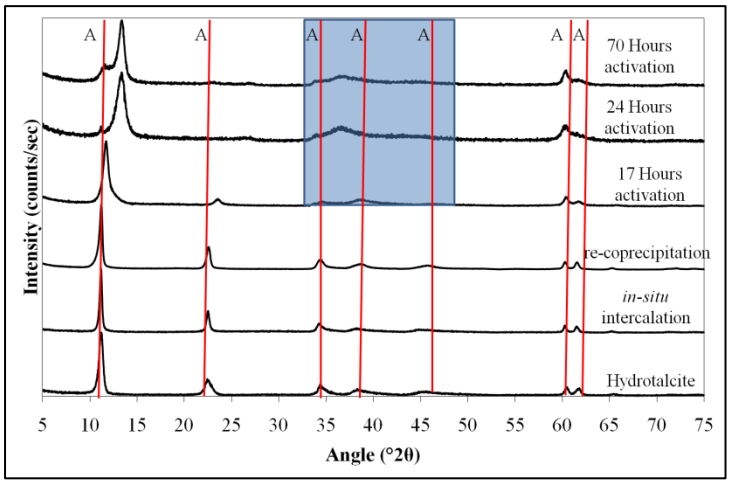

Figure 5.65: XRD comparison of hydrotalcite, oxalate intercalated hydrotalcite and thermally activated hydrotalcites

The thermal treatment XRD patterns show that there is little shift in the 003 peak between the precursor hydrotalcite and the sample that had been treated for 17 hours. This is suggestive that dehydroxylation had not significantly advanced in this time. However, between 17 and 24 hours of thermal treatment, there is a significant shift in the 003 peak position from 11 to 13 °2θ, which is suggestive of dehydroxylation occurring, resulting in a collapse of the interlayer space.

Further evidence of decomposition of the hydrotalcite with thermal treatment is shown by either the loss of, or change in shape of the typical hydrotalcite peaks shown in **Figure 5.65** as the vertical lines labelled A. There is also evidence of metal oxides forming with thermal treatment shown in the region shaded blue. However, it is difficult to determine what these metal oxides are due to band overlap and poor peak intensity, which is suggestive of very small crystallites (due to the peak broadening).

Hydrotalcites

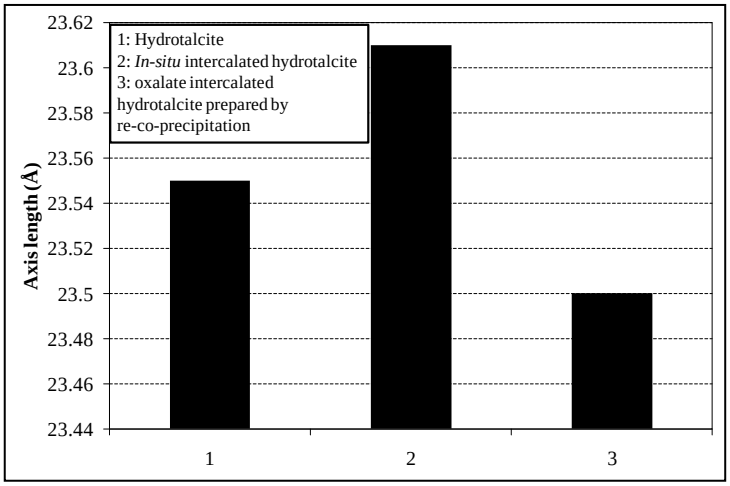

Figure 5.66: C-axis cell parameters for oxalate intercalated hydrotalcites and hydrotalcite

The oxalate intercalated hydrotalcites are interesting in that there is no major shift of the 003 peak when compared to the precursor hydrotalcite. When a Reitveld refinement was performed on these samples, the unit cell parameters where shown to be similar (see **Figure 5.66**) with the difference in the c-axis parameter most likely being caused by differing levels of interlayer hydration between the samples. Further evidence of varying hydration of the samples was shown in the TGA analysis of the materials, which showed that the *in-situ* oxalate intercalated hydrotalcite and the precursor hydrotalcite had significant hydration, while the re-co-precipitated hydrotalcite was not as highly hydrated.

Orientation of the oxalate anions

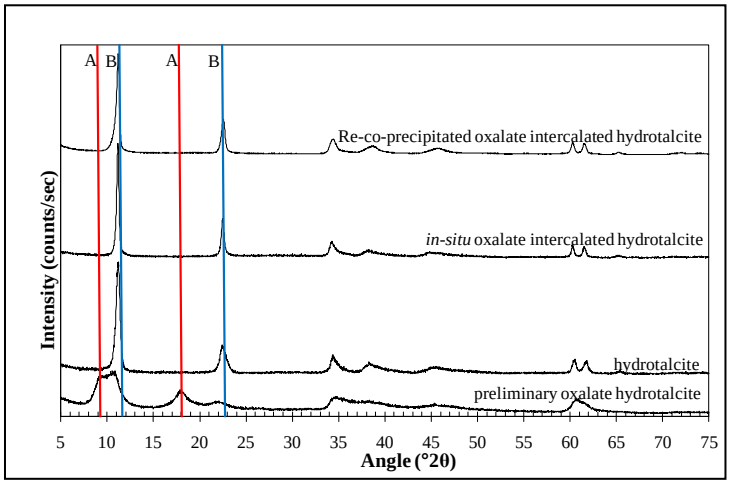

Figure 5.67: XRD comparison of oxalate intercalated hydrotalcites

The intercalation of oxalate into hydrotalcite in a preliminary study gave an XRD pattern which showed a movement of the 003 hydrotalcite peak by approximately 2 °2θ towards lower angle, which is indicative of a larger d-spacing and is a result similar to that which was shown in previous work [3, 70, 126]. The 003 and 006 peaks of this material have been highlighted by the lines marked A in the figure (**Figure 5.67**) above and correspond to the intercalation of oxalate across the interlayer spaces, as can be seen in the representative **Figure 5.68**, which shows a simplified hydrotalcite layered structure with the oxalate anions intercalated into the material.

The carbonate hydrotalcites all showed a similar d-spacing, with slight movement of the peak being determined by the amount of hydration in the interlayer space. The representative 003 and 006 peaks for a carbonate hydrotalcite have been highlighted with lines marked as B in **Figure 5.67**.

Despite the use of two different synthesis methods, the intercalation of oxalate into the hydrotalcite structure showed a similar diffraction pattern to the carbonate hydrotalcite (see **Figure 5.67**, representation **Figure 5.69**), which lead to suspicion that oxalate had not been incorporated into the structure. This was disproved using vibrational spectroscopy and TGA. The has lead to the hypothesis that the oxalate intercalated into the hydrotalcite is orientated along the interlayer space rather than across it, and this is shown in representative **Figure 5.70**.

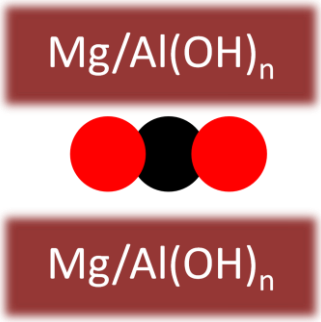

Figure 5.68: Representation of carbonate within the interlayer space of hydrotalcite

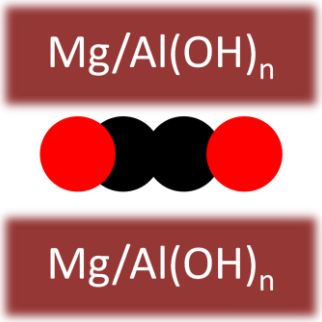

Figure 5.69: Representation of an oxalate intercalated hydrotalcite with oxalate orientated along the interlayer space

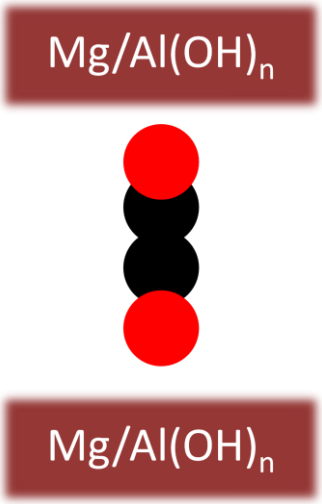

Figure 5.70 Representation of an oxalate intercalated hydrotalcite with oxalate orientated along the interlayer space

Thermally activated hydrotalcites

A Reitveld refinement of the thermally activated hydrotalcites shows that there was a significant change in the composition of the material between 17 and 24 hours of hydration, with almost complete loss of the hydrotalcite structure between 17 and 24 hours of thermal treatment. This is supported by the XRD patterns (**Figure 5.65**) which shows that the layer structure has collapsed significantly between 17 and 24 hours by the movement of the peak to around 13 °2θ. The presence of hydrotalcite after both 24 and 70 hours of treatment is most likely due to the reformation of hydrotalcite upon contact with carbon dioxide and water vapours in the atmosphere.

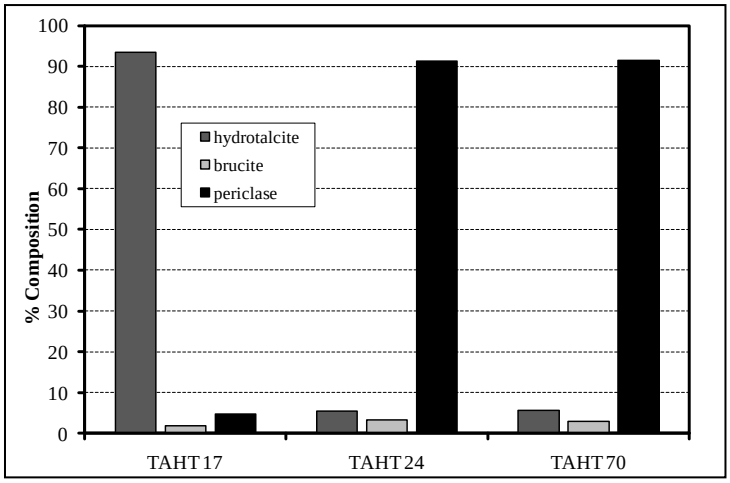

Figure 5.71: Phase composition of thermally activated hydrotalcites

The 70 hour thermally treated material has a similar phase composition to the 24 hour treated material (see **Figure 5.71**). However, there is a difference in surface area (see **Section 5.8.4**) which is most likely a change in morphology over thermal treatment time. The presence of around 5 % hydrotalcite in each sample is most likely due to atmospheric contact during sample handling, which is a good indicator that the thermal treatment of the hydrotalcite does not result in a permanent change.

5.8.2 IR ANALYSIS

Infrared analysis of the various hydrotalcites can be seen in the **Figure 5.72**, which shows some interesting bands, which have been highlighted and labelled.

The first of the interesting regions is in the hydroxyl stretching region of the spectra (3000 cm^{-1} to 4000 cm^{-1}), which shows considerable changes in the Mg_3-OH stretch (band A) between the precursor hydrotalcite and the oxalate intercalated hydrotalcites.

Furthermore, there is a significant change to the Mg_2Al-OH stretch (band B), which is more prominent in the oxalate intercalated hydrotalcites than the precursor hydrotalcite; while the $MgAl_2$-OH band (band C) is most prominent in the precursor hydrotalcite rather than the oxalate intercalated hydrotalcites. This is suggestive that the inclusion of oxalate into the interlayer spaces has modified the order of the metal ions in the metal-hydroxide sheets.

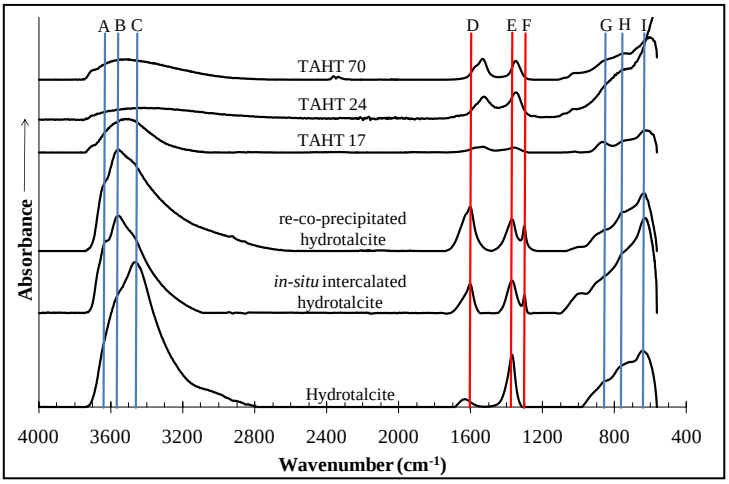

Figure 5.72: Infrared comparison of hydrotalcite, thermally activated hydrotalcites and oxalate intercalated hydrotalcites

In the thermally activated hydrotalcites, the hydroxyl stretching bands have significantly decreased which is expected with thermal treatment. The bands have overlapped enough that it is difficult to distinguish the individual bands from each other. There is also evidence of a new band appearing around 3700 cm^{-1}, which is most likely a Mg-OH band caused by the migration of protons through the metal-hydroxide layers.

The C-O bands in the region of 1200 cm^{-1} to 1600 cm^{-1} also show some interesting features. The oxalate intercalated hydrotalcites two extra C-O bands (bands D and F) in addition to the υ_3 carbonate band (band E). All three of these hydrotalcites also show water bands around 1550 cm^{-1} to 1600 cm^{-1}, which are lower than expected due to the effect of oxalate anions (which are not marked here). There is also evidence of extra C-O bands in the thermally activated hydrotalcites, with bands appearing around 1500 cm^{-1}. This is suggestive of the carbonate becoming integrated into the metal-hydroxide layers due to thermal treatment.

In the fingerprint region of the spectrum (less than 1000 cm^{-1}) there are three bands of interest. These are the υ_2 carbonate band around 877 cm^{-1} (band G); the M-OH translation around 733 cm^{-1} (band H) and the M-O Stretching band around 634 cm^{-1} (band I).

In the oxalate intercalated hydrotalcites, the fingerprint region of the spectrum is similar to the precursor hydrotalcite, which is what could be expected as the materials are very similar, although there is evidence that the bands have been shifted to slightly lower wavenumbers. The *in-situ* intercalated hydrotalcite shows an extra C-O band at 1014 cm^{-1} (which is not shown here).

The thermally activated hydrotalcites show considerable differences to the M-OH bands (bands G and H) which are decreased in all three thermally activated hydrotalcites. The major difference in the thermally activated hydrotalcites is in the sample that had been treated for 24 hours (TAHT 24), which has an M-O stretch that is significantly higher than the other samples and is suggestive of the material undergoing significant structural changes. This is supported by the BET analysis of the material.

5.8.3 RAMAN ANALYSIS

A comparison of the Raman spectra for all of the samples shows some interesting features and can be seen below (**Figure 5.73**). There have been a number of changes to the materials with thermal treatment and the insertion of oxalate into the material.

Thermally activated hydrotalcites

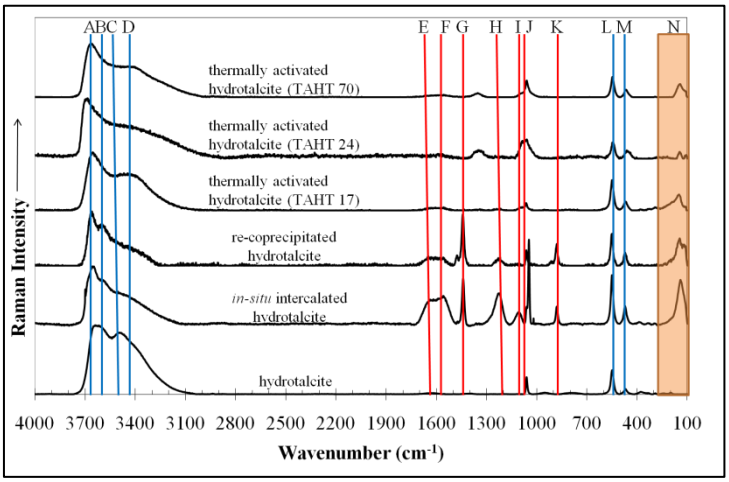

Figure 5.73: Raman spectral comparison of hydrotalcite, oxalate intercalated hydrotalcites and thermally activated hydrotalcites

There are some interesting changes (and some constant features) when it comes to the Raman spectra of the thermally activated hydrotalcites. With the M-O-M linking bands at 470 cm^{-1} (band M) and the M-OH stretching modes around 549 cm^{-1} (band L) there has been little change between the bands except for some peak broadening with thermal treatment.

The presence of carbonate (1060 cm^{-1}, band J) in the samples was also detected in the 24 and 70 hour treated samples, although this is most likely due to some reformation of the hydrotalcite precursor material upon atmospheric contact during handling. There is also some evidence of hydrogen bonded water appearing in the samples due to the peaks in the region below 300 cm^{-1} (shown as region N).

By far, the biggest area of change in the samples was within the metal-hydroxide stretching region (3000 cm^{-1} to 4000 cm^{-1}) where there were some changes to the Mg-OH stretch around 3660 cm^{-1} (band A), the Al-OH stretch around 3609 cm^{-1} (band B), the Al_3-OH stretch around 3498 cm^{-1} (band C) and the $MgAl_2$-OH stretch 3389 cm^{-1} (band D).

Band C, the Al_3-OH stretch shows a big decrease upon thermal treatment, with the samples treated for longer showing the greatest decrease in intensity for that band. There is also an increase in the intensity for band D, which is the $MgAl_2$-OH stretch, which is suggestive of some reorientation of the atoms within the structure as the material decomposes. The Mg-OH stretch (band A) at 3660 cm^{-1} has become better defined and has maintained intensity throughout the thermal treatment process, which is a strong indication of no major changes to Mg-OH bonding within the samples, which would be consistent with the formation of brucite. The metal-hydroxide stretching region has also broadened at lower wavenumbers, which is suggestive of an Mg_2Al-OH band becoming more intense and broadening (although it is not shown in **Figure 5.73**).

Oxalate intercalated hydrotalcites

The oxalate intercalated hydrotalcites show some interesting changes in the hydroxide stretching region (3000 cm^{-1} to 4000 cm^{-1}), mostly with decreases in intensity for the Al_3-OH (band C) and $MgAl_2$-OH (band D) stretches, which indicates that the inclusion of oxalate has changed the bonding between the metal ions in the brucite-like sheets.

There have also been some changes in the region between 1000 cm^{-1} and 1500 cm^{-1}, where a number of new carbon-oxygen bonds appear in positions around 1550 cm^{-1} (band G), 1440 cm^{-1} (band H), 1220 cm^{-1} (band I), 1060 cm-1 (band J) and 880 cm^{-1} (band K). Apart from the C-O band around 1060 cm^{-1} (band J), which is present in the precursor hydrotalcite and can be linked to carbonate, the other bands (bands G, H, I and K) are unique to the presence of the oxalate anions within the sample.

The two oxalate intercalated hydrotalcites also show clear evidence of interlayer water molecules being present through the two bands centred around 1600 cm^{-1} (bands E and F). The much higher intensity of the two water bending modes (bands E and F) for the *in-situ* oxalate intercalated hydrotalcite is suggestive of a higher level hydration within that sample, which is supported by the TGA data for the two samples.

5.8.4 NITROGEN ADSORPTION/DESORPTION ANALYSIS

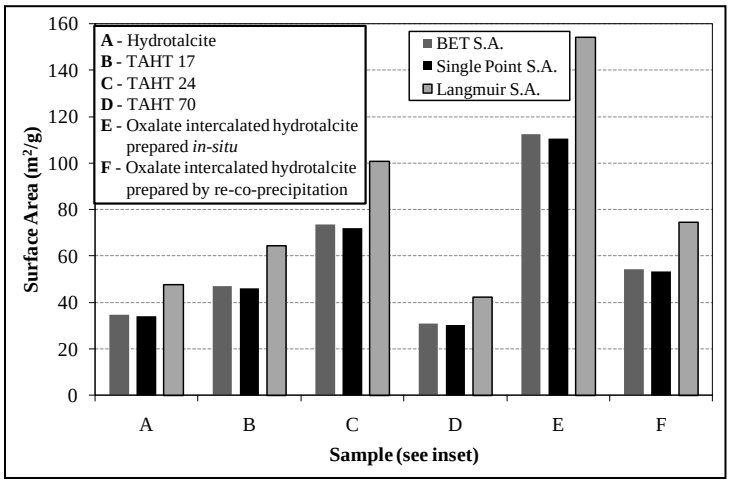

Figure 5.74: Surface area comparison of hydrotalcites, thermally activated hydrotalcites and oxalate intercalated hydrotalcites

A comparison of the surface area of the various hydrotalcite materials (**Figure 5.74**) shows that the oxalate intercalated hydrotalcites have a larger surface area than the precursor hydrotalcite. This is expected due to the larger size of the oxalate anion when compared to the carbonate anion. The *in-situ* intercalated hydrotalcite has a higher surface area than the re-co-precipitated hydrotalcite, which is also suggestive of some oxalate being adsorbed onto the surface of the material.

The thermally activated hydrotalcites show an increase in surface area when compared to the precursor hydrotalcite for up to 24 hours of treatment, while the 70 hour thermally treated sample shows a decreased surface area when compared to the precursor material. This suggests that the 24 hour thermally treated samples would make better adsorbents than materials treated for 70 hours at 280 °C.

Chapter 6: Results and Discussion: Adsorption Studies

6.1 CHEMISTRY AT THE HYDROTALCITE SURFACE

6.1.1 HYDROTALCITE STRUCTURE

Hydrotalcite has a unit cell that conforms to the rhombahedral $R\bar{3}m$ space group which group together to form hexagonal crystallites, such as those seen in **Figure 6.1**. This structure is similar to the brucite ($Mg(OH)_2$) crystal structure; however some of the magnesium atoms in the structure are dislocated by aluminium to give a net positive charge for the metal hydroxide sheets.

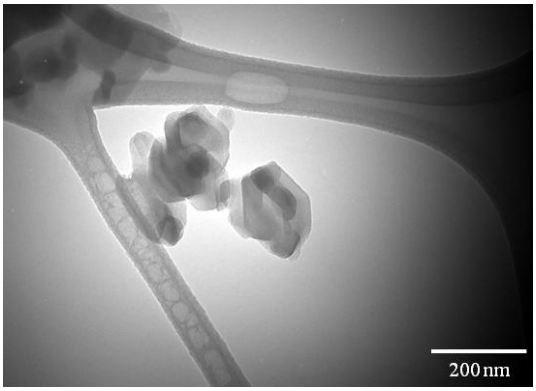

Figure 6.1: TEM image of hydrotalcite precursor material at 120 kx magnification

STRUCTURE ON THE FACE OF THE CRYSTALS

The distribution of adsorption sites across the face of the hydrotalcite crystal is going to be a regular, repeating pattern across the hexagonal face, as determined by Sideris *et al.* [59] by multinuclear NMR. This regular distribution of adsorption sites results in an evenly distributed positive charge across the layers allowing for the formation of a regular adsorption surface and adsorption sites with a uniform distribution. This can be seen in **Figure 6.2** below, which shows the ordered arrangement of the aluminium cation disorders in the hydrotalcite structure which forms the basis for a regular, repeating pattern of hexagons similar to that of honeycomb (red hexagon).

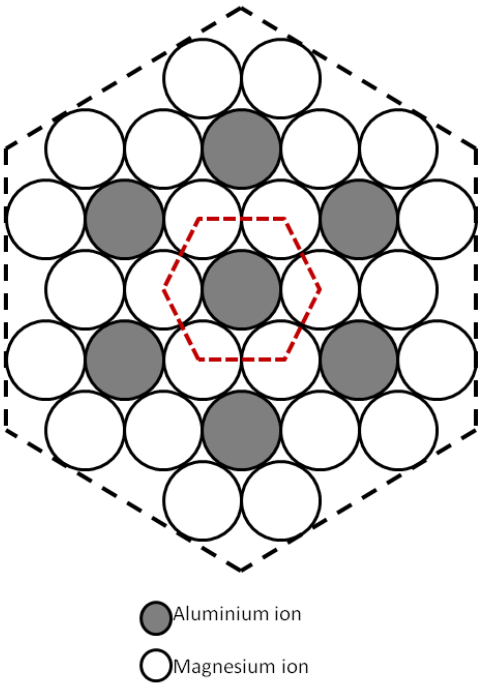

Figure 6.2: Diagram showing cation ordering in hydrotalcite

STRUCTURE OF THE CRYSTAL EDGES

The hydrotalcite structure at the edge of the crystals is significantly different and has an impact on the availability of adsorption sites. The electrostatic interactions between hydroxide groups bonded to the metal atoms results in hydroxide groups hanging off of the edge of the crystal. This in turn leads to hydroxide groups to be hanging off the edge of the crystal into empty space and results in a partial negative charge at the edge of the crystal.

IMPLICATIONS FOR ADSORPTION

When the crystal structure of hydrotalcite is considered there are some significant implications for adsorption. This first consideration is the uniform distribution of aluminium dislocations throughout the surface. This uniform distribution of aluminium atoms results in a uniform distribution of adsorption sites.

6.1.2 ADSORPTION AT THE HYDROTALCITE SURFACE

SORBATE ORIENTATION

When considering surface area calculations using the adsorption data $(S = q_e N\Omega)$ (**Equation 3.5**), sorbate orientation is an important consideration. With oxalate anions, there are three possible orientations in which they can be adsorbed. The first orientation is for the oxalate to be lying flat along the hydrotalcite surface, as shown in **Figure 6.3**.

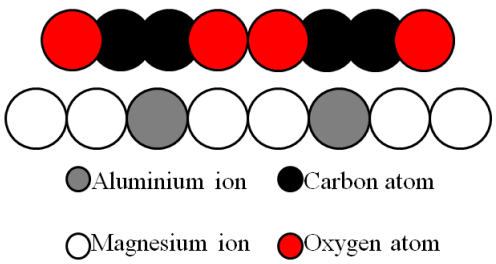

Figure 6.3: Diagram depicting oxalate adsorbed on hydrotalcite lying flat

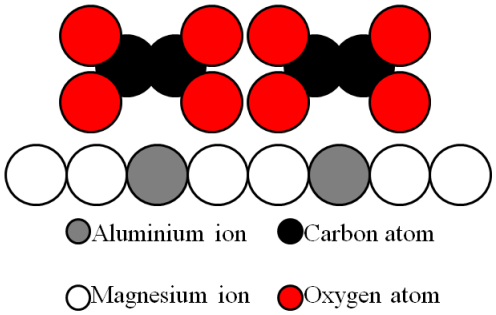

Figure 6.4: Diagram representing oxalate adsorbed to hydrotalcite lying on its side

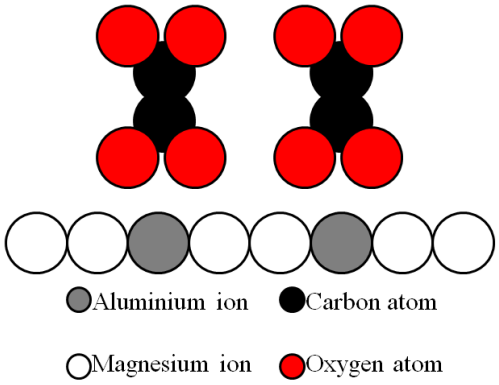

Figure 6.5: Diagram representing oxalate adsorbed to the surface of hydrotalcite in a "standing" orientation

This orientation is going to give the largest possible surface area when the surface area is calculated. The second possible orientation is for the oxalate anions to be lying on their sides along the surface of the hydrotalcite (**Figure 6.4**) while the third possible orientation is for the oxalate anions to be standing upright at the surface of the material (**Figure 6.5**), which gives the smallest possible surface area.

When considering the likely orientation that oxalate is most likely to take during orientation, it was considered to be most appropriate to consider the orientation that would give the largest possible surface area, the oxalate anions lying flat along the hydrotalcite surface. This is based upon the assumption that laying the oxalate anions flat does not mask any adsorption sites.

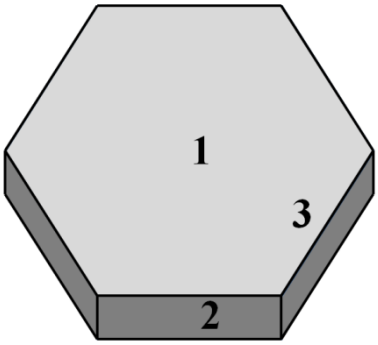

Figure 6.6: 3D representation of a hydrotalcite crystal highlighting possible adsorption areas

In reality, all three orientations are going to be represented although a random orientation is unlikely. The more likely scenario is that all three orientations are going to be represented given the following considerations:

1. On the hexagonal surface of the hydrotalcite (area 1 on **Figure 6.6**), the oxalate anions are most likely to be orientated so that they are standing up (**Figure 6.5**), with the second negative charge being cancelled by sodium ions.
2. On the edge of the hydrotalcite crystal (area 2 on **Figure 6.6**), there is likely to be no adsorption at all due to negative hydroxyl groups hanging into space.
3. On the surface of the hydrotalcite crystals near the edge (area 3 on **Figure 6.6**), the orientation of the oxalate anions is most likely to be a combination of oxalate lying flat or on its side (**Figure 6.3** and **Figure 6.4**).

SOLUTION PH

There has been substantial debate on what effect solution pH has on adsorption capacity, however Goh, Lim and Dong [90] suggest that adsorption capacity generally deacreases as the solution pH increases. This is an effect caused by competitive adsorption of hydroxide anions onto the positive surface of the hydrotalcite.

At the point of zero charge (pzc) the surface charge of the hydrotalcite is cancelled out by the hydroxide ions binding to and smothering the charged areas, resulting in no adsorption. Although the pzc varies for different hydrotalcites, the pzc of hydrotalcite is generally accepted to be around pH 12 for an Mg/Al ratio of 3:1 [127]. For this reason, the pH of the adsorption solutions becomes a factor. For solutions with a higher pH, the adsorption capacity of hydrotalcite is likely to decrease as they hydroxide concentration increases and provides more competition to the sorbate anions for adsorption sites.

6.2 HYDROTALCITE ADSORPTION STUDIES

6.2.1 OXALATE ADSORPTION ONTO HYDROTALCITE

The oxalate adsorption studies showed a couple of interesting points. The plot of q_e vs. c_e (see **Figure 6.7**) shows a gradual increase in adsorption. The Langmuir adsorption isotherm shows the first anomaly, as it is curved and impossible to determine a reasonable fit (**Figure 6.8**). This was seen as a clear indication that the adsorption of oxalate by hydrotalcite definitely is not driven by an equilibrium process and that adsorption sites are not equivalent [72, 74, 83-85].

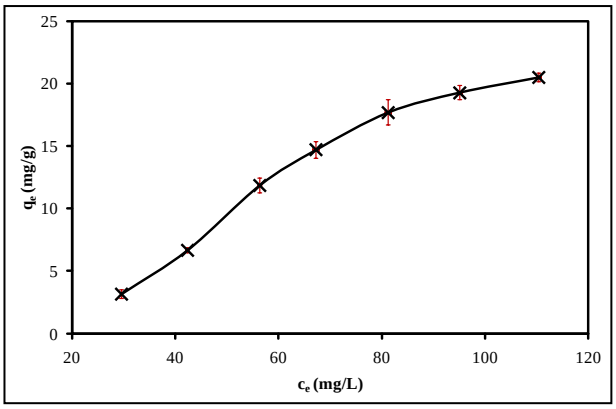

Figure 6.7: Plot of q_e vs. c_e for the adsorption of oxalate by hydrotalcite

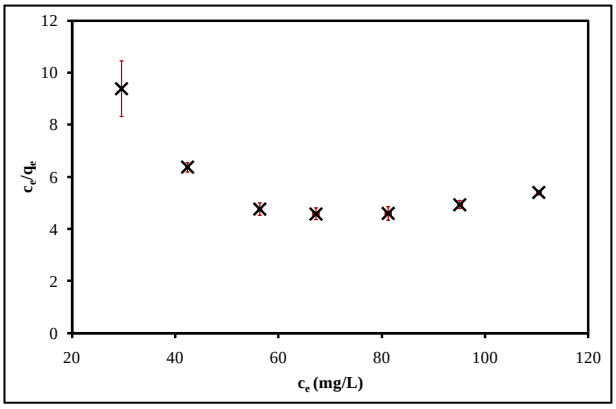

Figure 6.8: Langmuir adsorption isotherm for the adsorption of oxalate by hydrotalcite

The application of the Freundlich adsorption isotherm to the data (**Figure 6.9**) shows a good fit (R^2 = 0.9421) and is a clear indication that the adsorption of oxalate onto the surface of hydrotalcite is a concentration driven process [74, 80, 81] and that there is a distribution of energy levels for the adsorption sites.

It was possible to use the Freundlich model to calculate the Freundlich adsorption constant (k_F), which was determined to be 1.52 ± 0.08 and also to determine the adsorption intensity (1/n) which was calculated to be 1.43 ± 0.08 and is indicative of homogeneous adsorption and indicative of the adsorption sites being energetically equivalent.

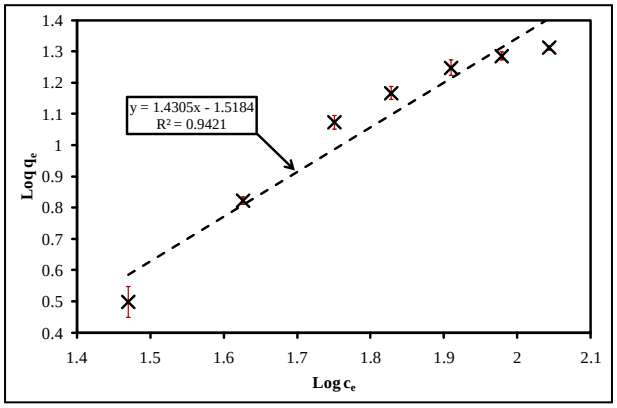

Figure 6.9: Freundlich adsorption isotherm for the adsorption of oxalate by hydrotalcite

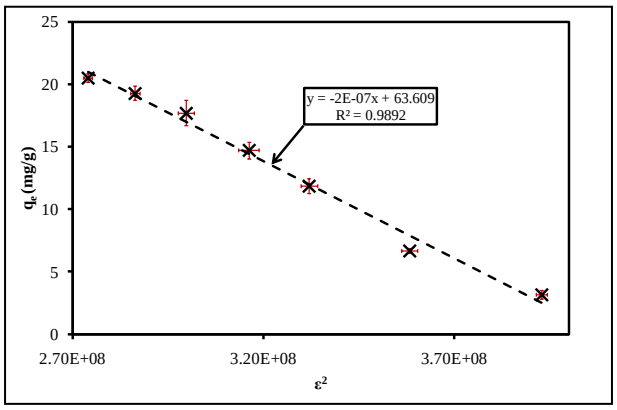

Figure 6.10: Polyani plot for the adsorption of oxalate by hydrotalcite

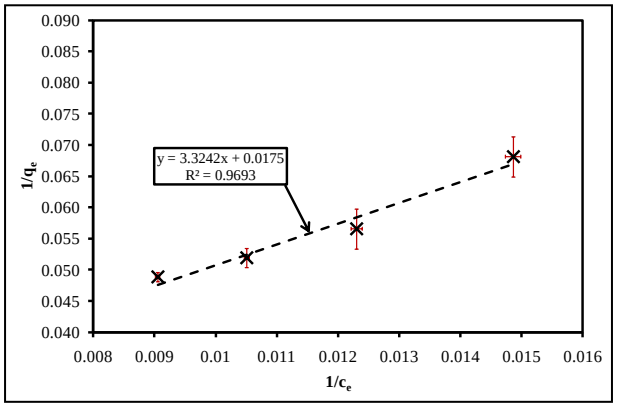

Figure 6.11: Plot of $1/q_e$ vs. $1/c_e$ for the adsorption of oxalate by hydrotalcite

It was possible to calculate the adsorption capacity using the Polyani potential plot (**Figure 6.10**) which had a strong correlation factor (R^2 = 0.9892) and gave a theoretical adsorption capacity of 63.6 ± 0.7 mg/g. The adsorption energy was also calculated from the D-R isotherm to be 3.82 ± 0.04 kJ/mol, which indicates that the adsorption of oxalate by hydrotalcite is a physical rather than a chemical process [88, 89]. This indicates that the oxalate anions are very weakly bound to the surface of the hydrotalcite.

When the adsorption data for the equilibrium concentrations above 60 mg/L are fitted to the Langmuir model, it is possible to use them to determine the theoretical adsorption capacity using the plot of $1/q_e$ vs. $1/c_e$, (**Figure 6.11**) which has a good correlation coefficient (R^2 = 0.9693) and gives a calculated theoretical adsorption capacity of 57 ± 2 mg/g.

From the theoretical adsorption data (using the Polyani potential calculations) it was possible to determine the active surface area of the hydrotalcite using **Equation 3.5**, which was calculated to be 101 ± 1 m^2/g

6.2.2 CARBONATE ADSORPTION ONTO HYDROTALCITE

The use of fully included hydrotalcite (hydrotalcite that has carbonate in the interlayer spaces) for the adsorption of carbonate was also examined (**Figure 6.12**). The initial data showed that there was an anomalous result around 80 ppm carbonate equilibrium concentration (c_e), resulting in that particular data point being removed as an outlier and the models being fitted accordingly.

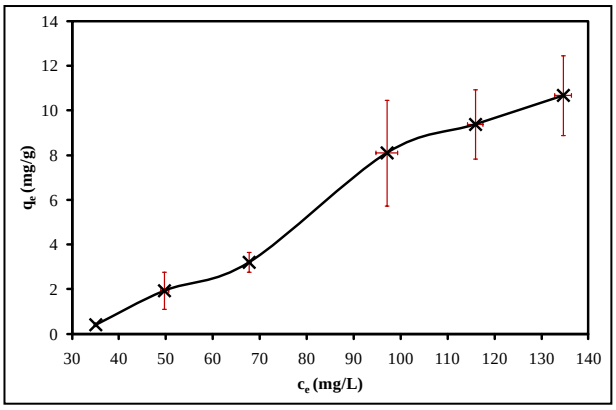

Figure 6.12: Plot of q_e vs. c_e for the adsorption of carbonate by hydrotalcite

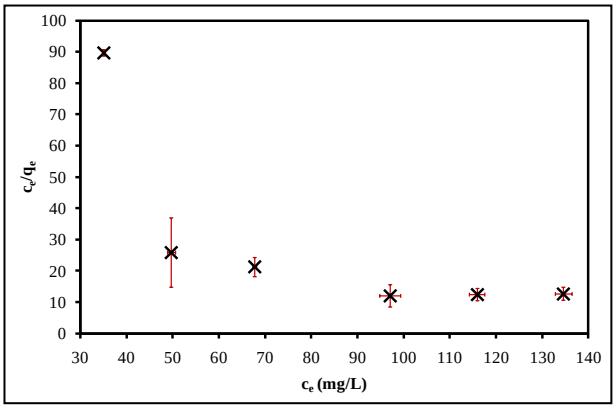

Figure 6.13: Langmuir adsorption isotherm for the adsorption of carbonate by hydrotalcite

The Langmuir adsorption isotherm (see **Figure 6.13**) is similar in nature to the oxalate adsorption data (**Figure 6.8**) in that there is no fit to a linear trend. This is a clear indication that in this case, the adsorption sites are not energetically equivalent and other models, such as the Freundlich adsorption model need to be considered.

The Freundlich adsorption isotherm (see **Figure 6.14**) shows a good fit to a linear trend (R^2 = 0.9452). (The apparent curvature of the plot is a common artefact of the treatment of the data [74, 80, 81, 85]). From the fit of the Freundlich adsorption model, the Freundlich constant was calculated to be -3.9 ± 0.2 and the adsorption intensity was determined to be 2.4 ± 0.1, which is again indicative of homogeneous adsorption, which means that there is essentially no energy distribution of adsorption sites.

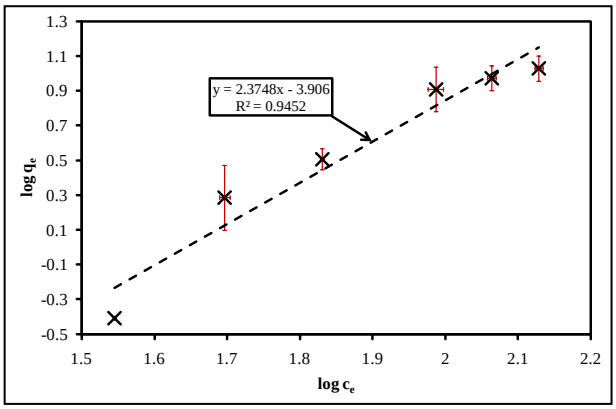

Figure 6.14: Freundlich adsorption isotherm for the adsorption of carbonate by hydrotalcite

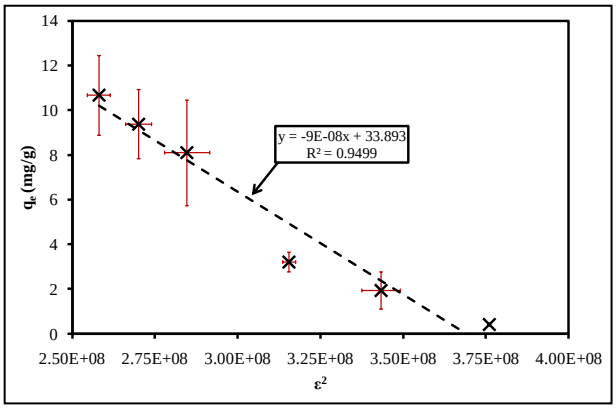

Figure 6.15: Polyani plot for the adsorption of carbonate by hydrotalcite

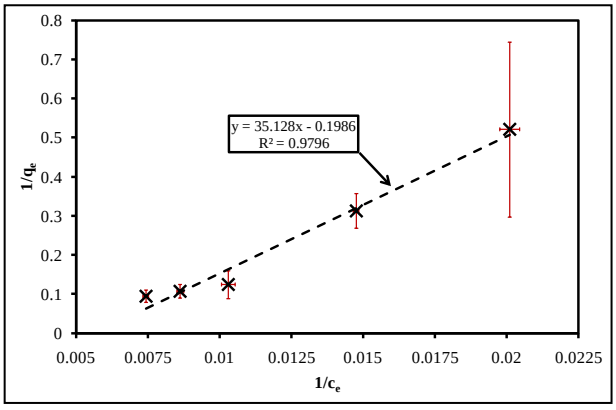

Figure 6.16: Plot of $1/q_e$ vs. $1/c_e$ for the adsorption of carbonate by hydrotalcite

The Polyani plot was used to calculate the adsorption capacity (**Figure 6.15**) and the plot showed a good correlation to a linear trend (R^2 = 0.9499) and gave a theoretical maximum adsorption capacity of 34 ± 2 mg/g. Although there was a good fit of a linear trend to the plot of $1/q_e$ vs. $1/c_e$, (see **Figure 6.16**, R^2 = 0.9796) the intercept was negative and the theoretical adsorption capacity was calculated to be -5.0±0.1 mg/g. This is most likely due to the plot of $1/q_e$ vs. $1/c_e$ being related to the Langmuir adsorption isotherm. Due to the non-fit of the Langmuir model, the theoretical maximum adsorption capacity of -5.0 mg/g can be disregarded.

The active surface area was calculated from the theoretical maximum adsorption capacity calculated by the Polyani plot and it was determined to be 44 ± 2 m^2/g using **Equation 3.5** and a cross sectional area of 1.9×10^{-19} m^2 for carbonate. The Polyani plot was also used to determine the energy of adsorption, which was found to be 2.6 ± 0.1 kJ/mol, which is clearly indicative of physiosorption being the dominant process, which suggests that carbonate anions are loosely adsorbed to the surface.

6.2.3 ADSORPTION FROM MIXED OXALATE/CARBONATE SOLUTIONS ONTO HYDROTALCITE

The use of hydrotalcite as an adsorbent for mixed oxalate/carbonate solutions (such as a Bayer liquor) is a novel application for adsorption. The combined plot of q_e vs. c_e (**Figure 6.17**) shows that the adsorption of a mixed oxalate/carbonate solution is complex. The first point of interest that it shows is that the adsorption of oxalate slowly increases as the overall solution concentration increases. The second thing that it shows is that the initial adsorption of carbonate (and consequently overall adsorption) is not consistent until around 220 mg/L, after which the adsorption rapidly increases. An examination of the error (standard error, represented by red bars) of these points shows that it is possible that for the concentrations under 220 mg/L that the adsorption may be consistent.

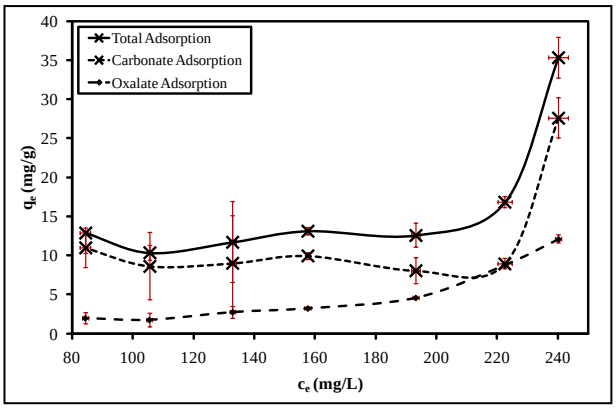

Figure 6.17: Plot of q_e vs. c_e for hydrotalcite adsorption from a combined oxalate/carbonate solution

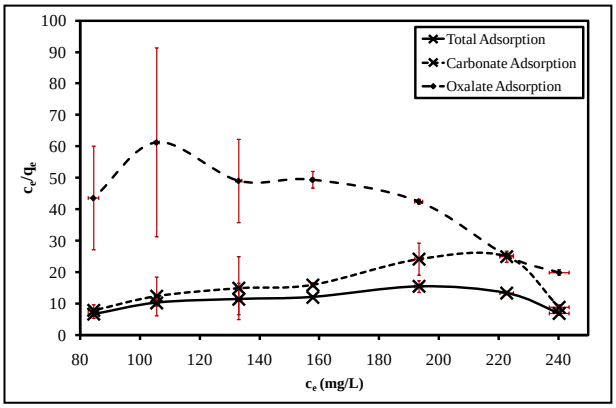

Figure 6.18: Langmuir adsorption isotherm for hydrotalcite from a combined oxalate/carbonate solution

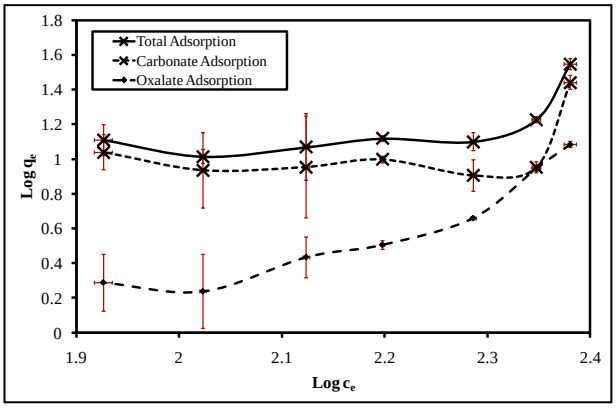

Figure 6.19: Freundlich adsorption isotherm for hydrotalcite from a mixed oxalate/carbonate solution

The combined Langmuir isotherm (**Figure 6.18**) shows that the oxalate adsorption is not likely to fit the Langmuir adsorption model unless the point around 80 mg/L is disregarded. It also suggests that the carbonate and overall adsorption isotherms show a possible fit to the Langmuir adsorption model.

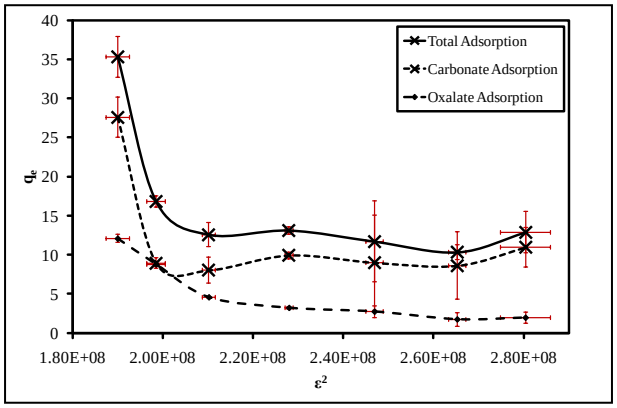

Figure 6.20: Polyani plot for hydrotalcite adsorption from a mixed oxalate/carbonate solution

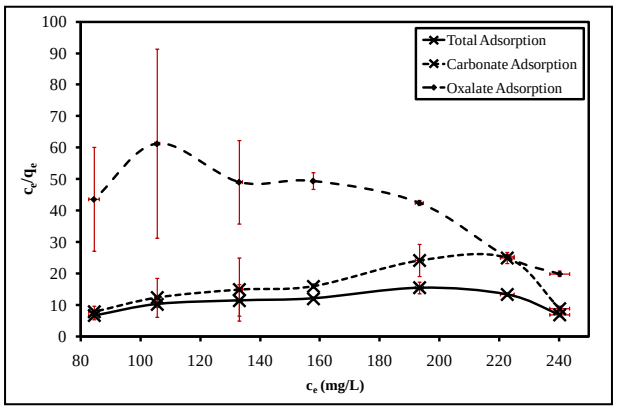

Figure 6.21: Combined plot of 1/qe vs. 1/ce for hydrotalcite adsorption from a mixed oxalate/carbonate solution

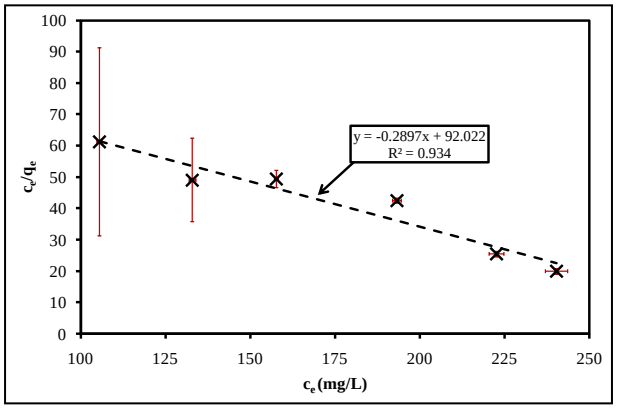

Figure 6.22: Langmuir adsorption isotherm for the adsorption of oxalate from an oxalate/carbonate mixture by hydrotalcite

The combined Freundlich isotherm (**Figure 6.19**) shows that once again, with the exception of the point at lowest concentration, the oxalate isotherm is likely to have a good fit, while the carbonate and total adsorption isotherms show a distinct "kick" upwards at higher concentrations, making the applicability of the Freundlich adsorption isotherm doubtful in those cases.

The combined Polyani plot (**Figure 6.20**) shows that none of the adsorption plots are very likely to fit, due to their "kick" upwards at higher concentration. Meanwhile, the combined $1/q_e$ vs. $1/c_e$ plot (**Figure 6.21**) shows that the total adsorption and carbonate adsorption are likely to fit a linear trend, while the low concentration point of the oxalate adsorption line appears to be an outlier.

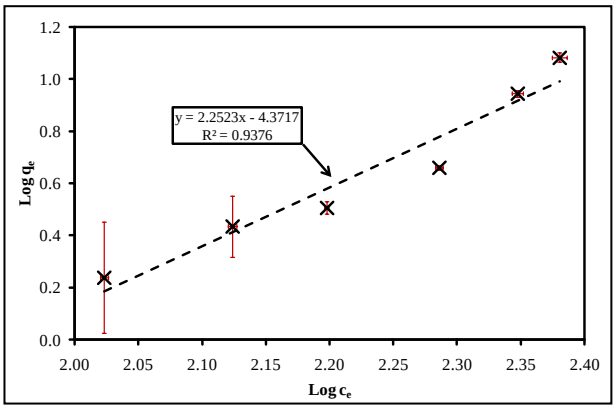

Figure 6.23: Freundlich adsorption isotherm for the adsorption of oxalate from an oxalate/carbonate mixture by hydrotalcite

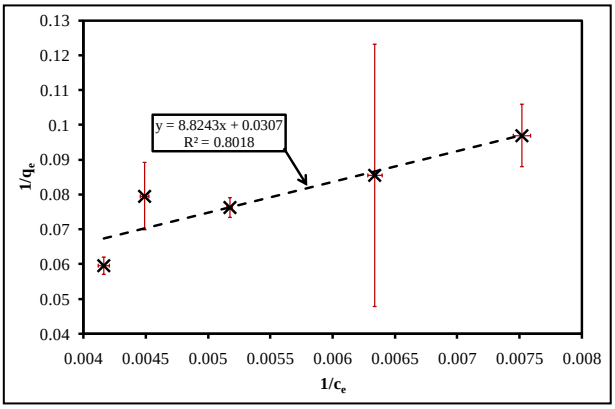

Figure 6.24: Plot of 1/qe vs. 1/ce for the adsorption of oxalate by hydrotalcite from a mixed oxalate/carbonate solution

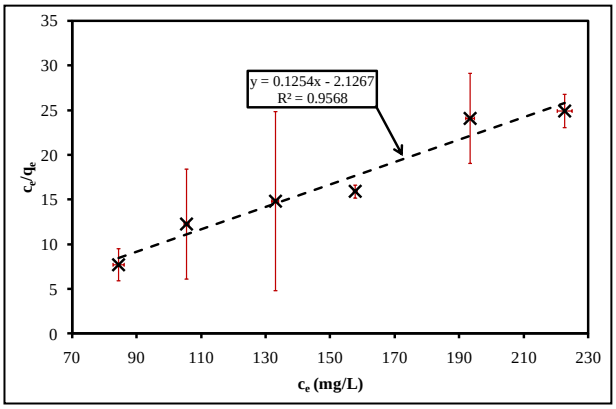

Figure 6.25: Langmuir adsorption isotherm for the adsorption of carbonate by hydrotalcite from an oxalate/carbonate mixture

The application of the Langmuir adsorption isotherm to the oxalate adsorption data (excluding the outlying point at 80 mg/L, see **Figure 6.22**) shows a decreasing trend with a strong correlation to a linear model (R^2 = 0.934). This suggests that the use of the Langmuir adsorption model to explain the adsorption of oxalate in this instance is not applicable and this supports the theory that the Freundlich model is a more applicable explanation of the adsorption of oxalate by hydrotalcite (see **Section 6.2.1**). From the Langmuir adsorption isotherm, it was also possible to calculate the energy of adsorption, which was calculated to be -1.9 ± 0.1 kJ/mol. This value implies that adsorption is an endothermic process in the case of competition from carbonate ions.

When the Freundlich adsorption isotherm is applied to the adsorption data (with the exception of the point at 80 mg/L, see **Figure 6.23**), there is a strong correlation to a linear model (R^2 = 0.9376). The Freundlich adsorption constant (kF) was calculated to be -4.0 ± 0.3 and the adsorption intensity (1/n) was calculated to be 2.3 ± 0.1, which clearly indicates that the adsorption sites have little or no energy distribution.

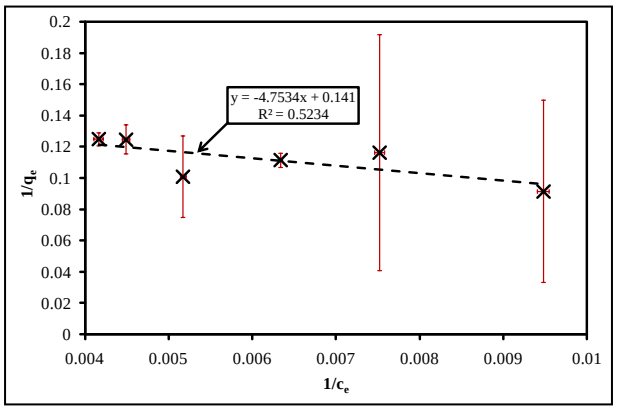

Figure 6.26: Plot of $1/q_e$ vs. $1/c_e$ for the adsorption of carbonate by hydrotalcite from a mixed oxalate/carbonate mixture

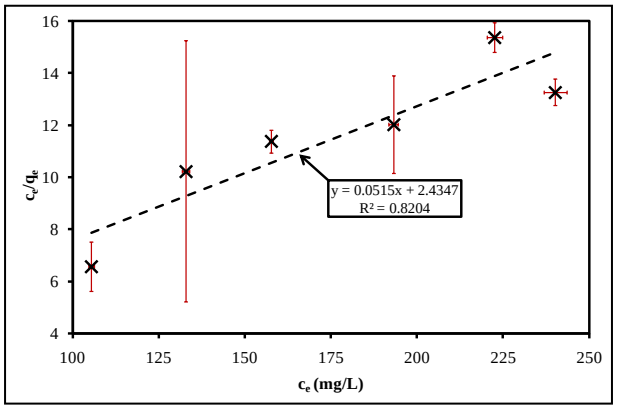

Figure 6.27: Langmuir adsorption isotherm for hydrotalcite adsorption from an oxalate/carbonate mixture

The plot of $1/q_e$ vs. $1/c_e$ for oxalate (**Figure 6.24**), once the outlier was removed showed a very strong correlation (R^2 = 0.9839) to a linear model and allowed the calculation of a theoretical adsorption capacity of 3.61 ± 0.06 mg/g, using the absolute value for the intercept.

For the carbonate adsorption data, there is an outlier around 240 mg/L. Once the outlier is removed, there is a very strong adherence to a linear trend (R^2 = 0.9568) for the Langmuir adsorption isotherm (**Figure 6.25**). This allows for the calculation of the Langmuir constant (k_L), which was determined to be -0.47 ± 0.02 and the energy of adsorption, which was calculated to be -36 ± 2 kJ/mol. This indicates that the adsorption of carbonate onto the hydrotalcite surface is chemisorption rather than a physiosorption and that it is endothermic. This chemisorption is most likely an effect of the presence of oxalate in the adsorption solution. The separation factor (k_R) was also calculated and it was found to be -8.9 ± 0.3 $x10^{-3}$, which suggests that adsorption may be irreversible. There was poor fit to a Freundlich adsorption isotherm (R^2 > 0.5) which is strongly suggestive of Freundlich adsorption not being applicable in this case.

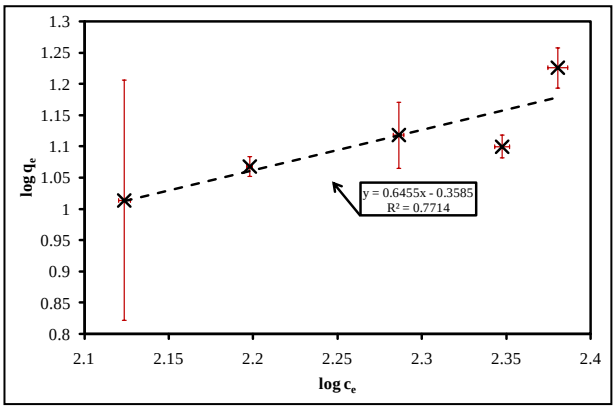

Figure 6.28: Freundlich adsorption isotherm for hydrotalcite adsorption from a mixed oxalate/carbonate solution

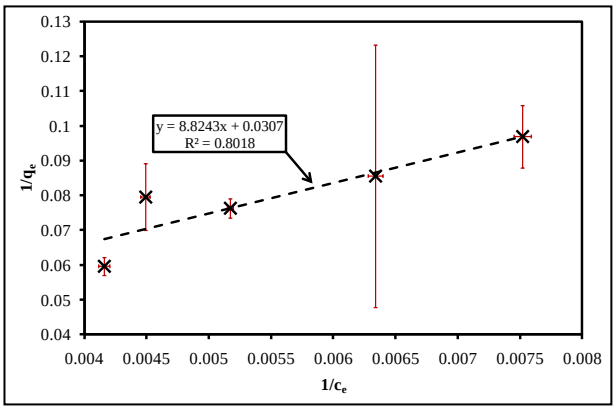

Figure 6.29: Plot of $1/q_e$ vs. $1/c_e$ for total adsorption of hydrotalcite from a mixed oxalate/carbonate solution

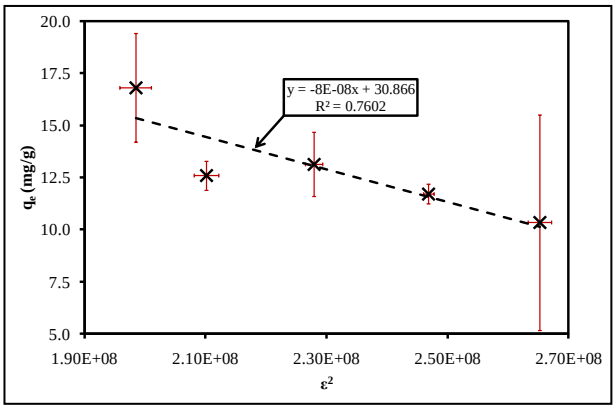

Figure 6.30: Polyani plot for adsorption by hydrotalcite from a mixed oxalate/carbonate mixture

The plot of $1/q_e$ vs. $1/c_e$ (see **Figure 6.26**) for the adsorption of carbonate showed a poor fit to a linear trend (R^2 = 0.5234). However, it allowed for the calculation of a theoretical adsorption capacity of the hydrotalcite, which was calculated to be 7 ± 3 mg/g, which is much lower than was expected. This may be due to a pH effect, which is discussed further below.

For the overall adsorption data, the fitting of the Langmuir (R^2 = 0.8204) and Freundlich (R^2 = 0.7714) adsorption isotherms were, at best, moderate (see **Figure 6.27** and **Figure 6.28**). The fact that these fits are only moderate is most likely due to the oxalate and carbonate adsorptions fitting different adsorption models, with oxalate fitting a Freundlich adsorption model (**Figure 6.23**) while carbonate fits a Langmuir adsorption model (**Figure 6.25**). This is most likely due to a co-adsorption effect of using ions with similar sizes and charge densities, which might result in variation in adsorption behaviour.

It was also possible to calculate the theoretical maximum adsorption study of the hydrotalcite using the plot of $1/q_e$ vs. $1/c_e$ (R^2 = 0.8018, see **Figure 6.29**) which gave a theoretical maximum adsorption capacity of 32.57±6.46 mg/g while the Polyani plot (R^2 = 0.7602, see **Figure 6.30**) gave a theoretical maximum adsorption of 30.87±7.40 mg/g.

6.2.4 EFFECT OF pH ON ADSORPTION

From the theoretical maximum adsorption capacities (see **Table 6.1**), it is clear that the adsorption of oxalate from an oxalate solution is most efficient while the adsorption of carbonate and the overall adsorption from the mixed solution are similar. When considering the pH of the initial adsorption solutions, shown in **Figure 6.31**(with the initial solution concentration decreasing in series from A-G), it is clear that the adsorption capacity of the material decreases as the pH increases towards the point of zero charge. However, it is also clear that the adsorption from the mixed solutions should also be theoretically higher than the adsorption from the carbonate solutions. This suggests that co-adsorption of oxalate and carbonate has an effect on not only the way hydrotalcite adsorbs, but also on how much material the hydrotalcite can adsorb, meaning that adsorption of oxalate from synthetic Bayer liquor is not viable.

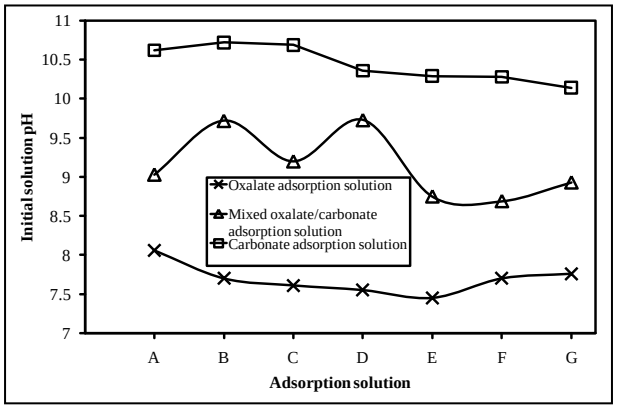

Figure 6.31: Plot of initial pH of adsorption solutions

6.2.5 HYDROTALCITE ADSORPTION SUMMARY

From the hydrotalcite adsorption studies, which are summarised in **Table 6.1** below, it was found that the single solution adsorption studies followed a Freundlich adsorption isotherm rather than a Langmuir adsorption isotherm, which is suggestive of adsorption capacity being controlled by concentration.

However, describing adsorption from the mixed oxalate/carbonate solutions could be described almost as well by the Langmuir adsorption isotherm as the Freundlich adsorption isotherm, with the exception of the carbonate component of the solution which did not fit a Freundlich adsorption isotherm. This is indicative of a change in adsorption as the solution becomes more complex.

Model/Plot	Parameter	Solution				
		Oxalate	Carbonate	oxalate/carbonate Mixture		
				$C_2O_4^{2-}$	CO_3^{2-}	Total
Langmuir adsorption isotherm	Fit (R^2)	No Fit	No Fit	0.934	0.9568	0.8204
	k_L	--	--	0.011 ±0.001	-0.47 ± 0.02	0.41 ± 0.07
	Adsorption Energy (kJ/mol)	--	--	-1.9 ± 0.1	-36 ± 2	13 ± 2
	Separation Factor (k_R)	--	--	0.28 ± 0.02	-0.0089 ± 0.0003	0.010 ± 0.001
Freundlich adsorption isotherm	Fit (R^2)	0.9421	0.9452	0.9372	No Fit	0.7714
	k_F	1.52 ± 0.08	-3.9 ± 0.2	-4.4 ± 0.3	--	-0.35 ± 0.08
	1/n (adsorption intensity)	1.43 ± 0.08	2.4 ± 0.1	2.3 ± 0.1	--	0.7 ± 0.1
Plot of $1/c_e$ vs. $1/q_e$	Fit (R^2)	0.9693	--	--	0.5234	0.8018
	Theoretical maximum adsorption (mg/g)	57 ± 2	--	--	7 ± 3	33 ± 6
Polyani Plot	Fit (R^2)	0.9898	0.9499	0.7718	No Fit	0.7602
	Theoretical maximum adsorption (mg/g)	63.6 ± 0.7	34 ± 2	12 ± 3	--	31 ± 7
	Adsorption energy (kJ/mol)	3.82 ± 0.04	2.6 ± 0.1	1.7 ± 0.4	--	2.4 ± 0.6
Theoretical Surface Area (m^2/g)		101 ± 1	44 ± 2	5.7 ± 0.1	11 ± 5	50 ± 10

Table 6.1: Summary of hydrotalcite adsorption data

In general, the use of the plot of $1/q_e$ vs. $1/c_e$ (which is based on the Langmuir adsorption model) was not a great method of describing adsorption capacity as the carbonate adsorption solution data and the oxalate component of the mixed oxalate/carbonate did not fit a Langmuir adsorption isotherm.

The Polyani plots could be applied to all but the carbonate component of the mixed oxalate/carbonate solutions and the calculated theoretical maximum adsorptions were reasonable in that they reflected the trends in the adsorption data.

From the adsorption data, it is clear that the single component adsorption of oxalate and carbonate fits the Freundlich adsorption model and that the Langmuir adsorption model is not applicable. When adsorption from mixed oxalate/carbonate systems is examined, it is clear that the co-adsorption has a major effect, as neither the Freundlich nor the Langmuir adsorption models fit very well.

The error bars for the adsorption plots were calculated by finding the standard errors for material adsorbed (q_e) and the analyte concentration at equilibrium (c_e). From the calculation of standard errors, it was found that the vertical error bars (q_e) was proportionally larger than horizontal error bars (c_e) for carbonate adsorption. It was determined that relationship of the vertical error to the horizontal error is defined by:

$$Eq_e = Ec_e \times \left(\frac{c_e}{q_e}\right)$$

Equation 6.1: Relationship between the vertical and horizontal error bars

6.2.6 THEORETICAL MODEL TO DESCRIBE ADSORPTION FROM OXALATE/CARBONATE SOLUTIONS BY HYDROTALCITE

From the data it is possible to propose a model to describe the adsorption at the hydrotalcite surface. The fact that both the Langmuir and Freundlich adsorption models are in some way applicable to an extent implies that not only is there a distribution of energy levels for the adsorption sites (governed by the applicability of the Freundlich adsorption isotherm). However, the adsorption intensity of 0.7 ± 0.7 suggests that adsorption is heterogeneous. Furthermore, the applicability of the Langmuir adsorption model suggests that the energy distribution of the active sites is very narrow.

From this information, it is proposed that carbonate adsorption fills the lower energy adsorption sites, which explains why the carbonate component of the solution adheres to a Langmuir adsorption model. It is proposed that this occurs because carbonate is slightly smaller and has a higher charge density.

The adsorption of the oxalate component follows a Freundlich adsorption isotherm, which corresponds to oxalate filling the higher energy adsorption sites, due to the larger size and slightly lower charge density of the oxalate anion.

6.3 THERMALLY ACTIVATED HYDROTALCITE ADSORPTION STUDIES

6.3.1 OXALATE ADSORPTION BY THERMALLY ACTIVATED HYDROTALCITES

Reformation studies of thermally activated hydrotalcites in oxalate solutions show that there are a number of processes that occur in the reformation process, which can be seen in **Figure 6.32**. The first of these processes is the reformation of the hydrotalcite structure, which involves the rapid absorption of oxalate anions from the solution, which occurs within the first 20 minutes of contact. The second phase of the reformation is the adsorption of oxalate anions up until the time of maximum uptake around 70 minutes, which is then followed by a process of desorption and replacement of the oxalate anions by carbonate anions up until 170 minutes, followed by what could be considered the start of ion exchange between oxalate and carbonate anions in the solution. It could be expected that the ion exchange will continue until equilibrium is reached.

Time (Min)	Average q_t (mg/g)	Time (Min)	Average q_t (mg/g)
0	0	100	80.2
10	68.1	110	84.1
20	72.7	120	80.5
30	71.6	130	79.0
40	76.8	140	80.7
50	80.3	150	77.2
60	83.9	160	76.7
70	86.2	170	78.2
80	82.2	180	62.2
90	84.1		

Table 6.2: Adsorption data for oxalate adsorption by TAHT in air

The adsorption of oxalate at the point of maximum uptake, as determined from the data (see and **Table 6.2**), is 86.2 ± 0.4 mg/g thermally activated hydrotalcite after 70 minutes. The active surface area was calculated to be 136 ± 1 m^2/g using **Equation 3.5**. This is slightly higher than that calculated for hydrotalcite.

The kinetics of adsorption were studied in order to gain an understanding of the adsorption processes involved. The Lagergren plot, which correlates to first order kinetics (rate of adsorption is independent of concentration) does not fit the expected linear model, which shows that the reformation of the thermally activated hydrotalcite does not follow a first order kinetic model.

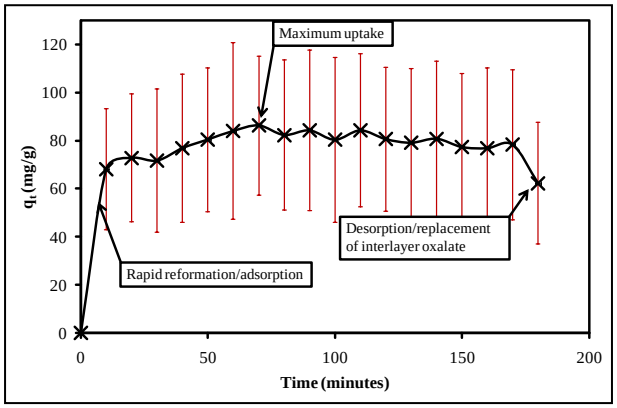

Figure 6.32: Plot of oxalate adsorption (q_t) vs. Time for thermally activated hydrotalcite in oxalate solution

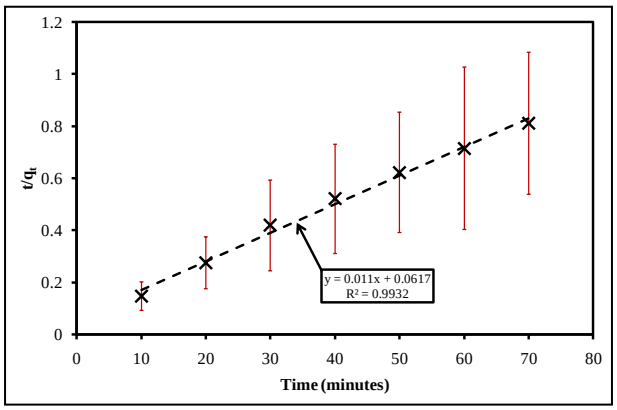

Figure 6.33: plot of $\frac{t}{q_t}\ vs\ t$ for thermally activated hydrotalcite in oxalate solution

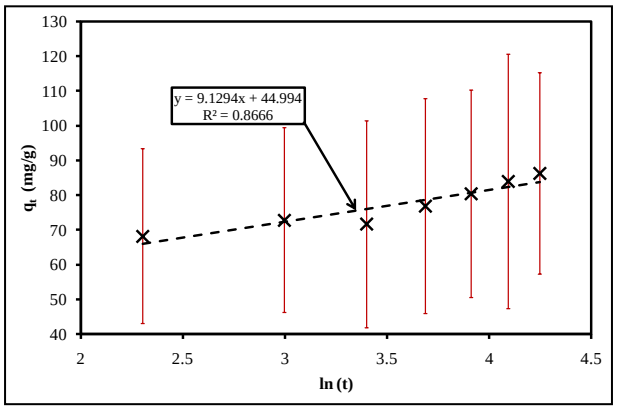

Figure 6.34: Elovich plot to maximum adsorption of thermally activated hydrotalcite in oxalate solution

The plot of $\frac{t}{q_t}\ vs\ t$ (**Figure 6.33**) shows excellent correlation (R^2 0.9932) between the plotted data and the 2nd order kinetics model $\left(\frac{t}{q_t} = \frac{1}{k_2 q_e^2} + \left(\frac{1}{q_e}\right) t\right)$ which allows for the calculation of q_e and k_2. From the slope of the trendline, the theoretical adsorption capacity at equilibrium is 78.7 ± 0.5 mg/g while the intercept yields a k_2 of $-1.4 \pm 0.1 \times 10^{-2}$ mg/g/min.

The Elovich plot (**Figure 6.34**) for the first 70 minutes (to the point of maximum adsorption) shows a moderate correlation (R^2 0.8666) to the model and gives an initial adsorption rate (α) of 45 ± 6 mg/g/min and a desorption constant (β) of 9 ± 1 mg/g/min.

From the Elovich and $\frac{t}{q_t}\ vs\ t$ plots, the reformation of the thermally activated hydrotalcite appears, in oxalate solution, to follow a second order kinetics model, suggesting that the rate of reformation is dependent on concentration.

The plot of $q_t vs\ \sqrt{t}$ does not form a linear relationship passing through the origin showing that intraparticle diffusion does not play a part in the reformation of thermally activated hydrotalcite in oxalate solutions.

6.3.2 OXALATE/CARBONATE ADSORPTION BY THERMALLY ACTIVATED HYDROTALCITE

From the adsorption data (**Table 6.3** and **Figure 6.35**), it is clear that there is a preference of thermally activated hydrotalcite for carbonate, with the maximum adsorption capacity with respect to carbonate being 48 ± 2 mg/g thermally activated hydrotalcite within a 20 minute contact time and the adsorption capacity for oxalate being 3 ± 1 mg/g thermally activated hydrotalcite after 90 minutes contact time. The overall active surface area for the thermally activated hydrotalcite was calculated to be 97 ± 14 m^2/g, which is again slightly higher than uncalcined hydrotalcite.

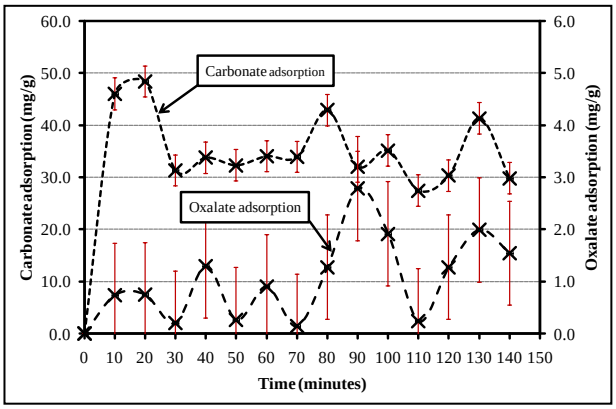

Figure 6.35: Plot of q_t vs t for the adsorption thermally activated hydrotalcite in an oxalate/carbonate solution

The maximum adsorption of the system was determined to be 49 ± 3 mg/g at 20 minutes of contact time, followed quickly by establishment of equilibrium.

Time (minutes)	Oxalate Adsorption (mg/g)	Carbonate adsorption (mg/g)	Total Adsorption (mg/g)
0	0.0	0.0	0.0
10	0.7	46.0	46.7
20	0.7	48.4	49.1
30	0.2	31.3	31.5
40	1.3	33.7	35.0
50	0.3	32.3	32.5
60	0.9	34.0	34.9
70	0.1	33.9	34.0
80	1.3	42.9	44.2
90	2.8	32.0	34.8
100	1.9	35.1	37.0
110	0.2	27.4	27.7
120	1.3	30.3	31.6
130	2.0	41.3	43.3
140	1.5	29.8	31.4

Table 6.3: Adsorption data for thermally activated hydrotalcite in an oxalate/carbonate mixture

Due to co-adsorption effects resulting in oxalate adsorption being extremely variable, it was impossible to determine any of the kinetic parameters of the system.

There are some differences between the adsorption of an oxalate/carbonate mixture by thermally activated hydrotalcite and the adsorption of oxalate using the same method. The first noticeable difference is that after fast initial reformation, the adsorbed carbonate quickly appears to establish equilibrium around 33 ± 1 mg/g adsorbed carbonate for the first 70 minutes (**Figure 6.35**). After this time, although there is variation in the adsorbed carbonate, this is most likely random scatter. It was impossible to determine the adsorption kinetics of the system with certainty due to the rapid reformation of the thermally activated hydrotalcite to hydrotalcite and that the sampling interval was ten minutes.

For the oxalate component of the system, the oxalate adsorption is low with the maximum adsorption being 3 ± 1 mg/g oxalate at 90 minutes contact time. Because the adsorption of oxalate is so low with such a high variance, the adsorption of oxalate in this system is probably due to ion exchange and the establishment of equilibrium.

6.3.3 SUMMARY OF THERMALLY ACTIVATED HYDROTALCITE ADSORPTION

For the thermally activated hydrotalcites, it was possible to determine some parameters for thermally activated hydrotalcites in contact with oxalate solutions. However, when thermally activated hydrotalcites were placed in contact with mixed oxalate/carbonate solutions, it was impossible to sample at intervals capable of giving meaningful results.

		Oxalate	Mixed Solution		
			Oxalate	Carbonate	Total
Maximum Adsorption (mg/g)		86.2 ± 0.4	3 ± 1	48 ± 2	49 ± 3
Active Surface Area (m^2/g)		136 ± 1	--	--	97 ± 6
Lagergren Kinetic Model		--	--	--	--
2^{nd} Order Kinetics	**R^2**	0.9932	--	--	--
	q_e (mg/g)	78.7±0.5	--	--	--
	K_2 (mg/g/min)	-1.4 ± 0.1 x10^{-2}	--	--	--
Elovich Kinetics Model	**R^2**	0.8666	--	--	--
	α (mg/g/min)	45 ± 6	--	--	--
	β (mg/g/min)	9 ± 1	--	--	--
Intraparticle diffusion kinetic model		--	--	--	--

Table 6.4: Summary of thermally activated hydrotalcite adsorption

However, it was determined that the use of thermally activated hydrotalcites had an oxalate uptake of 86.2 ± 0.4 mg/g hydrotalcite and adhered to second order kinetic models, as shown in **Table 6.4** above. For oxalate pick-up from a mixed oxalate/carbonate solution, maximum oxalate up-take was determined experimentally to be 3 ± 1 mg/g while the overall uptake was 49 ± 3 mg/g, which is significantly less than the uptake from an oxalate solution.

The error bars used in the kinetic adsorption plots were calculated using the standard error method. The error bars were found to be relatively large due to significant tailing of the oxalate TOC peaks, which is due to the decomposition of oxalate in the TOC being kinetically hindered.

Chapter 7: Conclusions and Recommendations

7.1 AIMS & OBJECTIVES

7.1.1 DEVELOPING A HYDROTALCITE THAT HAS BEEN SUCCESSFULLY INTERCALATED WITH OXALATE FOR CHARACTERISATION AND ANALYSIS

Oxalate intercalated hydrotalcites were prepared through the use of *in-situ* intercalation (**Section 5.5**) and the use of the re-co-precipitation technique (**Section 5.6**). Both methods were shown to be successful at intercalating oxalate into the interlayer spaces of hydrotalcite, and this is supported by the evidence of X-ray diffraction and infrared analysis. For the first time, Raman analysis (**Section 5.5.3**) and infrared emission spectroscopy (**Section 5.5.4**) have been used to characterise hydrotalcite. Furthermore, the first theory to describe the thermal stability of oxalate intercalated hydrotalcite has been proposed (**Section 5.55** and summarised in **Section 7.2.1**).

7.1.2 PREPARING AND CHARACTERISING HYDROTALCITE SO THAT THE ADSORBENT, ABSORBENT AND ION EXCHANGE PROPERTIES CAN BE EXAMINED

Hydrotalcite was prepared by the use of the co-precipitation method and characterised using X-ray diffraction, infrared, Raman and infrared emission spectroscopy; along with thermogravimetric analysis, BET Analysis, SEM and TEM imaging (see **Section 5.1**). The analysis of these materials shows the typical behaviour of hydrotalcites of the same composition reported in the literature.

7.1.3 TESTING THE ADSORPTION, ABSORPTION AND ION EXCHANGE PROPERTIES OF THESE MATERIALS TO UNDERSTAND THEIR PHYSICAL BEHAVIOUR

The adsorption properties for hydrotalcite and thermally activated hydrotalcites were performed on aqueous oxalate solutions and aqueous oxalate/carbonate mixtures. From the adsorption data, it was determined that neither hydrotalcite nor thermally activated hydrotalcites would be appropriate adsorbents for the removal of oxalate anions from Bayer Process liquors.

7.1.4 MODELLING THE BEHAVIOUR OF THESE MATERIALS IN ORDER TO GAIN AN UNDERSTANDING OF THE SURFACE CHEMISTRY OF THESE MATERIALS FOR POTENTIAL FURTHER STUDY INTO THE PREPARATION OF FUTURE ANION ADSORBENTS

It was possible to test some of the adsorption models for the adsorption of oxalate by hydrotalcite and thermally activated hydrotalcite. From the adsorption data, it was shown that both Freundlich and Langmuir adsorption models can be used to determine the adsorption properties of hydrotalcite. For thermally activated hydrotalcite, it was possible to determine that the adsorption of oxalate from an aqueous solution adhered to second order kinetics models. However, when carbonate anions were added to the system, it was impossible to determine the kinetics model that best fit the adsorption of oxalate due to the preferential uptake of carbonate.

Furthermore, this is the first time in the literature that an oxalate/carbonate adsorption mixture has been tested by hydrotalcite and thermally activated hydrotalcites. From the batch adsorption studies, a simple model has been developed to describe the adsorption behaviour of these adsorption systems (see **Section 6.2.6**).

7.2 MAJOR CONCLUSIONS: MATERIALS PREPARATION AND CHARACTERISATION

7.2.1 OXALATE INTERCALATED HYDROTALCITES

From the analysis of the oxalate intercalated hydrotalcites it can be concluded that oxalate was successfully intercalated into the structure of hydrotalcite using both *in-situ* intercalation and re-co-precipitation intercalation methods. It was shown through XRD analysis that there may be an intermediate structure for oxalate intercalated hydrotalcite which has a 003 peak at an angle of around 9 °2θ (although this was not conclusively shown) and that XRD cannot be used for identification of oxalate intercalated hydrotalcite as samples generally had a diffraction pattern very similar to that of a carbonate intercalated hydrotalcite.

An IR analysis shows the presence of extra C-O bonds that are also present in sodium carbonate and Raman analysis shows a number of C-O bands that can be used to identify the intercalation of oxalate into the structure of the hydrotalcite as well as variation to the metal-hydroxide bonding within the structure.

Surface area analysis using nitrogen adsorption shows that there has been an increase in the surface area for the oxalate intercalated hydrotalcites when compared to the precursor materials. Nitrogen adsorption data also shows that preparation method has an effect on surface area due to differences in crystallite size.

Thermal analysis, namely TGA and IES analysis, shows that there has been a change in the thermal stability of the material upon the intercalation of hydrotalcite. This is due to the oxalate decomposing at a higher temperature than carbonate.

From the TGA and IES data, it was possible to develop a novel model to explain the decomposition steps of oxalate intercalated hydrotalcites (first explained in **Section 5.5.5**), which proceeds in the following series of steps:

1. Removal of interlayer water from the interlayer spaces below 200 °C;
2. Decomposition of oxalate around 350 °C, followed by linkage of half of the decomposed oxalate anion to the metal-hydroxide layer to form bicarbonate by 400 °C;
3. Further dehydration of the metal-hydroxide layer, which results in the carbonate anion pushing into the metal-hydroxide layer (similar to **Section 5.1.5**); followed by
4. Complete decarbonisation and dehydroxylation of the material to form spinel and periclase by 1000 °C.

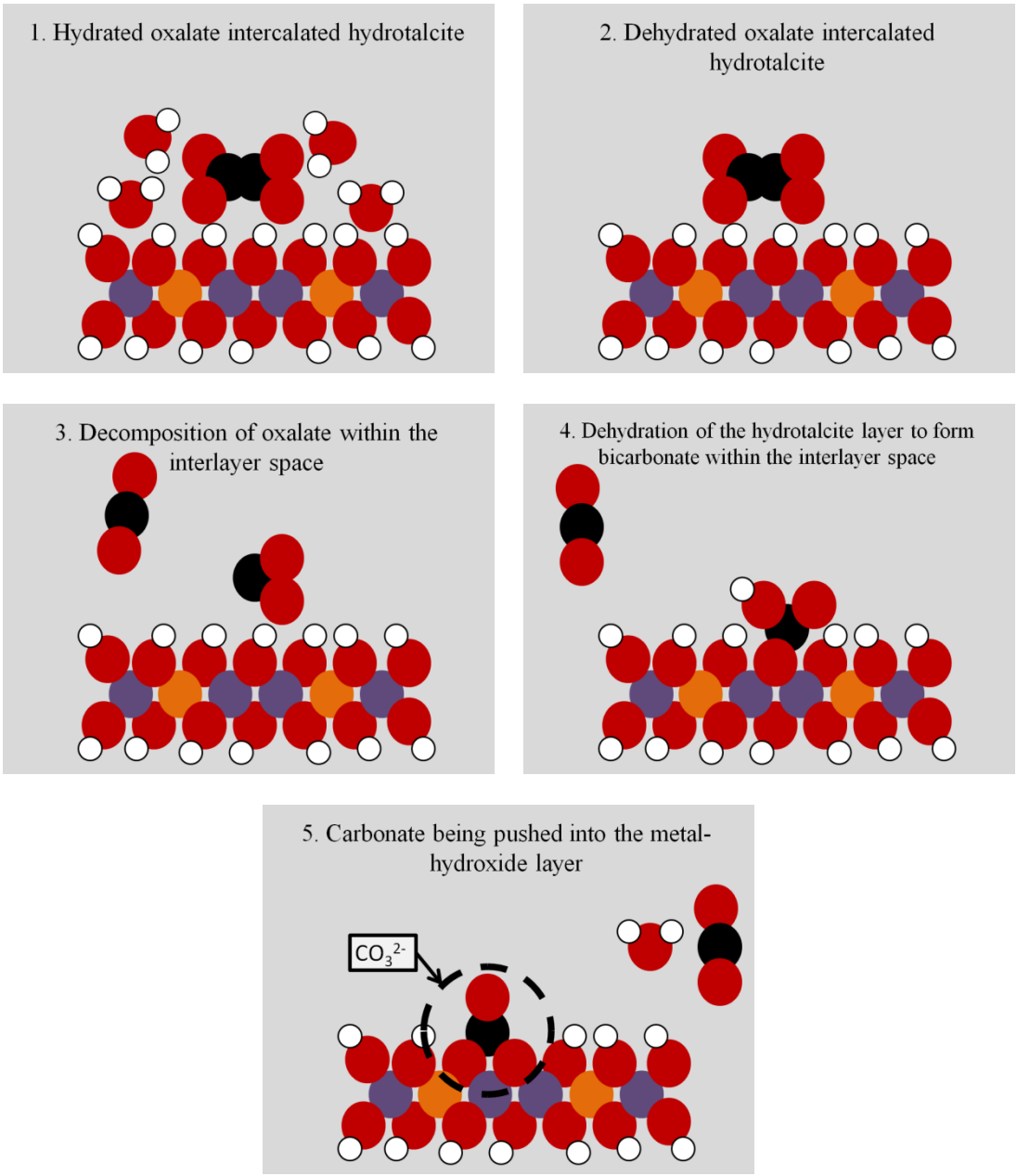

Figure 7.1: Theoretical decomposition model for oxalate intercalated hydrotalcite

7.2.2 THERMALLY ACTIVATED HYDROTALCITES

From the thermally activated materials analysis, it was shown that it is possible that a thermal activation time of 24 hours at 280 °C was more efficient than thermal activation at the same temperature over time frames of 17 and 70 hours.

XRD shows that the hydrotalcite layers collapse upon thermal treatment, due to decarbonisation and some dehydroxylation of the material (although it maintains its layered structure. This collapse is demonstrated by an increase in the diffraction angle of the 003 peak from around 11 °2θ to around 13.5 °2θ for thermal activation of hydrotalcite performed at 280 °C. It was also seen that thermally activated hydrotalcites are very hydrophilic and are capable of reforming hydrotalcite upon contact with a humid atmosphere, which has been shown in the XRD patterns of the 24 and 70 hour activated hydrotalcites, which provided evidence of some hydrotalcite reformation upon contact with a humid atmosphere.

It was also shown that vibrational spectroscopy is excellent for determining that carbonate has been lost from the material although dehydroxylation is harder to determine using either infrared or Raman spectroscopy.

Hydrotalcite that has been thermally activated for 24 hours has a surface area approximately double that of the precursor material, which is higher than 17 and 70 hours of thermal treatment. This also suggests that 24 hours of thermal treatment is optimal for the activation of hydrotalcite. The large surface area of hydrotalcites that have been thermally activated for 24 hours makes them better candidates for the adsorption of anions from aqueous solutions.

7.3 ADSORPTION STUDIES

7.3.1 HYDROTALCITES

7.4.1.1 Oxalate solutions

Hydrotalcite was shown to be a capable adsorbent of oxalate in aqueous solution with a theoretical adsorption capacity of between 85 ±2 and 63.6 ± 0.7 mg/g. The adsorption was found to best fit the Freundlich adsorption isotherm (R^2 0.9421), which is suggestive of a distribution of the energy of the adsorption sites, whilst it was determined that the Langmuir adsorption isotherm was not applicable in this case.

7.4.1.2 Carbonate solutions

Hydrotalcite was shown to be a suitable adsorbent of carbonate in aqueous solution with a theoretical adsorption capacity of 34 ± 2 mg/g. The adsorption was found to fit the Freundlich adsorption isotherm (R^2 0.9452), whilst it was determined that the Langmuir adsorption isotherm was not applicable to this adsorption study.

7.4.1.3 Oxalate/carbonate solutions

With competition from carbonate, the oxalate adsorption capacity of hydrotalcite was reduced to 12 ± 3 mg/g hydrotalcite, with the overall adsorption capacity also reduced to 31 ± 7 mg/g hydrotalcite. This reduction in overall adsorption capacity is most likely due to competition between oxalate and carbonate anions hindering access of anions to less available adsorption sites in the hydrotalcite.

In this case, the overall adsorption was best explained by the Freundlich adsorption isotherm (R^2 = 0.8018) rather than the Langmuir adsorption isotherm (R^2 = 0.7714), the relatively poor quality of the fit suggests that mixed adsorption is more complicated than the adsorption models used here.

Carbonate adsorption could not be described using the Freundlich adsorption isotherm, but rather by the use of the Langmuir adsorption isotherm (R^2 = 0.9568) which indicates that there has been a significant change to the adsorption process when competitive carbonate anions are added to the oxalate adsorption solution. Interestingly, the use of the D-R adsorption isotherm was not possible, as the Polyani plot did not give a fit. This indicates that none of the simple adsorption models considered here are applicable to describing the adsorption of oxalate and carbonate from a mixture by hydrotalcite.

The preference of hydrotalcite for carbonate rather than oxalate shows that hydrotalcite is not a good adsorbent for the removal of oxalate anions when there is competition from carbonates anions and on the basis of this evidence, adsorption testing on synthetic Bayer liquors was not conducted.

7.3.2 THERMALLY ACTIVATED HYDROTALCITES

7.4.2.1 Oxalate solutions

Adsorption of oxalate from an aqueous solution using thermally activated hydrotalcite was shown to be possible with an observed maximum adsorption of 86.2 ± 0.4 mg/g thermally activated hydrotalcite after 90 minutes contact.

It was also indicated that the adsorption of oxalate by a thermally activated hydrotalcite followed a pseudo-second order kinetic model with $k_2 = -1.4 \times 10^{-2}$ mg/g/min, an initial adsorption rate of 45 ± 6 mg/g/min and a theoretical adsorption capacity of 78.7 ± 0.5 mg/g thermally activated hydrotalcite. The Elovich model of second order kinetics gave an initial adsorption rate of 45 ± 6 mg/g/min and a desorption constant of 9 ± 1 mg/g/min.

7.4.2.2 Oxalate/carbonate solutions

With competition from carbonate, it was shown that the adsorption capacity of the thermally activated hydrotalcite was decreased, with an observed maximum adsorption capacity being 49 ± 3 mg/g thermally activated hydrotalcite at a contact time of 20 minutes. However, the maximum adsorption of oxalate was observed to be 3 ± 1 mg/g thermally activated hydrotalcite. It was also shown that due to the very quick establishment of equilibrium (30 minutes) it was impossible to determine the kinetics of this system with the sampling timeframe used (10 minutes).

On the basis of the adsorption data for the oxalate/carbonate mixture, it was determined that hydrotalcite would not be an appropriate adsorbent for the removal of oxalate from a synthetic Bayer liquor due to the thermally activated hydrotalcite having a greater selectivity for carbonate.

Chapter 8: Recommendations for further research

8.1.1 HYDROTALCITES

From the results of the adsorption studies, one major recommendation can be made: Studies should be performed into how the identity of the metal cation effects the selectivity of hydrotalcite-like compounds for carbonate.

8.1.2 OXALATE INTERCALATED HYDROTALCITES

From the results of the characterisation of the thermally activated hydrotalcites, it is recommended that studies should be performed into the structure of the oxalate intercalated hydrotalcite to determine if the intercalation of oxalate into the structure of the material yields a preferred orientation related to synthesis conditions.

It is also recommended that studies should be performed into modelling the atom locations within the unit cell of oxalate intercalated hydrotalcites. This should serve as a tool to identify changes in the material structure related to the insertion of other di-carboxylic acids.

8.1.3 THERMALLY ACTIVATED HYDROTALCITES

From the research data, the following recommendations are being made with respect to further research into thermally activated hydrotalcites to determine how low temperature thermal activation effects the structure of the hydrotalcite and from there determine more accurately the optimum thermal treatment temperature and time frame.

There is also some merit in finding Bayer liquor that has low carbonate and high oxalate concentrations for testing with thermally activated hydrotalcites to determine their applicability as adsorbents for that application.

8.1.4 ADSORBENTS

Due to the low adsorption of oxalate from the mixed oxalate/carbonate mixtures, it is recommended that other adsorbents, such as activated carbon be investigated as potential adsorbents for oxalate from Bayer Process liquors.

Chapter 9: References

1. Wellington, M. and F. Valcin, *Impact of Bayer Process Liquor Impurities on Causticization.* Ind. Eng. Chem. Res., 2007. **46**(15): p. 5094-5099.
2. Sidrak, Y.L., *Dynamic Simulation and Control of the Bayer Process. A Review.* Ind. Eng. Chem. Res., 2001. **40**(4): p. 1146-1156.
3. Prevot, V., C. Forano, and J.P. Besse, *Reactivity of oxalate with ZnAl layered double hydroxides through new materials.* Journal of Materials Chemistry, 1999. **9**(1): p. 155-160.
4. Stuart, A.D., T. Tran, and D.A.J. Swinkels, *The oxidative removal of organics in bayer liquors from alumina plants using manganese dioxide ore.* Hydrometallurgy, 1987. **19**(1): p. 37-49.
5. Dukkanci, M. and G. Gunduz, *Ultrasonic degradation of oxalic acid in aqueous solutions.* Ultrasonics Sonochemistry, 2006. **13**(6): p. 517-522.
6. Marciano, S., N. Mugnier, P. Clerin, B. Cristol, and P. Moulin, *Nanofiltration of Bayer process solutions.* Journal of Membrane Science, 2006. **281**(1-2): p. 260-267.
7. Pareek, V., M.P. Brungs, and A.A. Adesina, *Photocausticization of spent Bayer liquor: a pilot-scale study.* Advances in Environmental Research, 2003. **7**(2): p. 411-420.
8. Pareek, V.K., M.P. Brungs, and A.A. Adesina, *Continuous Process for Photodegradation of Industrial Bayer Liquor.* Ind. Eng. Chem. Res., 2001. **40**(23): p. 5120-5125.
9. Schlesinger, R., G. Götzinger, H. Sixta, A. Friedl, and M. Harasek, *Evaluation of alkali resistant nanofiltration membranes for the separation of hemicellulose from concentrated alkaline process liquors.* Desalination, 2006. **192**(1-3): p. 303-314.
10. Tardio, J., S. Bhargava, S. Eyer, M. Sumich, and D.B. Akolekar, *Interactions between Specific Organic Compounds during Catalytic Wet Oxidation of Bayer Liquor.* Ind. Eng. Chem. Res., 2004. **43**(4): p. 847-851.
11. Tardio, J., S. Bhargava, J. Prasad, and D.B. Akolekar, *Catalytic wet oxidation of the sodium salts of citric, lactic, malic and tartaric acids in highly alkaline, high ionic strength solution.* Topics in Catalysis, 2005. **33**(1-4): p. 193-199.
12. Tardio, J., S.K. Bhargava, S. Eyer, and D.B. Akolekar, *Low-Temperature Wet Oxidation of Sodium Salts of Low Molecular Weight Mono- and Dicarboxylic Acids in Synthetic Bayer Liquor.* Ind. Eng. Chem. Res., 2004. **43**(3): p. 669-674.
13. Palmer, S.J., *Stability of Hydrotalcites formed from Bayer Refinery Environmental Control Processes*, in *School of Physical and Chemical Sciences*. 2008, Queensland University of Technology: Brisbane. p. 58.
14. Baker, A.R. and A.M. Greenaway, *Comparison of Bauxite and Bayer Liquor Humic Substances by 13C Nuclear Magnetic Resonance Spectroscopy. Implications for the Fate of Humic Substances in the Bayer Process.* Ind. Eng. Chem. Res., 1998. **37**(10): p. 4198-4202.

15. Smeulders, D.E., M.A. Wilson, and L. Armstrong, *Poisoning of Aluminum Hydroxide Precipitation by High-Molecular-Weight Fractions of Bayer Organics.* Ind. Eng. Chem. Res., 2001. **40**(25): p. 5901-5907.
16. Barnett, N.W., S.W. Lewis, S.D. Purcell, and P. Jones, *Determination of sodium oxalate in Bayer liquor using flow-analysis incorporating an anion exchange column and tris(2,2'-bipyridyl)ruthenium(II) chemiluminescence detection.* Analytica Chimica Acta, 2002. **458**(2): p. 291-296.
17. Chen, Q.Y., J.B. Xiao, and X.Q. Chen, *Rapid determination of organic acids in Bayer liquors by high-performance liquid chromatography after solid-phase extraction.* Minerals Engineering, 2006. **19**(14): p. 1446-1451.
18. Chen, Y., Q. Feng, K. Liu, Y. Chen, and G. Zhang, *Study on the structure of Bayer liquor with spectroscopy and MD simulation.* Chemical Physics Letters, 2006. **422**(4-6): p. 406-411.
19. Guthrie, J.D., P.J. The, and W.D. Imbrogno, *Characterization of Organics in Bayer Liquor.* Light Met., 1984: p. 127-146.
20. Harakuwe, A.H., P.R. Haddad, and P.E. Jackson, *Quantitative determination of oxalate in Bayer liquor by capillary zone electrophoresis A validative study.* Journal of Chromatography A, 1996. **739**(1-2): p. 399-403.
21. Jackson, P.E., *Analysis of oxalate in Bayer liquors: a comparison of ion chromatography and capillary electrophoresis.* Journal of Chromatography A, 1995. **693**(1): p. 155-161.
22. Whelan, T.J., G.S.K. Kannangara, and M.A. Wilson, *Increased Resolution in High-Performance Liquid Chromatograph Spectra of High-Molecular-Weight Organic Components of Bayer Liquors.* Ind. Eng. Chem. Res., 2003. **42**(26): p. 6673-6681.
23. Wille, A. and M. Laeubli, *Determination of Common Anions and Organic Acids in Bayer Liquor Applying Metrohm In-line Neutralization*, in *LC-GC Europe*. 2006.
24. Palmer, S.J., R.L. Frost, and T. Nguyen, *Hydrotalcites and their role in coordination of anions in Bayer liquors: Anion binding in layered double hydroxides.* Coordination Chemistry Reviews, 2009. **253**(1-2): p. 250-267.
25. Palmer, S.J., B.J. Reddy, and R.L. Frost, *Characterisation of red mud by UV-vis-NIR spectroscopy.* Spectrochimica Acta Part A: Molecular and Biomolecular Spectroscopy, 2009. **71**(5): p. 1814-1818.
26. Prestidge, C.A. and I. Ametov, *Cation effects during aggregation and agglomeration of gibbsite particles under synthetic Bayer crystallisation conditions.* Journal of Crystal Growth, 2000. **209**(4): p. 924-933.
27. Li, J., C.A. Prestidge, and J. Addai-Mensah, *Secondary nucleation of gibbsite crystals from synthetic Bayer liquors: effect of alkali metal ions.* Journal of Crystal Growth, 2000. **219**(4): p. 451-464.
28. Li, J., C.A. Prestidge, and J. Addai-Mensah, *The Influence of Alkali Metal Ions on Homogeneous Nucleation of Al(OH)3 Crystals from Supersaturated Caustic Aluminate Solutions.* Journal of Colloid and Interface Science, 2000. **224**(2): p. 317-324.
29. Jones, F., J.B. Farrow, and W. van Bronswijk, *Effect of caustic and carbonate on the flocculation of haematite in synthetic Bayer liquors.* Colloids and Surfaces A: Physicochemical and Engineering Aspects, 1998. **142**(1): p. 65-73.

30. Zheng, K., A.R. Gerson, J. Addai-Mensah, and R.S.C. Smart, *The influence of sodium carbonate on sodium aluminosilicate crystallisation and solubility in sodium aluminate solutions.* Journal of Crystal Growth, 1997. **171**(1-2): p. 197-208.
31. Kovács, Z. and W. Samhaber, *Contribution of pH dependent osmotic pressure to amino acid transport through nanofiltration membranes.* Separation and Purification Technology, 2008. **61**(3): p. 243-248.
32. Mänttäri, M., A. Pihlajamäki, and M. Nyström, *Effect of pH on hydrophilicity and charge and their effect on the filtration efficiency of NF membranes at different pH.* Journal of Membrane Science, 2006. **280**(1-2): p. 311-320.
33. Nilsson, M., G. Trägårdh, and K. Östergren, *The influence of pH, salt and temperature on nanofiltration performance.* Journal of Membrane Science, 2008. **312**(1-2): p. 97-106.
34. Nilsson, M., F. Lipnizki, G. Trägårdh, and K. Östergren, *Performance, energy and cost evaluation of a nanofiltration plant operated at elevated temperatures.* Separation and Purification Technology, 2008. **60**(1): p. 36-45.
35. Van der Bruggen, B., M. Mänttäri, and M. Nyström, *Drawbacks of applying nanofiltration and how to avoid them: A review.* Separation and Purification Technology, 2008. **63**(2): p. 251-263.
36. Meylan, S., F. Hammes, J. Traber, E. Salhi, U. von Gunten, and W. Pronk, *Permeability of low molecular weight organics through nanofiltration membranes.* Water Research, 2007. **41**(17): p. 3968-3976.
37. Jarusutthirak, C., S. Mattaraj, and R. Jiraratananon, *Influence of inorganic scalants and natural organic matter on nanofiltration membrane fouling.* Journal of Membrane Science, 2007. **287**(1): p. 138-145.
38. Zagorodni, A.A., *Ion Exchange Materials: Properties and Applications*. 2006, Burlington: Elsevier Science.
39. Kumar, A., T.V.V. Rao, S.K. Mukerjee, and V.N. Vaidya, *Recycling of chemicals from alkaline waste generated during preparation of UO3 microspheres by sol-gel process.* Journal of Nuclear Materials, 2006. **350**(3): p. 254-263.
40. Di Girolamo, M. and M. Marchionna, *Acidic and basic ion exchange resins for industrial applications.* Journal of Molecular Catalysis A: Chemical, 2001. **177**(1): p. 33-40.
41. Chanda, M. and G.L. Rempel, *Sorption of sulfide on a macroporous, quaternized poly(4-vinyl pyridine) in alkaline medium.* Reactive Polymers, 1995. **24**(3): p. 203-212.
42. Horng, L.-L. and D. Clifford, *The behavior of polyprotic anions in ion-exchange resins.* Reactive and Functional Polymers, 1997. **35**(1-2): p. 41-54.
43. Frost, R., A. Musemeci, J.T. Kloprogge, M. Adebajo, and W. Martens, *Raman Spectroscopy of Hydrotalcites with Phosphate in the interlayer - Implications for the Removal of Phosphate from Water.* Journal of Raman Spectroscopy, 2006. **37**(7): p. 733-741.
44. Frost, R. and J. Reddy, *Thermo-Raman Sepctroscopic Study of the Natural Layered Double Hydroxide Manasseite.* Spectrochemica Acta, 2006. **65**(3-4): p. 553-559.
45. He, J., M. Wei, B. Li, Y. Kang, D. Evans, and X. Duan, *Preparation of Layered Double Hydroxides*, in *Layered Double Hydroxides*. 2006. p. 89-119.

46. Frost, R., M.L. Weier, and J.T. Kloprogge, *Raman Spectroscopy of some Natural Hydrotalcites with Sulphate and Carbonate in the Interlayer.* Journal of Raman Spectroscopy, 2003. **34**(10): p. 760-768.
47. Li, F. and X. Duan, *Applications of Layered Double Hydroxides*, in *Layered Double Hydroxides*. 2006. p. 193-223.
48. Kukkadapu, R.K., M.S. Witkowski, and J.E. Amonette, *Synthesis of a Low-Carbonate High-Charge Hydrotalcite-like Compound at Ambient Pressure and Atmosphere.* Chem. Mater., 1997. **9**(2): p. 417-419.
49. Sabbar, E.M., M.E. de Roy, and F. Leroux, *New Cu and/or Pt complexes intercalated MgAl-hydrotalcite-type anionic clays: Synthesis, characterization, thermal behavior and textural properties.* Microporous and Mesoporous Materials, 2007. **103**(1-3): p. 134-141.
50. Rivera, J.A., G. Fetter, and P. Bosch, *Microwave power effect on hydrotalcite synthesis.* Microporous and Mesoporous Materials, 2006. **89**(1-3): p. 306-314.
51. Brei, V.V., O.V. Melezhyk, G.M. Starukh, E.I. Oranskaya, and P.A. Mutovkin, *Organic precursor synthesis of Al-Mg mixed oxides and hydrotalcites.* Microporous and Mesoporous Materials, 2008. **113**(1-3): p. 411-417.
52. Zhu, J., P. Yuan, H. He, R. Frost, Q. Tao, W. Shen, and T. Bostrom, *In situ synthesis of surfactant/silane-modified hydrotalcites.* Journal of Colloid and Interface Science, 2008. **319**(2): p. 498-504.
53. Du, L. and B. Qu, *Effects of Synthesis Conditions on Crystal Morphological Structures and Thermal Degradation Behavior of Hydrotalcites and Flame Retardant and Mechanical Properties of EVA/Hydrotalcite Blends.* Polymer Composites, 2008. **28**(2): p. 131-138.
54. Climent, M.J., A. Corma, S. Iborra, K. Epping, and A. Velty, *Increasing the basicity and catalytic activity of hydrotalcites by different synthesis procedures.* Journal of Catalysis, 2004. **225**(2): p. 316-326.
55. Dávila, V., E. Lima, S. Bulbulian, and P. Bosch, *Mixed Mg(Al)O oxides synthesized by the combustion method and their recrystallization to hydrotalcites.* Microporous and Mesoporous Materials, 2008. **107**(3): p. 240-246.
56. Braterman, P.S., P.X. Zhi, and F. Yarberry, *Layered Double Hydroxides (LDHs)*, in *Handbook of Layered Materials*, S.M. Auerbach, K.A. Carrado, and P.K. Dutta, Editors. 2001, Marcel Dekker Inc.: Hoboken.
57. Drezdzon, M.A., *Synthesis of isopolymetalate-pillared hydrotalcite via organic-anion-pillared precursors.* Inorg. Chem., 1988. **27**(25): p. 4628-4632.
58. Salmones, J., B. Zeifert, M.H. Garduño, J. Contreras-Larios, D.R. Acosta, A.R. Serrano, and L.A. Garcia, *Synthesis and characterization of hydrotalcites by mechanical milling and conventional method.* Catalysis Today, 2008. **133-135**: p. 886-890.
59. Sideris, P.J., U.G. Nielsen, G. Zhehong, and C.P. Grey, *Mg/Al Ordering in Layered Double Hydroxides Revealed by Multinuclear NMR Spectroscopy.* Science, 2008. **321**: p. 113-117.
60. Bontchev, R.P., S. Liu, J.L. Krumhansl, J. Voigt, and T.M. Nenoff, *Synthesis, Characterization, and Ion Exchange Properties of Hydrotalcite $Mg_6Al_2(OH)_{16}(A)x(A')_{2-x}$. 4H2O (A, A' = Cl-, Br-, I-, and NO3-, 2 ≥ x ≥ 0) Derivatives.* Chem. Mater., 2003. **15**(19): p. 3669-3675.

61. Feng, Y.X., N. Yin, Q.F. Li, J.W. Wang, M.Q. Kang, and X.K. Wang, *Environmentally Benign Route for the Synthesis of Polycarbonate Diols (PCDLs)-Calcined MgAl Hydrotalcites as Heterogeneous Catalysts.* Ind. Eng. Chem. Res., 2008. **47**(7): p. 2140-2145.
62. Kloprogge, J.T. *Vibrational Spectroscopy of Minerals*. [Website] [cited 2008 1 September]; Online Minerals Database]. Available from: http://www.mineralatlas.com/General%20introduction/Introduction.htm.
63. Barthelmy, D. *Mineralogy Database*. [Website] 2000 1/26/08 [cited 2008 1 September]; Online Mineralogy Database]. Available from: http://webmineral.com/.
64. Hall, A. and M.G. Stamatakis, *Hydrotalcite and an Amorphous Clay Mineral in High-Magnesium Mudstones from the Kozani Basin, Greece.* Journal of Sedimentary Research, 2000. **70**(3): p. 549-558.
65. Kloprogge, J.T., M.L. Weier, I. Crespo, M.A. Ulibarri, C. Barriga, V. Rives, W. Martens, and R. Frost, *Intercalation of iron hexacyano complexees in Zn, Al Hydrotalcite, Part 2. An Mid-infrared and Raman Spectroscopic Study.* Journal of Solid State Chemistry, 2004. **177**: p. 1382-1387.
66. Frost, R. and A. Musemeci, *Nitrate adsorption through Hydrotalcite Reformation.* Journal of Colloid and Interface Science, 2006. **302**(1): p. 203-206.
67. Aisawa, S., H. Hirahara, H. Uchiyama, S. Takahashi, and E. Narita, *Synthesis and Thermal Decomposition of Mn-Al Layered Double Hydroxides.* Journal of Solid State Chemistry, 2002. **167**(1): p. 152-159.
68. Frost, R., A. Musemeci, J. Bouzaid, M. Adebajo, W. Martens, and J.T. Kloprogge, *Intercalation of hydrotalcites with hexacyanoferrate(II) and (III) -A ThermoRaman Spectroscopic Study.* Journal of Solid State Chemistry, 2005. **178**(1940-1948).
69. Ren, L., J. He, S. Zhang, D.G. Evans, and X. Duan, *Immobilization of penicillin G acylase in layered double hydroxides pillared by glutamate ions.* Journal of Molecular Catalysis B: Enzymatic, 2002. **18**(1-3): p. 3-11.
70. Zhang, J., F. Zhang, L. Ren, D.G. Evans, and X. Duan, *Synthesis of layered double hydroxide anionic clays intercalated by carboxylate anions.* Materials Chemistry and Physics, 2004. **85**(1): p. 207-214.
71. Sprynskyy, M., B. Buszewski, A. Terzyk, and J. Namiesnik, *Study of the selection mechanism of heavy metal (Pb^{2+}, Cu^{2+}, Ni^{2+} and Cd^{2+}) adsorption on clinoptilolite.* Journal of Colloid and Interface Science, 2006. **304**: p. 21-28.
72. Atkins, P. and J. De Paula, *Physical Chemistry*. 7th ed. 2002, New York: Oxford University Press.
73. Babel, S. and T.A. Kurniwan, *Low-cost adsorbents for heavy metals uptake from contaminated water: a review.* Journal of Hazardous Materials, 2003. **B97**: p. 219-243.
74. Amuda, O.S., A.A. Giwa, and I.A. Bello, *Removal of heavy metal from industrial wastewater using modified activated coconut shell carbon.* Biochemical Engineering Journal, 2007. **36**: p. 174-181.
75. Bhattacharyya, K.G. and S.S. Gupta, *Kaolonite, montmorillonite and their modified derivatives as adsorbents for removal of Cu(II) from aqueous solution.* Separation and Purification Technology, 2006. **50**: p. 388-397.

76. Bhattacharyya, K.G. and S.S. Gupta, *Adsorption of a few heavy metals on natural and modified kaolonite and monmorillonite: A review.* Advances in Colloid and Interface Science, 2008. **140**: p. 114-131.
77. Gupta, S.S. and K.G. Bhattacharyya, *Immobilization of Pb(II), Cd(II) and Ni(II) ions onto kaolonite and montmorillonite surfaces from aqueous medium.* Journal of Environmental Management, 2008. **87**: p. 46-58.
78. Ozverdi, A. and M. Erdem, *Cu^{2+}, Cd^{2+} and Pb^{2+} adsorption from aqueous solutions by pyrite and synthetic iron sulphide.* Journal of Hazardous Materials, 2006. **B137**: p. 626-632.
79. Tiwari, D., H.-U. Kim, and S.-M. Lee, *Removal beahaviour of sericite for Cu(II) and Pb(II) from aqueous solutions: Batch and column studies.* Separation and Purification Technology, 2007. **57**: p. 11-16.
80. Adebowale, K.O., I.E. Unuabonah, and B.I. Olu-Owolabi, *The effect of some operating variables on the adsorption of lead and cadmium ions on kaolonite clay.* Journal of Hazardous Materials, 2006. **B134**: p. 130-139.
81. Bouchenafa-Saib, N., K. Khouli, and O. Mohammedi, *Preparation and characterization of pillared montmorillonite: apllication in adsorption of cadmium.* Desalination, 2007. **217**: p. 282-290.
82. Ayoob, S., A.K. Gupta, P.B. Bhakat, and V.T. Bhat, *Investigations on the kinetics and mechanisms of sorptive removal of fluoride from water using alumina cement granules.* Chemical Engineering Journal, 2008. **140**(1-3): p. 6-14.
83. Turan, P., M. Dogan, and M. Alkan, *Uptake of trivalent chromium ions from aqueous solutions using kaolonite.* Journal of Hazardous Materials, 2007. **148**: p. 56-63.
84. Yan-Hui, L., D. Jun, L. Zhaokun, D. Zechao, Z. Yuefeng, X. Cailu, W. Dehai, and W. Bingqing, *Competitive adsorption of Pb^{2+}, Cu^{2+}, and Cd^{2+} ions from aqueous solutions by multiwalled carbon nanotubes.* Carbon, 2003. **41**: p. 2787-2792.
85. Kaya, A. and A.H. Oren, *Adsorption of Zinc from aqueous solutions to bentonite.* Journal of Hazardous Materials, 2005. **B125**: p. 183-189.
86. Unuabonah, I.E., K.O. Adebowale, B.I. Olu-Owolabi, L.Z. Yang, and L.X. Kong, *Adsorption of Pb (II) and Cd (II) from aqueous solutions onto sodium tetraborate-modified Kaolonite clay: Equilibrium and thermodynamic stidues.* Hydrometallurgy, 2008. **93**: p. 1-9.
87. Eren, E. and B. Afsin, *An investigation of Cu (II) adsorption by raw and acid-acivated bentonite: A combined potentiometric, thermodynamic, XRD, IR, DTA study.* Journal of Hazardous Materials, 2008. **151**: p. 682-691.
88. Hsieh, C.-T. and H. Teng, *Langmuir and Dubinin-Radushkevich analyses on equilibrium adsorption of activated carbon fabrics in aqueous solutions.* Journal of Chemical Technology and Biotechnology, 2000. **75**: p. 1066-1072.
89. Sari, A., M. Tuzen, C. Citak, and M. Soylak, *Equilibrium, kinetic and thermodynamic studies of adsorption of Pb (II) from aqueous solution onto Turkish kaolinite clay.* Journal of Hazardous Materials, 2007. **149**: p. 283-291.
90. Goh, K.-H., T.-T. Lim, and Z. Dong, *Application of layered double hydroxides for removal of oxyanions: A review.* Water Research, 2008. **42**(6-7): p. 1343-1368.

91. Wang, H., J. Chen, Y. Cai, J. Ji, L. Liu, and H.H. Teng, *Defluoridation of drinking water by Mg/Al hydrotalcite-like compounds and their calcined products.* Applied Clay Science, 2007. **35**(1-2): p. 59-66.
92. Mandal, S. and S. Mayadevi, *Adsorption of fluoride ions by Zn-Al layered double hydroxides.* Applied Clay Science, 2008. **40**(1-4): p. 54-62.
93. Lv, L., J. He, M. Wei, D.G. Evans, and X. Duan, *Uptake of chloride ion from aqueous solution by calcined layered double hydroxides: Equilibrium and kinetic studies.* Water Research, 2006. **40**(4): p. 735-743.
94. Lv, L., J. He, M. Wei, D.G. Evans, and Z. Zhou, *Treatment of high fluoride concentration water by MgAl-CO3 layered double hydroxides: Kinetic and equilibrium studies.* Water Research, 2007. **41**(7): p. 1534-1542.
95. Lv, L., J. He, M. Wei, D.G. Evans, and X. Duan, *Factors influencing the removal of fluoride from aqueous solution by calcined Mg-Al-CO3 layered double hydroxides.* Journal of Hazardous Materials, 2006. **133**(1-3): p. 119-128.
96. Das, J., B.S. Patra, N. Baliarsingh, and K.M. Parida, *Adsorption of phosphate by layered double hydroxides in aqueous solutions.* Applied Clay Science, 2006. **32**(3-4): p. 252-260.
97. Bhattacharyya, K.G. and S.S. Gupta, *Kaolonite and montmoriilonite as adsorbents for Fe(III), Co(II) and Ni(II) in aqueous medium.* Applied Clay Science, 2008. **41**: p. 1-9.
98. Kloprogge, J.T., L. Hickey, and R.L. Frost, *Synthesis and spectroscopic characterisation of deuterated hydrotalcite.* Journal of Materials Science Letters, 2002. **21**(8): p. 603-605.
99. Costa, F.R., A. Leuteritz, U. Wagenknecht, D. Jehnichen, L. Häußler, and G. Heinrich, *Intercalation of Mg-Al layered double hydroxide by anionic surfactants: Preparation and characterization.* Applied Clay Science, 2008. **38**(3-4): p. 153-164.
100. Tao, Q., Y. Zhang, X. Zhang, P. Yuan, and H. He, *Synthesis and Characterization of Layerd Double Hydroxide with a High Aspect Ratio.* Journal of Solid State Chemistry, 2006. **179**: p. 708-715.
101. Kloprogge, J.T., D. Wharton, L. Hickey, and R.L. Frost, *Infrared and Raman study of interlayer anions CO_3^{2-}, NO_3^-, SO_4^{2-} and ClO_4^- in Mg/Al-hydrotalcite.* American Mineralogist, 2002. **87**: p. 623-629.
102. Tsyganok, A. and A. Sayari, *Incorporation of transition metals into Mg-Al layered double hydroxides: Coprecipitation of cations vs. their pre-complexation with an anionic chelator.* Journal of Solid State Chemistry, 2006. **179**(6): p. 1830-1841.
103. Kloprogge, J.T., R.L. Frost, and L. Hickey, *FT-Raman and FT-IR spectroscopic study of the local structure of Mg/Zn/Al-hydrotalcites.* Journal of Raman Spectroscopy, 2004. **35**: p. 967-974.
104. Frost, R.L., S.J. Palmer, G.A. Ayoko, and T. Nguyen, *Synthesis and Raman spectroscopic characterisation of hydrotalcite with CO_3^{2-} and $(MoO_4)^{2-}$ anions in the interlayer.* Journal of Raman Spectroscopy, 2008. **39**(3): p. 695-401.
105. Stanimirova, T., I. Vergilov, G. Kirov, and N. Petrova, *Thermal decomposition products of hydrotalcite-like compounds: low-temperature metaphases.* Journal of Materials Science, 1999. **34**(17): p. 4153-4161.

106. Stanimirova, T.S. and V. Balek, *Characterization of layered double hydroxide Mg-Al-CO_3 prepared by re-hydration of Mg-Al mixed oxide.* Journal of Thermal Analysis and Calorimetry, 2008. **94**(2): p. 477-481.
107. Stanimirova, T.S., T. Hibino, and V. Balek, *Thermal behaviour of Mg-Al-CO_3 layered double hydroxide characterised by emnation thermal analysis.* Journal of Thermal Analysis and Calorimetry, 2006. **84**(2): p. 473-478.
108. Rives, V., *Characterisation of layered double hydroxides and their decomposition products.* Journal of Materials Chemistry and Physics, 2002. **75**: p. 19-25.
109. Hibino, T., Y. Yamashita, K. Kosuge, and A. Tsunashima, *Decarbonation behaviour of Mg-Al-CO_3 Hydrotalcite-like compounds during heat treatment.* Clays and Clay Minerals, 1995. **43**(4): p. 427-432.
110. Kloprogge, J.T. and R.L. Frost, *Infrared Emission Spectroscopic Study of the dehydroxylation of synthetic Mg/Al and Mg/Zn/Al-hydrotalcites.* Physical Chemistry Chemical Physics, 1999. **1**: p. 1641-1647.
111. Hutson, N.D., S.A. Speakman, and E.A. Payzant, *Structural Effects on the High Temperature Adsorption of CO2 on a Synthetic Hydrotalcite.* Chemistry of Materials, 2004. **16**(21): p. 4135-4143.
112. Sharma, U., B. Tyagi, and R.V. Jasra, *Synthesis and Characterization of Mg-Al-CO3 Layered Double Hydroxide for CO2 Adsorption.* Industrial & Engineering Chemistry Research, 2008. **47**(23): p. 9588-9595.
113. Qian, G., Z.P. Xu, J. Zhang, Y.F. Xu, C. Chen, and Q. Liu, *Reinvestigation of Dehydration and Dehydroxylation of Hydrotalcite-like Compounds through Combined TG-DTA-MS Analyses.* Journal of Physical Chemistry C, 2010. **Article In Press**.
114. Lazaridis, N.K., T.D. Karapantsios, and D. Georgantas, *Kinetic analysis for the removal of a reactive dye from aqueous solution onto hydrotalcite by adsorption.* Water Research, 2003. **37**(12): p. 3023-3033.
115. Holgado, M.J., V. Rives, M.S. Sanromán, and P. Malet, *Hexacyanoferrate-interlayered hydrotalcite.* Solid State Ionics, 1996. **92**(3-4): p. 273-283.
116. Michalik, A., E.M. Serwicka, K. Bahranowski, A. Gawel, M. Tokarz, and J. Nilsson, *Mg,Al-hydrotalcite-like compounds as traps for contaminants of paper furnishes.* Applied Clay Science, 2008. **39**(1-2): p. 86-97.
117. Abelló, S. and J. Pérez-Ramírez, *Steam activation of Mg-Al hydrotalcite. Influence on the properties of the derived mixed oxides.* Microporous and Mesoporous Materials, 2006. **96**(1-3): p. 102-108.
118. Ferreira, O.P., S.G. de Moraes, N. Durán, L. Cornejo, and O.L. Alves, *Evaluation of boron removal from water by hydrotalcite-like compounds.* Chemosphere, 2006. **62**(1): p. 80-88.
119. Ficicilar, B. and T. Dogu, *Breakthrough analysis for CO2 removal by activated hydrotalcite and soda ash.* Catalysis Today, 2006. **115**(1-4): p. 274-278.
120. Walfaran, G.E. and E. Pugh, *Raman combinations and stretching overtones from water, heavy water and NaCl in water at shifts to ca. 7000cm^{-1}*. Journal of Solution Chemistry, 2004. **33**(1): p. 81-97.
121. Carey, D.M. and G.M. Korenowski, *Measurement of the Raman spectrum of liquid water.* Journal of Chemical Physics, 1998. **108**(7): p. 2669-2675.
122. Ito, K. and H.J. Bernstein, *The Vibrational Spectra of the formate, acetate and oxalate ions.* Canadian Journal of Chemistry, 1956. **34**: p. 170-178.

123. Frost, R.L. and M.L. Weier, *Raman spectroscopy of natural oxalates at 298 and 77 K.* Journal of Raman Spectroscopy, 2003. **34**: p. 776-785.
124. Hind, A.R., S.K. Bhargava, W. Van Bronswijk, and S.C. Grocott, *On the Aqueous Vibrational Spectra of Alkali Metal Oxalates.* Applied Spectroscopy, 1998. **52**(5): p. 683-691.
125. Ricci, M.A., G. Signorelli, and V. Mazzacurati, *Raman spectra of water in the translational and librational regions.* Journal of Physics: Condensed Matter, 1990. **2**: p. SA183-SA187.
126. Jules, C.A.A.R., A.v.B. Jeroen, A.J.v. Dillen, W.G. John, and P.d.J. Krijn, *The Thermal Decomposition of Mg-Al Hydrotalcites: Effects of Interlayer Anions and Characteristics of the Final Structure.* Chemistry - A European Journal, 2002. **8**(24): p. 5571-5579.
127. Han, S., W. Hou, C. Zhang, D. Sun, X. Huang, and a. Gouting Wang, *Structure and the point of zero charge of magnesium aluminium hydroxide.* Journal of the Chemical Society, Faraday Transactions, 1998. **94**(7): p. 915-918.